Title
Ferroelectric Ordering in Colloidal Nanocrystals

Author
Polking, Mark Joseph

Publication Date
2011

Peer reviewed|Thesis/dissertation

Ferroelectric Ordering in Colloidal Nanocrystals

by

Mark Joseph Polking

A dissertation submitted in partial satisfaction of the

requirements for the degree of

Doctor of Philosophy

in

Engineering - Materials Science and Engineering

and the Designated Emphasis

in

Nanoscale Science and Engineering

in the

Graduate Division

of the

University of California, Berkeley

Committee in charge:

Professor A. Paul Alivisatos, Chair

Professor Ramamoorthy Ramesh

Professor Joel Moore

Fall 2011

Ferroelectric Ordering in Colloidal Nanocrystals

by

Mark Joseph Polking

Abstract

Ferroelectric Ordering in Colloidal Nanocrystals

by

Mark Joseph Polking

Doctor of Philosophy in Engineering - Materials Science and Engineering

and the Designated Emphasis in

Nanoscale Science and Engineering

University of California, Berkeley

Professor A. Paul Alivisatos, Chair

The size-stability and fundamental nature of ferroelectric ordering in low-dimensional nanomaterials are explored using colloidal nanocrystals of the ferroelectric semiconductor germanium telluride (GeTe) and the archetypal perovskite ferroelectric barium titanate ($BaTiO_3$). The synthesis of size-controlled colloidal GeTe nanocrystals is first explored, and the evolution of a polarization domain structure with increasing size is examined with transmission electron microscopy (TEM) and electron diffraction. The size-dependent ferroelectric ordering in ensembles of GeTe nanocrystals is then examined using a combination of temperature-dependent synchrotron x-ray diffraction, Raman scattering, and aberration-corrected TEM. Finally, the polarization state in individual nanocrystals of GeTe and $BaTiO_3$ is elucidated using atomic-resolution TEM, off-axis electron holography, and piezoresponse force microscopy (PFM). The nature of the polar state and the correlations among local ferroelectric distortions are compared for the cases of GeTe and $BaTiO_3$, the former a highly conductive semiconductor and the latter an electrical insulator, to deconvolute the influences of surface-induced strains and depolarization fields on the nature of the polar state.

GeTe nanocrystals with sizes ranging from 8 nm to 500 nm and size distributions of approximately 10-20 percent are prepared using divalent germanium (Ge) precursors and trioctylphosphine-tellurium (TOP-Te). GeTe nanocrystals with widely varying sizes are prepared using Ge precursors with different reduction kinetics. Particles of all sizes are confirmed to exist in the rhombohedral phase characteristic of the ferroelectric state.

The evolution of a polarization domain structure is examined in GeTe nanocrystals with average sizes of 8, 100, and 500 nm. Dark-field TEM and electron diffraction experiments

indicate a monodomain state for the 8 nm particles, a transition to a bidomain state for the 100 nm particles, and the emergence of a polydomain state for the largest (500 nm) particles.

The size-dependent ferroelectric ordering in 8, 17, 100, and 500 nm average diameter GeTe nanocrystals is examined using synchrotron x-ray diffraction, Raman scattering, and atomic-resolution TEM. Rietveld refinement of room-temperature synchrotron diffraction patterns indicates a monotonic decrease in the lattice constant and the rhombohedral angular distortion of the unit cell with decreasing particle size, and temperature-resolved synchrotron diffraction experiments demonstrate a reversible rhombohedral-cubic ferroelectric phase transition. Raman scattering confirms the broken inversion symmetry of particles of all sizes and indicates a substantial displacive component of the phase transition down to the smallest sizes studied. In addition, analysis with atomic-resolution TEM suggests the preservation of a substantial linear component of the ferroelectric polarization.

Individual nanocrystals of GeTe with an average diameter of 8 nm and nanocubes of $BaTiO_3$ with an average side length of 10 nm are then imaged with aberration-corrected TEM and off-axis electron holography. These experiments suggest that the polarization exists in a largely linear, monodomain state, in contrast with theoretical reports indicating a transition towards a toroidal polarization state. In addition, analysis with PFM demonstrates the preservation of polarization switching at room temperature in $BaTiO_3$ nanocubes smaller than 10 nm in size and indicates a transition to a superparaelectric state below a critical length scale of approximately 5-10 nm.

These studies of individual GeTe and $BaTiO_3$ nanocrystals are complimented with atomic pair distribution function analyses, which indicate correlations among ferroelectric dipoles that are stronger in the case of GeTe, but reduced relative to bulk material. Comparisons between GeTe and $BaTiO_3$ nanomaterials of comparable size and between $BaTiO_3$ nanocrystals with varying morphologies indicate strong contributions to ferroelectric size effects due to both electrostatics and internal strain and demonstrate a shape-dependence of the stability of the ferroelectric state.

Overall, these experiments demonstrate the surprising stability of a coherent, linear, and monodomain polarization state in the smallest ferroelectric nanomaterials ever characterized. The overall polarization is weakened significantly due to a combination of both surface-induced strains and depolarization effects, although the local ferroelectric distortions in both GeTe and $BaTiO_3$ nanocrystals remain close to the bulk values. Although limited evidence for a rotational tendency of the polarization is observed in the atomic-resolution TEM studies, no clear evidence for a vortex polarization state was found, in contrast with theoretical expectations.

To my parents

Gary and Clare Polking

For their unwavering love and support, keenly felt even 2000 miles away from home

And

My sister

Kathryn Polking

Who set me on the path to success so many years ago

Table of Contents

Introduction iv

Acknowledgments vii

Chapter 1. Controlled Synthesis of Germanium Telluride (GeTe) Nanocrystals 1

1.1 Introduction 1

1.2 Materials and Methods 2

1.3 Results and Discussion 5

Chapter 2. Evolution of a Polarization Domain Structure in Germanium Telluride Nanostructures 9

2.1 Introduction 9

2.2 Materials and Methods 10

2.3 Results and Discussion 10

Chapter 3. Analysis of Size-Dependent Ferroelectric Ordering in Colloidal Germanium Telluride Nanocrystals 20

3.1 Introduction 20

3.2 Materials and Methods 21

3.3 Results and Discussion 25

3.3.1 Nanocrystal Synthesis 25

3.3.2 Atomic-Resolution Transmission Electron Microscopy 26

3.3.3 Synchrotron X-ray Diffraction Measurements of the Size-Scaling of the Polar Ordering and Phase Transition 30

3.3.4 Temperature-Dependent Raman Measurements 34

3.3.5 Discussion of Results 37

Chapter 4. Characterization of Ferroelectric Ordering in Individual Colloidal Nanocrystals 39

4.1 Introduction 39

4.2 Materials and Methods 42

4.3 Results and Discussion 46

4.3.1 Atomic-Resolution TEM Imaging of Individual GeTe Nanocrystals 46

4.3.2 Atomic-Resolution TEM Imaging of Individual $BaTiO_3$ Nanocubes 48

4.3.3 Off-Axis Electron Holographic Imaging of Ferroelectric Polarization in $BaTiO_3$ Nanocubes 53

4.3.4 Piezoresponse Force Measurements of Individual $BaTiO_3$ Nanocubes 56

4.3.5 Discussion of Results 58

Chapter 5. Comparing GeTe and $BaTiO_3$: Understanding the Mechanisms for Ferroelectric Size Effects 59

5.1 Introduction 59

5.2 Materials and Methods 61

5.3 Results and Discussion 62

5.3.1 Amorphous and Crystalline GeTe Nanoparticles 62

5.3.2 Fourier Transform Infrared Spectroscopy of GeTe Nanoparticles 63

5.3.3 Atomic Pair Distribution Function Measurements of GeTe Nanocrystals 67

5.3.4 Atomic Pair Distribution Function Measurements of $BaTiO_3$ Nanocrystals 70

5.3.5 Discussion of Results 72

References 75

Introduction

Since the discovery of ferroelectricity nearly nine decades ago, polar materials have emerged as a subject of widespread fundamental and practical interest. Polar materials, as we shall define them here, are those materials that undergo spontaneous symmetry-breaking distortions from a higher symmetry "prototype" structure that lead to local electric dipole moments with long-range ordering. Adjacent local moments may be oriented antiparallel with respect to one another, leading to an antiferroelectric phase, or may be aligned in parallel, leading to a ferroelectric or pyroelectric phase with a macroscopic polarization[1].

Ferroelectrics in particular, the spontaneous polarization of which may be reoriented under an applied electric field, have attracted great interest for nonvolatile information storage devices and many other applications[2,3]. Practical applications of these materials require room-temperature stability of the polar phase and a detailed understanding of polar ordering at the nanoscale. Despite voluminous work on ferroelectric nanomaterials, the questions of polar phase stability and the fundamental nature of the polar state in low-dimensional materials have remained elusive. Early reports indicated complete quenching of the polar state due to depolarization fields, surface layers, and other effects[4,5]. More recent studies[6-8] on ensembles of ferroelectric perovskite nanoparticles using atomic pair distribution function analysis combined with detailed Raman and Rietveld refinement experiments have painted a more complex picture of nanosized ferroelectrics, according to which the overall distortion of the particle is diminished, as seen in earlier work, but the local ferroelectric distortions are enhanced relative to bulk material. Recent theoretical work has added a new dimension to this story: The emergence of stable toroidal polarization patterns in ferroelectric nanodots[9,10] has been predicted using first-principles calculations. Despite intense research over the last few decades, conclusive answers to the question of the fundamental nature of ferroelectric ordering in low-dimensional nanosystems have been hindered in part by the lack of high-quality, monocrystalline ferroelectric nanomaterials[11-14] and the paucity of methods for the analysis of individual nanocrystals at a local scale. Experimental confirmation of polar phase stability and phase transitions in unconstrained low-dimensional nanosystems is noticeably lacking, and characterization of polar ordering at a local, unit-cell level in these systems is practically nonexistent. In addition, the mechanisms governing the nature of the polar state in these systems are not entirely understood, with literature reports pointing to depolarization fields, internal strains, and other driving forces for the size-dependence of polar ordering[15-17].

This study, motivated by these holes in current experimental knowledge, focuses on three basic questions of fundamental importance to this field. The first, and most basic, of these questions concerns the feasibility of synthesizing high-quality, monocrystalline, and size-controlled nanocrystals of a polar material. The second question focuses on the ultimate size-stability of the polar phase, the occurrence of polar phase transitions in these materials, and the size-dependence of the overall polar order parameter. The final question regards the nature of polar ordering in these systems at the unit-cell scale.

In order to explore the first of these questions, colloidal chemistry methods have been extended to the synthesis of nanocrystals of polar materials. Colloidal techniques, which have emerged as a powerful tool for the exploration of novel size-dependent phenomena in optical, magnetic, and other functional nanomaterials, provide an economical, highly scalable, and low-temperature route to a wide range of materials[18,19]. These methods, which rely on the decomposition of reactive organometallic precursors in the presence of long-chain organic surfactant molecules, also provide a means of producing nanomaterials of uniform, controlled sizes with variable morphologies[20]. While colloidal chemistry has enjoyed many successes in the preparation of functional nanomaterials, these successes have not extended to the synthesis of a polar nanomaterial of controllable size. Previously, the synthesis of highly polydisperse nanorods of $BaTiO_3$ with lengths of several microns remained the only example of a colloidal polar nanomaterial[13]. To remedy this dearth of nanocrystalline ferroelectrics, this study has focused on the synthesis of colloidal nanocrystals of the IV-VI semiconductor GeTe. This material, with only a single anion and cation per primitive unit cell, is the simplest possible material that may undergo a polar phase transition and thus serves as a convenient basis for this study[1]. In addition, while the controllable colloidal synthesis of perovskite oxides—the family to which most classic polar materials belong—has remained elusive, considerable progress has been made on the synthesis of other IV-VI semiconductors, including the closely related materials PbTe and SnTe[21,22].

Following the synthesis of monodisperse nanocrystals of several sizes, analysis of polar ordering in this system has focused sequentially on three relevant length scales. The first experiments have been conducted at the ensemble level on colloidal nanocrystals of the simple model ferroelectric GeTe using *in-situ* temperature-dependent x-ray and Raman scattering. These experiments provide complementary pathways to the confirmation of polar phase stability and the existence of a polar phase transition and to the elucidation of the size-scaling of the overall ferroelectric distortion in nanocrystal ensembles.

Characterization of the system has then been extended to the single-particle level to provide direct confirmation of polar behavior, free from ensemble averaging. Direct measurements of the structural distortion leading to polar ordering, enabled by recent advances in aberration-corrected transmission electron microscopy (TEM), have provided evidence of an overall, coherent ferroelectric distortion in individual nanocrystals of the model ferroelectric GeTe. These experiments have also indicated a transition from a polydomain to a monodomain state with decreasing particle size in analogy with ferromagnetic materials.

Finally, characterization of individual nanocrystals has been extended down to atomic length scales using aberration-corrected TEM and off-axis electron holography. Using exit-wave reconstruction of image series obtained by aberration-corrected TEM, atomic column positions have been directly extracted to probe variations and correlations of local structural distortions, providing a local picture of ferroelectric ordering at the single-particle level. Nanocrystals of both GeTe, which exhibits nearly metallic conduction[23], and $BaTiO_3$, a traditional insulating oxide ferroelectric, have been analyzed to deconvolute the contributions of depolarizing fields and surface-induced strains to the size-dependence of ferroelectric ordering. The correlations

among ferroelectric dipoles have also been analyzed with complimentary atomic pair distribution function studies.

Overall, these experiments indicate that a coherent, linear polarization state can be stable even at nanometer length scales in both insulating and conductive ferroelectrics, in contrast with theoretical expectations of a toroidal state[10,24]. The linear order, however, is disrupted by decoherence of ferroelectric dipoles and coherent local polarization rotations that reduce the magnitude of the polar distortion. This arises from both internal strains and from depolarization fields, pointing to a picture of the driving force for ferroelectric size effects that is more complex than previously believed.

Acknowledgements

There are many to whom I owe my deepest gratitude for the ultimate success of this project, which came after a year of fruitless work on the synthesis of $BiFeO_3$ and many more frustrating months spent developing the synthesis of GeTe. First, I would like to thank my advisers, Prof. Ramesh and Prof. Alivisatos, for giving me the opportunity to learn to think as a scientist, develop my own scientific ideas, and largely chart the course of my own research. There are few places as conducive to the development of the tools for scientific thought as the laboratories of Prof. Ramesh and Prof. Alivisatos, whom I feel honored and privileged to have as mentors.

I would also like to acknowledge my other mentors—Dr. Yadong Yin, Dr. Dmitri Talapin, and Dr. Jonathan Owen—for imparting some of their immense wisdom to me during the early stages of my PhD. Their patient guidance was crucial to my early development as a scientist, and I continue to try to follow their example.

I would like to take this opportunity to acknowledge the numerous intellectual contributions of my collaborators to this work. Dr. Jeffrey Urban and Dr. Delia Milliron, along with Dr. Emory Chan, Marissa Caldwell, and Dr. Simone Raoux, lent their considerable expertise with x-ray analysis to the development of the *Nano Letters* manuscript and provided invaluable critical feedback during its composition. Dr. Haimei Zheng's careful and patient work on the TEM was instrumental in the analysis of the domain structure of the GeTe nanocrystals. Dr. Christian Kisielowski taught me much of what I know about advanced atomic-resolution TEM, and Dr. Joel Ager similarly played the role of patient teacher as I learned about Raman spectroscopy. Dr. Gabriel Caruntu and Shiva Adireddy at the University of New Orleans provided the beautiful $BaTiO_3$ nanocubes that were employed in the final phase of my graduate research, and Dr. Valeri Petkov of Central Michigan University and Dr. Myung-Geun Han of Brookhaven National Laboratory lent their considerable expertise in atomic pair distribution function analysis and off-axis electron holography, respectively.

I would be amiss if I did not recognize my colleagues in the Alivisatos lab, who have enriched my life immensely both scientifically and personally. The creativity and passion for science of my labmates have been truly inspiring. In particular, I would like to thank Dr. Prashant Jain for igniting my interest in optical phenomena, and Trevor Ewers, Charina Choi, Sassan Sheikholeslami, Katie Lutker, and many others for their friendship and support.

Finally, I would like to thank the National Science Foundation for providing my NSF Graduate Research Fellowship, which has substantially enhanced my quality of life as a graduate student. I would also like to recognize Avi Rosenzweig and the NSF-IGERT program for providing a further three years of fellowship support and the opportunity to interact with scientists across many different disciplines.

Chapter 1: Controlled Synthesis of Germanium Telluride (GeTe) Nanocrystals

1.1. Introduction:

Semiconducting IV-VI nanocrystals have received attention recently due to their strong quantum size effects[21,25,26] and rich array of phase transitions that influence their electronic, optical, and phononic properties[27,28]. The semiconductor germanium telluride (GeTe) in particular has garnered interest due to its reversible amorphous-to-crystalline phase transition[29,30] and ferroelectric phase transition, which leads to a spontaneous polarization along a <111> axis below ~625 K[31-33]. This polar distortion also leads to the formation of polarization domain boundaries, which influence its mechanical, electronic, thermal, and other properties[34]. The simplest possible ferroelectric, GeTe provides a simple model system for the study of polar ordering phenomena at reduced dimensions. Although the high bulk carrier density of GeTe hinders direct measurement of the spontaneous polarization, the interplay of structural, optical, electronic, and other properties make this an important system for further study.

Despite interest in GeTe, methods for the synthesis of high-quality nanomaterials of GeTe are relatively unexplored, and little is currently known about its nanoscale properties. While vapor-phase syntheses of GeTe nanowires and solution-phase syntheses of micron-scale crystals and amorphous nanoparticles have been reported[35-39], the size scales of these materials are far from the quantum regime, and the formation of crystalline GeTe of controlled sizes has remained elusive. In addition, while colloidal chemistry has proven highly successful for the synthesis of semiconducting and metallic nanomaterials with tunable optical, magnetic, and other functionalities, few syntheses of low-dimensional nanostructures of materials exhibiting spontaneous polar ordering exist[12-14], hindering fundamental study of polar phenomena at nanoscale dimensions. In this chapter, a simple and highly adaptable colloidal synthesis of GeTe nanocrystals of sizes ranging from 8 to 100 nm is described. These nanocrystals have narrow size distributions and exhibit the rhombohedral structure characteristic of the polar phase down to particle sizes of less than 10 nm.

1.2. Materials and Methods:

Reagents and Reagent Preparation:

Germanium(II) chloride-1,4 dioxane complex (1:1), tellurium powder (30 mesh, 99.997 %), 1-dodecanethiol (1-DDT, >98 %), anhydrous 1,2 dichlorobenzene (DCB, 99 %), 1-octadecene (ODE, 90 %), oleylamine (70 %), squalane (99 %), anhydrous acetonitrile (99.8 %), and anhydrous chloroform (99 %) were purchased from Sigma-Aldrich. Bis[bis(trimethylsilyl)amino]Ge(II) ($(TMS_2N)_2Ge$) was purchased from Gelest, and trioctylphosphine (TOP, 97 %) was purchased from Strem. A 10 wt% stock solution of Te (shot, 99.999% from Sigma-Aldrich) in TOP for 8 nm particles was prepared by dissolving Te shot in TOP at room temperature. Stock solutions of Te in TOP with a concentration of 10 wt% were prepared for all other particles under argon on a Schlenk line by dissolving Te powder in TOP at 200 ˚C for two hours. These stock solutions were then stored in an argon glovebox. Squalane, 1-octadecene, and oleylamine were dried under vacuum at 110 ˚C for 1 hour, and 1-dodecanethiol was dried under vacuum at 90 ˚C for 1 hour. All other reagents were used without further preparation.

Synthesis of 8 nm GeTe Nanocrystals:

6 mL of dried squalane was added to a 50 mL 3-neck reaction flask in a glovebox. The flask was then sealed and attached to a Schlenk line under constant argon flow. In the glovebox, 0.1 g of $(TMS_2N)_2Ge$ was mixed with 1 mL of TOP and 1 mL of dried squalane and added to the flask at room temperature. Then, 0.03 g of dried 1-DDT was mixed with 1.5 mL of a 10 wt% TOP-Te solution. The squalane/TOP/$(TMS_2N)_2Ge$ solution was then heated to 230 ˚C under constant argon flow and rapid stirring, and the 1-DDT/TOP-Te solution was immediately injected. After injection, the temperature dropped to ~220 ˚C and was held at this value for 1.5-2 minutes. The flask was then rapidly cooled with compressed air to room temperature.

Synthesis of 17 nm GeTe Nanocrystals:

3 mL of dried ODE and 3 mL of dried oleylamine were loaded into a 50 mL 3-neck reaction flask inside a glovebox. In the glovebox, 0.1 g of $(TMS_2N)_2Ge$ was mixed with 1 mL of dried 1-octadecene and 0.5 mL of TOP-Te. The reaction flask was sealed inside the glovebox and attached to a Schlenk line under argon flow. The flask was then heated to 250 ˚C under

constant argon flow and rapid stirring, and the $(TMS_2N)_2Ge$/TOP-Te injection solution was then rapidly injected. The reaction mixture was held at approximately 235 ˚C for 1.5 minutes and allowed to cool to room temperature.

Synthesis of 100 nm GeTe Nanocrystals:

1.5 mL of dried 1-DDT, 4.5 mL of DCB, and 10 mg of $GeCl_2$-dioxane were loaded into a 50 mL 3-neck reaction flask inside a glovebox. The reaction flask was sealed inside the glovebox and transferred to a Schlenk line under continuous argon flow. The reaction mixture was heated to 180 ˚C under argon flow and rapid stirring, and 0.7 mL of TOP-Te was then injected into the reaction mixture. The reaction mixture was held at approximately 177 ˚C for 2 minutes and allowed to cool to room temperature.

Cleaning Procedure:

The nanocrystals were transferred from the reaction vessel into vials under argon flow and cleaned under air-free conditions in a glovebox. In a typical cleaning procedure, ~2 mL of nanocrystal solution/suspension was mixed with 10-20 mL of anhydrous chloroform and an amount of anhydrous acetonitrile sufficient to induce flocculation. The particles were then centrifuged and redispersed in anhydrous chloroform with sonication. This centrifugation and redispersal procedure was repeated, and the particles were redispersed in chloroform.

Transmission Electron Microscopy:

Low-resolution transmission electron microscope (TEM) images were taken with an FEI Tecnai G2 Super Twin microscope operated at 200 kV and equipped with a LaB_6 filament. High-resolution TEM (HRTEM) images of the 8 and 17 nm particles were then taken with an FEI monochromated F20 UT Tecnai microscope with a field emission gun operated at 200 kV. TEM images of the 100 nm particles were taken using a Philips CM 300 microscope operated at 300 kV and equipped with a field emission gun. Measurements of particle sizes for size statistics were performed in Image-Pro Plus 4.5.

Powder X-ray Diffraction:

Powder x-ray diffraction (XRD) was performed with a Bruker AXS GADDS D-8 diffractometer (Co K_{α}, 1.79026 Å) operated at 45 kV and 35 mA. Scans were collected for 3000 seconds. The background signal from the plastic substrate was subtracted from the data collected for the nanocrystal films.

Rietveld Refinement:

Rietveld refinements for the 8 nm nanocrystals were completed with the program MAUD, v. 2.072. The refined parameters included three background parameters, the lattice constant, rhombohedral angle, atomic positions, B factors, and peak broadening.

1.3. Results and Discussion:

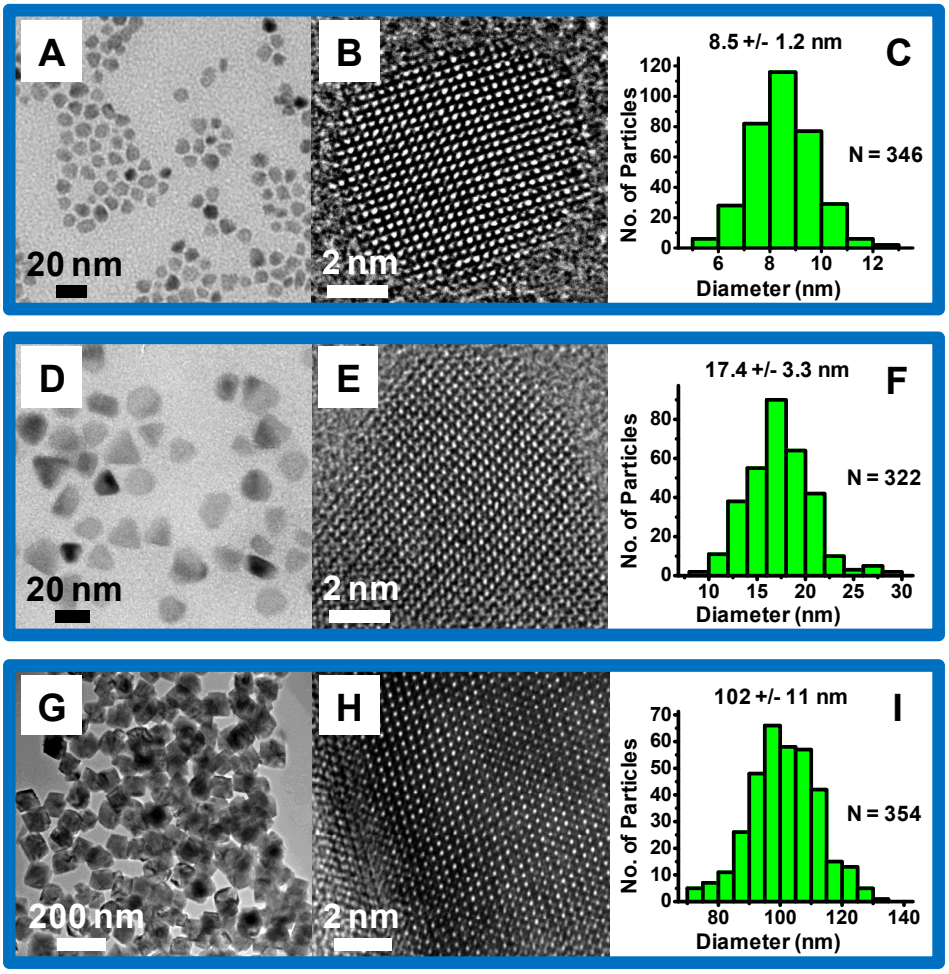

Figure 1.1. Transmission electron microscope (TEM) images and size statistics for GeTe nanocrystals. (A, B, C) Low-resolution TEM image (A), high-resolution TEM (HRTEM) image (B), and size statistics (C) for 8 nm GeTe nanocrystals; (D, E, F) low-resolution TEM image (D), HRTEM image (E), and size statistics (F) for 17 nm GeTe nanocrystals; (G, H, I) low-resolution TEM image (G), HRTEM image (H), and size statistics (I) for 100 nm GeTe nanocrystals. *N* is the number of particles measured.

GeTe nanocrystals with average sizes of 8, 17, and 100 nm were synthesized by reaction of the divalent germanium precursors Ge(II) chloride-1,4 dioxane complex and

bis[bis(trimethylsilyl)amino]Ge(II) ($(TMS_2N)_2Ge$) with trioctylphosphine-tellurium (TOP-Te). Phase-pure GeTe nanocrystals can be prepared in a variety of solvents, including 1,2 dichlorobenzene, 1-octadecene, phenyl ether, and others. The basic chemistry is also compatible with other surfactants, including 1-dodecanethiol, oleylamine, and phosphonic acids.

Nanocrystals with an average diameter of 8 nm were synthesized by the reaction of $(TMS_2N)_2Ge$ with TOP-Te in the presence of 1-dodecanethiol and excess trioctylphosphine at 230 °C, and nanocrystals with a 17 nm average diameter were prepared using the same precursors in the presence of oleylamine at 250 °C. The synthesis of nanocrystals with an average size of 100 nm was accomplished through the use of $GeCl_2$-dioxane complex and TOP-Te in the presence of 1-dodecanethiol at 180 °C. Prior to the syntheses, solvents were dried and degassed where appropriate, which was found to be crucial to the production of phase-pure GeTe.

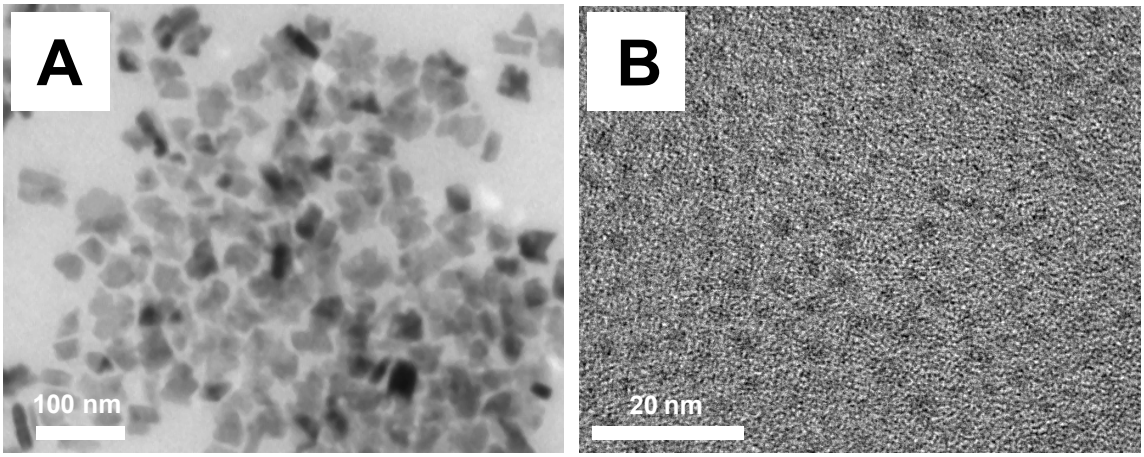

Figure 1.2. Transmission electron microscope images of Ge(0) nanocrystals formed through reduction of Ge(II) precursors with oleylamine. (A) Image of ~15 nm Ge(0) nanocrystals formed through reduction of $GeCl_2$-dioxane complex; (B) image of ~3 nm Ge(0) nanocrystals formed through reduction of bis[bis(trimethylsilyl)amino]Ge(II).

Typical transmission electron microscope (TEM) images for 8, 17, and 100 nm nanocrystals are shown in Figure 1.1. High-resolution TEM (HRTEM) imaging indicates that particles of all sizes are crystalline, and size statistics collected on samples of over 250 particles demonstrate size distributions of 10-20 percent, typical values for many colloidal syntheses.

The production of GeTe nanocrystals in two size regimes is facilitated by the use of two precursors, $GeCl_2$-dioxane complex and $(TMS_2N)_2Ge$, with vastly different reaction kinetics.

The latter precursor often yielded nucleation within several seconds in many different surfactant/solvent systems whereas the former reacted sluggishly, if at all, under the same reaction conditions. Both precursors are readily reduced in the presence of primary amines and alkanethiols to yield Ge(0) nanocrystals. $GeCl_2$-dioxane reacts sluggishly with pure oleylamine at 300 °C and produces germanium nanocrystals with an average size of approximately 15 nm (Figure 1.2A); reduction of $(TMS_2N)_2Ge$ under the same reaction conditions results in rapid nucleation of ~3 nm particles (Figure 1.2B). Similar trends are observed at lower temperatures. Although the precise reaction mechanism is not fully understood, this large increase in the Ge(II) reduction rate may contribute to the increase in particle nucleation rate and decrease in diameter from $GeCl_2$-dioxane to $(TMS_2N)_2Ge$, consistent with a previous study indicating the vital role of Ge(II) reduction kinetics in GeTe formation[38].

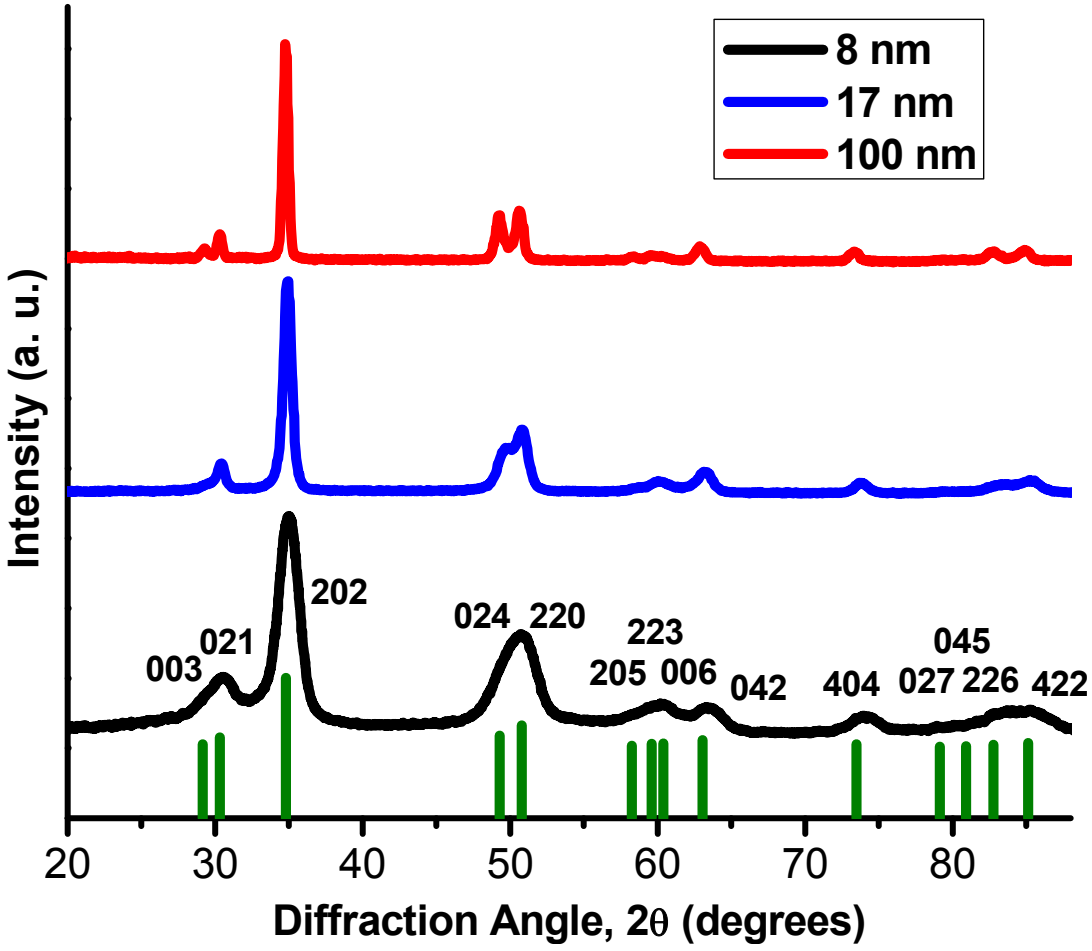

Figure 1.3. Powder x-ray diffraction patterns for 8, 17, and 100 nm GeTe nanocrystals. The patterns indicate the presence of phase-pure GeTe in the rhombohedral R3m (160) space group.

Powder x-ray diffraction (Figure 1.3) confirms the presence of phase-pure GeTe. The polar phase transition in GeTe from a rock salt structure to a rhombohedral structure results in the splitting of the 111 and 220 diffraction lines (in the cubic indexing system) into 003-021 and 024-220 doublets (in the rhombohedral indexing system)[32,33]. The XRD patterns of the 17 and 100 nm particles exhibit clear splitting of the 111 and 220 doublets characteristic of the rhombohedral phase. Significant peak broadening for the 8 nm particles, however, complicates determination of the material phase, necessitating analysis by Rietveld refinement (Figure 1.4). This analysis confirms the presence of the rhombohedral phase with a rhombohedral angle of approximately 88.5°. Multiple trials consistently indicated a rhombohedral distortion.

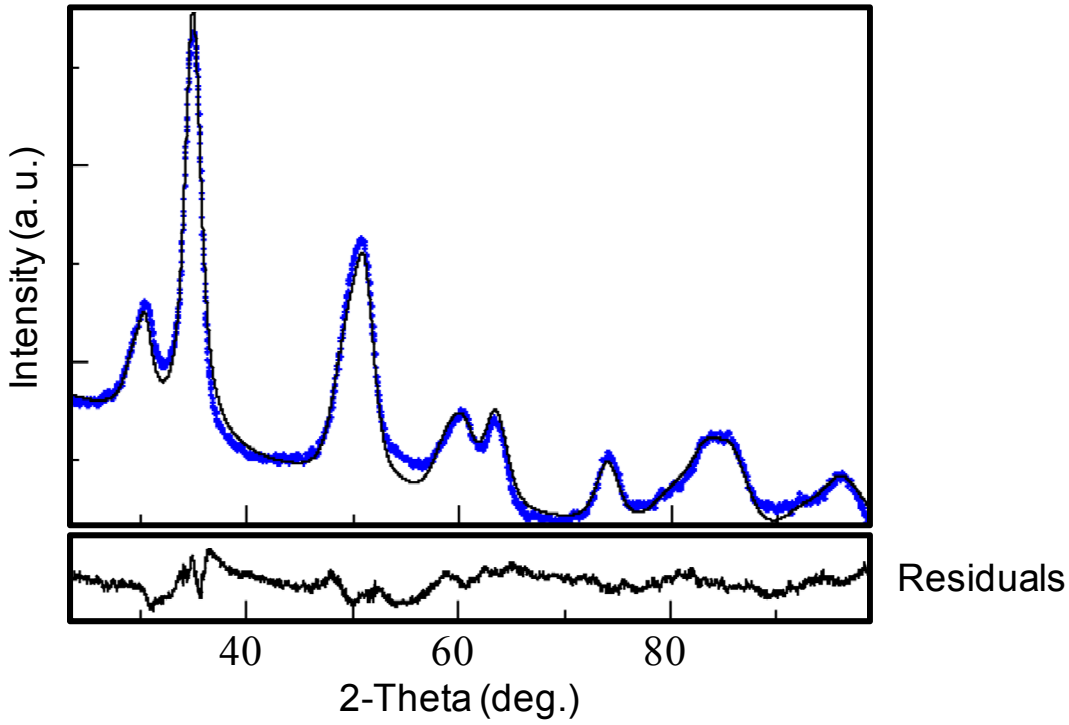

Figure 1.4. Rietveld refinement for the 8 nm GeTe nanocrystals. The Rietveld fit indicates a rhombohedral angular distortion of approximately 88.5°.

This chapter demonstrates the synthesis of nanocrystals of the semiconductor GeTe with controlled sizes and narrow size distributions using colloidal techniques. Divalent Ge precursors with drastically different reduction kinetics were employed to produce GeTe nanocrystals over a broad range of sizes. Analysis with powder x-ray diffraction indicates that particles of all sizes exist in the rhombohedral phase characteristic of the ferroelectric state, suggesting that some degree of ferroelectric order is maintained down to nanometer length scales.

Chapter 2: Evolution of a Polarization Domain Structure in Germanium Telluride Nanostructures

2.1 Introduction:

The presence of domains having well-defined orientations of the order parameter is one of the most important and fundamental characteristics of ferroic materials[1,40]. The shape, relative orientation, and periodicity of ferroic domain boundaries exert an enormous influence on the macroscopic behavior of the order parameter, and these boundaries often exhibit material properties vastly different from the bulk material[41,42]. Size-dependent behaviors of ferroic domain structures have long been studied in thin-film samples, with a characteristic decrease in domain wall periodicity with decreasing film thickness[43].

Freestanding magnetic nanocrystals exhibit a transition from a monodomain state to a polydomain state with increasing crystal volume[44]. Significant work has recently been devoted to elucidating the analogous ferroelectric domain behavior in freestanding nanoscale crystals of the archetypal ferroelectric $BaTiO_3$[45-47]. These studies suggest a reduction in domain periodicity with decreasing side length similar to that observed in thin-film samples down to length scales of approximately 100 nm. The behavior of ferroelectric domain structures at nanometer length scales, however, has yet to be characterized experimentally, perhaps due to the paucity of high-quality single crystals of ferroelectric materials within this size regime. It is not clear to what length scale the domain scaling behavior observed for freestanding nanodots extends, and the fundamental nature of the polar state at these dimensions remains a subject of continuing controversy.

In this chapter, the evolution of the polarization domain structure in GeTe nanocrystals with average sizes of 8, 100, and 500 nm is examined using a combination of dark-field transmission electron microscopy and electron diffraction. A transition from a primarily monodomain state to a multidomain state is observed for length scales above ~30 nm, indicating a critical size scale for the emergence of a polarization domain structure.

2.2 Materials and Methods:

Synthesis of 8 and 100 nm GeTe Nanocrystals:

The synthesis and cleaning procedure for 8 nm and 100 nm GeTe nanocrystals are as described in Section 1.2.

Synthesis of Highly Faceted 500 nm Nanostructures:

For the synthesis of highly faceted 500 nm nanostructures, seed particles were first prepared by adding 10 mg of $GeCl_2$-dioxane to 1.5 mL of 1-DDT and 4.5 mL of DCB in a three-neck flask in a glovebox. 0.9 mL of TOP-Te was then combined with a solution of 0.15 g of $(TMS_2N)_2Ge$ in 0.9 mL of ODE. The $GeCl_2$/1-DDT/DCB mixture was then heated to 180 ˚C under argon, and 0.1 mL of TOP-Te was rapidly injected into the flask. After 2.5 minutes, 0.2 mL of the solution containing $(TMS_2N)_2Ge$ and TOP-Te was injected every 2 minutes until consumed. The reaction was then held at 180 ˚C for a further 10 minutes and allowed to cool to room temperature.

Transmission Electron Microscopy and Electron Diffraction:

Dark-field images and electron diffraction patterns for the 8 nm nanocrystals were taken using the TEAM 1 microscope, a modified FEI Titan 80-300 equipped with a field emission gun and a combined spherical and chromatic aberration corrector operated at 300 kV. Electron diffraction patterns and TEM images of the 100 nm particles and highly faceted 500 nm crystals were taken using a Philips CM 300 microscope operated at 300 kV and equipped with a field emission gun.

2.3 Results and Discussion:

Dark-field TEM and electron diffraction studies (Figures 2.1, 2.2, 2.3, and 2.4) reveal the size-dependent evolution from a primarily monodomain state to a state with multiple polarization domains. Many IV-VI materials form in low-symmetry structures with weak bonding along

certain crystallographic directions, leading to stacking faults, twin boundaries, and other defects[27,48]. GeTe in the rhombohedral phase forms {100} and {110} twin boundaries as well as inversion boundaries separating domains with different <111> polarization axes[34]. HRTEM investigations presented in Chapter 1 indicate that the 8 and 17 nm particles primarily consist of a single domain. Electron diffraction patterns of the 100 nm particles, in contrast, reveal splitting of diffraction spots consistent with the formation of {100} and {110} twin boundaries (Figure 2.2).

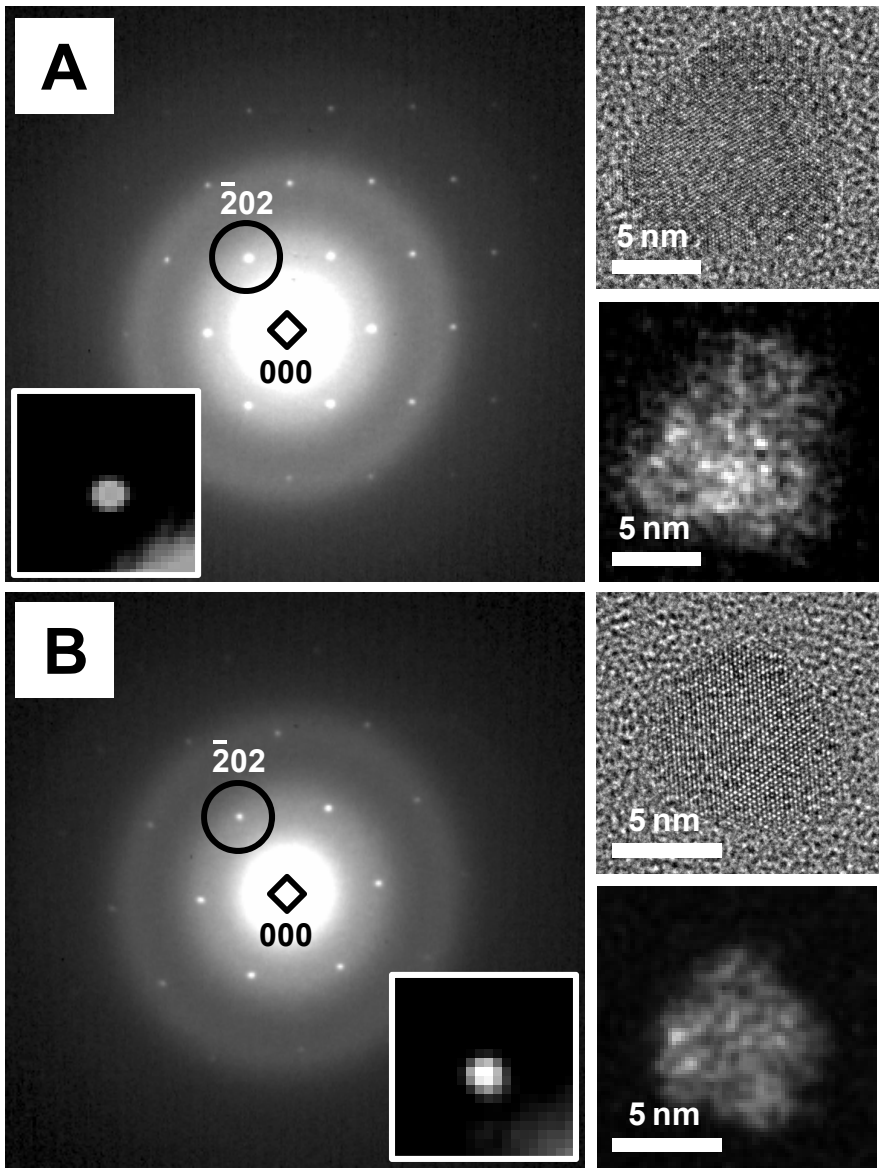

Figure 2.1. Electron diffraction patterns and dark-field TEM images of 8 nm GeTe nanocrystals. (A) Electron diffraction pattern of a single ~ 8 nm GeTe nanocrystal in the [111] zone axis orientation and corresponding dark-field TEM image taken with g = -220; no splitting of diffraction spots can be observed, indicating a monodomain state; (B) electron diffraction pattern of a single ~7 nm GeTe nanocrystal in the [111] zone axis orientation showing a single set of diffraction spots and corresponding dark-field TEM image taken with g = -220.

The change in lattice orientation across {100} and {110} domain boundaries leads to pronounced diffraction contrast in dark-field images[49]. The breakdown of Friedel symmetry for noncentrosymmetric crystals leads to differences in background contrast between inversion domains in dark-field images, and observation using complementary $\vec{g}$ and $-\vec{g}$ diffraction vectors results in a reversal of the relative contrast[49]. Dark-field TEM images of the 100 nm particles (Figure 2.2) reveal the presence of all three types of domain boundaries and the spatial relationships between domains. These images suggest that the 100 nm particles are largely bidomain. The electron diffraction patterns of the 8 nm particles (Figure 2.1), in contrast, contain a single set of spots, and dark-field TEM images reveal largely uniform contrast, confirming the monodomain structure.

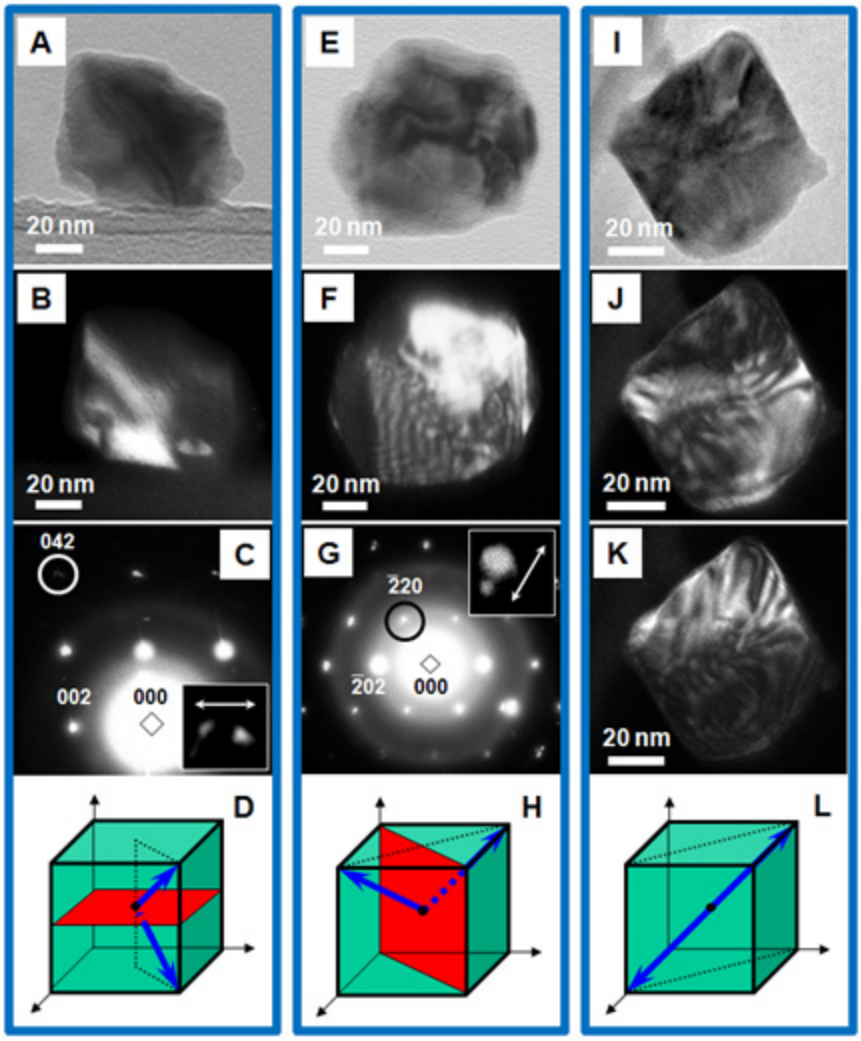

Figure 2.2. Polarization domains in 100 nm GeTe nanocrystals. (A, B, C) Bright-field TEM image (A), dark-field TEM image taken with $\vec{g} = 002$ (B), and corresponding electron diffraction pattern (C) consistent with a (100) twin boundary (109° domain wall); (E, F, G) bright-field TEM image (E), dark-field TEM image taken with $\vec{g} = \bar{4}22$ (F), and corresponding electron diffraction pattern (G) consistent with a (110) twin boundary (71° domain wall); (I, J, K) bright-field TEM image (I), dark-field TEM images taken with $\vec{g} = 002$ (J) and $\vec{g} = 00\bar{2}$ (K), respectively, indicating reversal of domain contrast characteristic of an inversion domain boundary (180° domain wall); (D, H, L) schematic illustrations of the relationships between polarization vectors across 109°, 71°, and 180° domain walls.

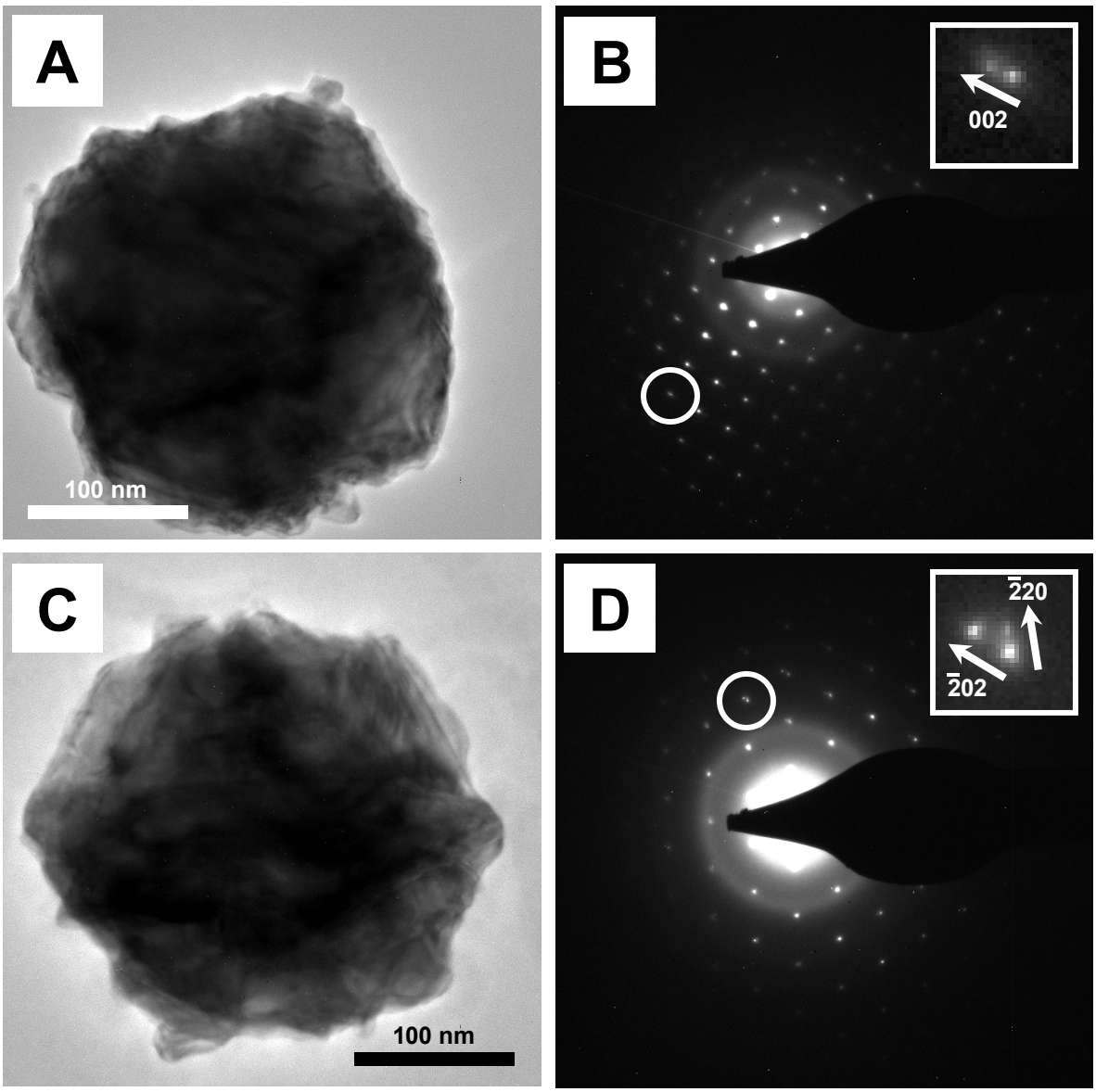

Figure 2.3. Transmission electron microscope (TEM) images and corresponding electron diffraction patterns of highly faceted GeTe nanostructures. (A) TEM image and (B) corresponding electron diffraction pattern of a particle near a [100] zone axis orientation. Splitting of diffraction spots parallel to 200-type *g* vectors can be observed, consistent with the presence of {100} twin boundaries; (C) TEM image and (D) corresponding electron diffraction pattern of a particle near a [111] zone axis orientation. Splitting of diffraction spots parallel to -220-type *g* vectors is apparent, indicating the presence of {110} twin boundaries.

To study the domain structure in still larger particles, additional precursor was injected into a solution containing seed particles, resulting in the formation of highly faceted nanostructures of regular diameter exhibiting surface features with a length scale of approximately 30 nm (Figure 2.3). Electron diffraction patterns of these crystals reveal similar splitting of diffraction spots indicative of {100} and {110} twin boundary formation (Figure 2.3) and exhibit no evidence of diffraction rings characteristic of polycrystals. Dark-field TEM imaging (Figure 2.4) shows a complex contrast pattern with many strongly diffracting regions, suggesting the presence of numerous polarization domains in the particles. This is consistent with the observed splitting of diffraction spots along multiple directions (Figure 2.3) indicating a polydomain state. Sequential addition of precursor to these structures thus results in the formation of networks of polarization domains rather than simple conformal addition of material to the particle surface. These observations suggest an average domain size of approximately 20-50 nm, consistent with literature reports on GeTe thin films[50].

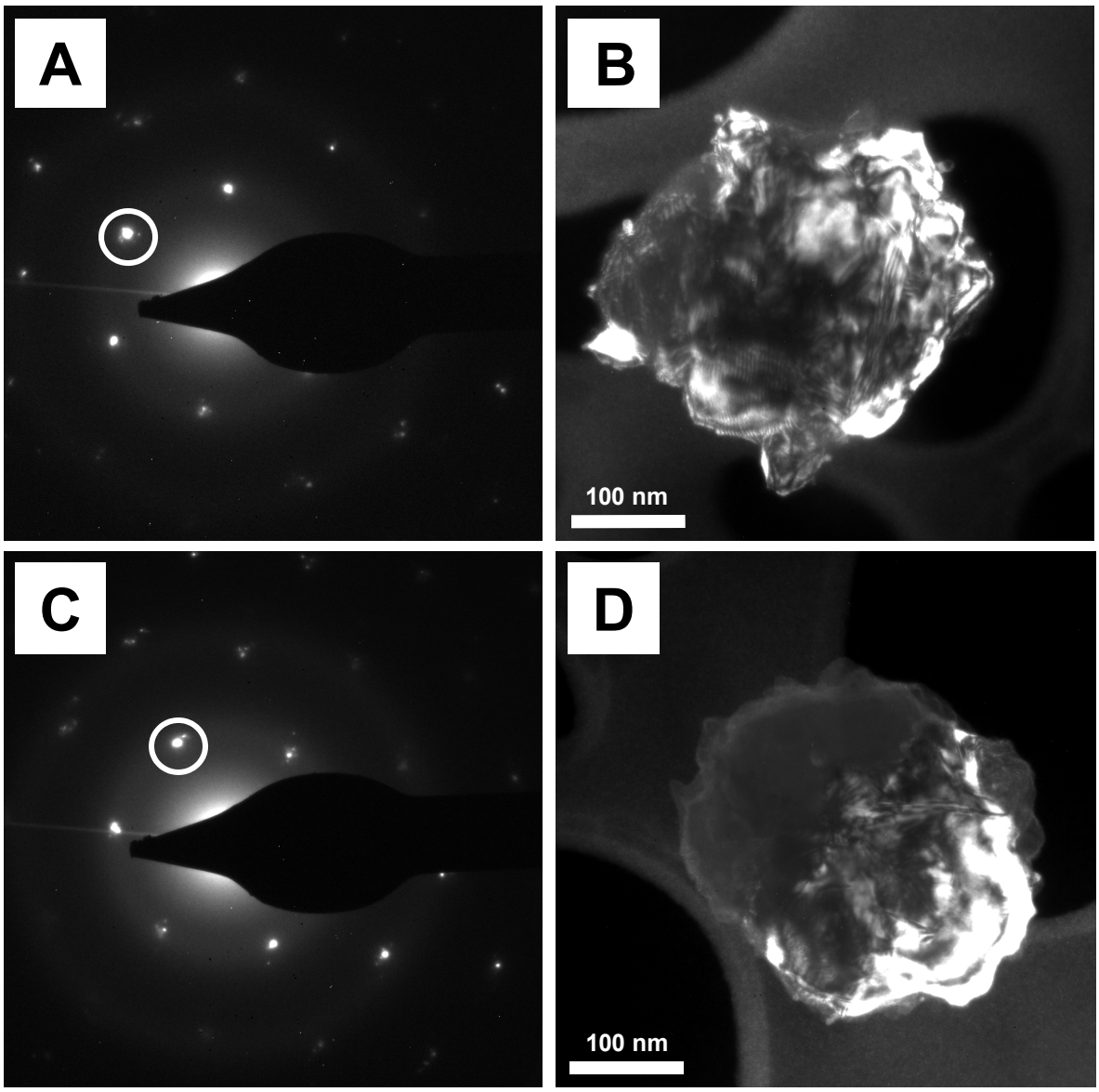

Figure 2.4. Electron diffraction patterns and corresponding dark-field TEM images of highly faceted GeTe nanostructures. (A) Electron diffraction pattern and (B) corresponding dark-field TEM image taken with g = -220 for a GeTe nanostructure near a [111] zone axis; (C) electron diffraction pattern and (D) corresponding dark-field TEM image taken with g = -220 of another GeTe nanostructure near a [111] zone axis. The background contrast is due to the lacey carbon support film.

The formation of domain boundaries in polar-ordered materials arises from a balance among electrostatic energy, elastic energy, and the energy of domain wall formation[1]. Periodic arrays of ferroelastic domain walls form to alleviate epitaxial strains in thin films[51] or strains imposed by surrounding grains in ceramic materials[52]. Ferroelastic domain formation is disfavored, however, in unconstrained crystals[53] but has nonetheless been observed in free-standing $BaTiO_3$ films due to the intrinsic tension imposed by a surface layer with different structural properties[53]. Domain formation in our GeTe nanocrystals may proceed via a similar mechanism. Although the high carrier density in GeTe may significantly screen the polarization, an additional electrostatic driving force for domain walls may be present. The formation of purely ferroelectric 180° walls[1] suggests an electrostatic influence on domain formation.

The scaling laws observed for freestanding ferroelectric nanodots[46] thus break down at length scales of around ~30 nm in GeTe, leading to the formation of a monodomain state below this critical length scale (Figure 2.5), as observed for magnetic nanocrystals. In this size regime, the energetic cost for the formation of a ferroelastic domain wall becomes too large to offset the associated reduction in strain energy. It should be noted, however, that the analogy between magnetic and ferroelectric nanocrystals is not strictly accurate, given the drastically larger wall thicknesses of magnetic materials (~50 nm) compared with ferroelectric materials (~2 nm)[1,44]. The formation of multiple polarization domains is thus not constrained by the finite thickness of the domains walls at the length scales of this experiment, and a multidomain state could in principle exist under appropriate electrical and mechanical boundary conditions. The ~30 nm length scale for the emergence of a multidomain state indicates that this finite wall thickness has little influence on the domain structure.

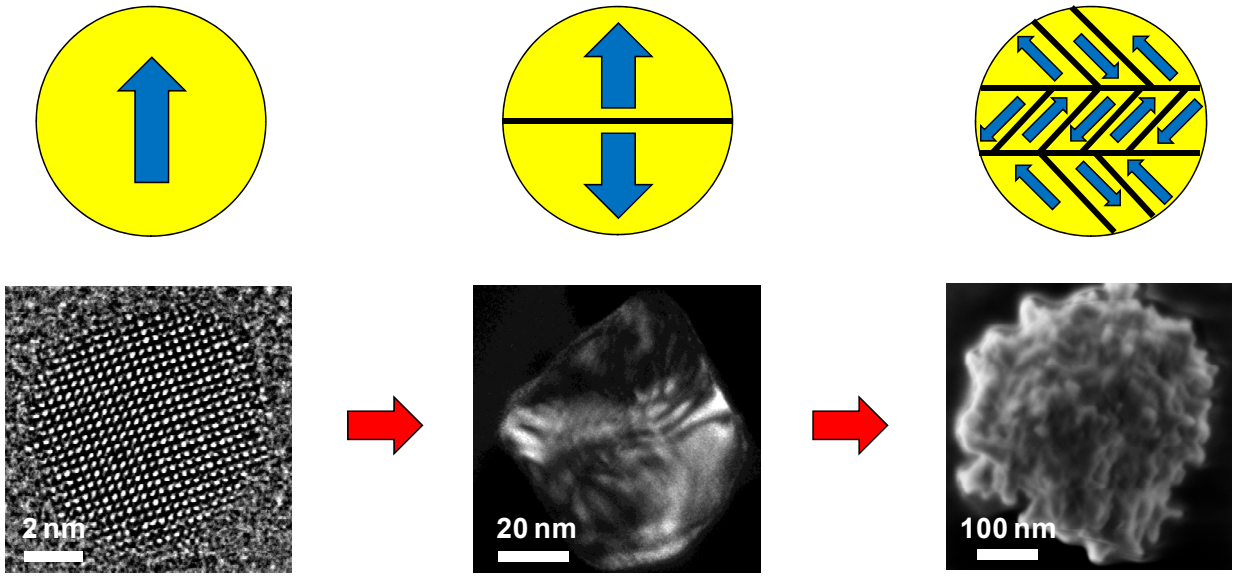

Figure 2.5. Schematic illustration of the emergence of a polarization domain structure in colloidal GeTe nanocrystals. The smallest (8 nm) particles exist in a monodomain state, which undergoes a transition to a bidomain state in nanocrystals of 100 nm average diameter. A polydomain state can be observed in GeTe nanocrystals with diameters of several hundred nanometers.

This chapter demonstrates the emergence of a polarization domain structure in nanocrystals of the semiconductor GeTe with controlled sizes and narrow size distributions. Below a characteristic size scale of ~30-50 nm a monodomain state emerges, as for ferromagnetic nanocrystals. The emergence of a polarization domain structure is attributed to a ferroelastic mechanism driven by long-range internal strain fields imposed by the particle surfaces. These results indicate the breakdown of the scaling laws observed by Schilling, Catalan, and others at length scales below ~30-50 nm[46,47].

Chapter 3: Analysis of Size-Dependent Ferroelectric Ordering in Colloidal Germanium Telluride Nanocrystals

3.1 Introduction:

Practical applications of ferroelectric nanomaterials require room-temperature stability of the polar phase and a detailed understanding of polar ordering at the nanoscale. As mentioned previously, the fundamental nature of the polar state in low-dimensional nanomaterials has long remained a subject of controversy, with conflicting literature reports indicating incoherent local polar distortions[7,8], the emergence of a toroidal polarization[9,10] or complete quenching of the polar state [4,5,54]. In addition, while considerable attention has focused on perovskite thin films, the nature of polar ordering in other classes of ferroelectrics, including the IV-VI family of materials, remains largely unexplored.

Germanium telluride has received much attention for its potential in phase-change memory devices[55], thermoelectrics[56], and other applications. A semiconductor with a band gap of 0.1 eV in the bulk[57], GeTe is also the simplest possible ferroelectric material[1], comprising one cation and one anion per primitive unit cell, making this material an interesting model system for the fundamental study of ferroelectricity. Below ~625 K, the cubic rock salt lattice of GeTe undergoes a spontaneous symmetry-breaking distortion into a rhombohedral structure (space group R3m), which yields a polar phase[33,58]. This distortion may be represented as an angular distortion of the unit cell with a concurrent displacement of the Ge sublattice[30,32], which generates a spontaneous polarization along a [111] axis of the original cubic lattice (Figure 3.1).

In this chapter, the size-dependent polar ordering in size-controlled nanocrystals of GeTe is examined in both ensembles and individual nanocrystals. Atomic-scale evidence is provided of a room-temperature polar distortion retained at over 70 percent of the bulk value in nanocrystals less than 5 nm in size using aberration-corrected transmission electron microscopy (TEM) and detailed Rietveld refinement studies. In addition, temperature-resolved synchrotron diffraction and Raman spectroscopy studies demonstrate a reversible size-dependent polar phase transition. The polar distortion arises via a polar phase transition that is displacive in nature. The observed size-dependence of the polar ordering is attributed to surface-induced internal strains. The work described in this chapter demonstrates the persistence of polar order at

nanometer dimensions and the preservation of a displacive, reversible ferroelectric phase transition in a low-dimensional nanomaterial.

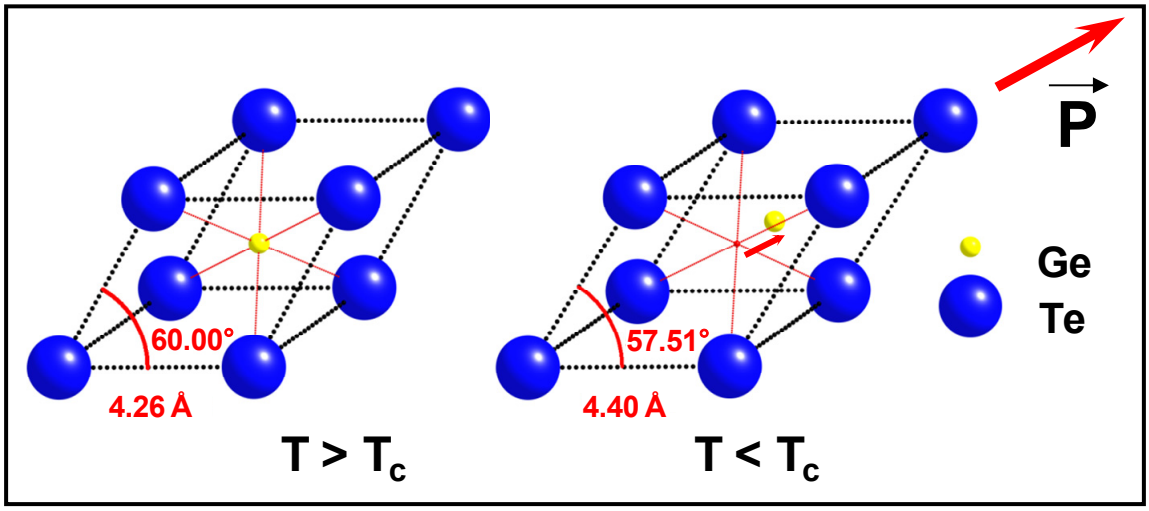

Figure 3.1. Schematic illustration of the spontaneous polar distortion in GeTe. The primitive unit cells for the cubic phase of GeTe (left), stable above ~625 K, and the low-temperature rhombohedral phase (right) are illustrated. The distortion results in a relative displacement of the Ge and Te sublattices that induces a spontaneous polarization (large red arrow) along a <111> axis. The displacement of the Ge cation is exaggerated for clarity. (Structural parameters obtained from ref. 30).

3.2 Materials and Methods:

Synthesis of 8, 17, and 100 nm GeTe Nanocrystals:

The synthesis and cleaning procedure for 8 nm, 17 nm, and 100 nm GeTe nanocrystals are as described in Section 1.2.

Synthesis of 500 nm GeTe Nanocrystals:

Prior to the synthesis, oleic acid (Sigma-Aldrich, 90%), 1-octadecene (Sigma-Aldrich, 90%) and oleylamine (Sigma-Aldrich, 70%) were dried by heating under vacuum at 110 ˚C for 1 hour. A 10 wt% solution of Te in TOP (TOP-Te) was prepared by dissolving Te powder (Sigma-Aldrich, 30 mesh, 99.997%) in trioctylphosphine (Strem, 97%) at 200 ˚C for 2 hours under constant argon flow. 1 mL of dried oleic acid, 1 mL of dried oleylamine, 3 mL of dried octadecene, and 50 mg of $GeCl_2$-dioxane were then added to a 50 mL 3-neck flask inside a glovebox, and the flask was sealed and attached to a Schlenk line under argon flow. The reaction mixture was then heated to 300 ˚C under constant argon flow and stirring. At 300 ˚C, 1 mL of TOP-Te was rapidly injected into the flask. The mixture was held at approximately 290 ˚C for 2 minutes and allowed to cool to room temperature. Particles were cleaned by centrifugation and redispersal in anhydrous chloroform.

Transmission Electron Microscopy:

Focal series for exit wave reconstruction were taken using the TEAM 0.5 and TEAM 1 microscopes at the National Center for Electron Microscopy, modified FEI Titan microscopes operated at 80 kV and equipped with high-brightness field emission guns, Gatan Image Filters, and CEOS aberration correction systems on the imaging side. Exit wave reconstructions were completed using focal series consisting of 20 images with the Gerchberg-Saxton algorithm in the program MacTempas X by Total Resolution. All focal series were recorded with a negative coefficient of spherical aberration (C_s) of -0.02 to -0.01 mm and a residual chromatic aberration of 0.002-0.003 mm.

Analysis of the rhombohedral angle for GeTe nanocrystals in a [100] orientation was performed in MacTempas X using the peak finding routine and lattice fitting tool. For this analysis, the fast Fourier transform (FFT) of the reconstructed phase image was first calculated, and an annular mask was applied to the resulting FFT to remove a portion of the background signal from the amorphous carbon support. An inverse Fourier transform was then calculated, and a background subtraction filter was applied to further remove background signal due to the amorphous carbon. The modulus of the Fourier transform of the resulting image was computed, and the diffraction peaks in the FFT were then fit using the peak finding tool. A best-fit lattice was then computed for the array of diffraction spots using the lattice fitting routine with a tolerance of 0.1.

Synchrotron X-ray Diffraction:

The powder diffraction file mentioned in the text (00-047-1079) was obtained from the ICDD PDF-2 database (2006 release). The rhombohedral diffraction lines mentioned in the text refer to the unit cell described in this file. Temperature-dependent x-ray diffraction measurements were conducted at beamline X20C at the National Synchrotron Light Source at Brookhaven National Laboratory. The beamline is equipped with a high-throughput synthetic multilayer monochromator and delivers 10^{13} photons/s at a wavelength of 1.797 Å. The endstation includes a BN heater stage, and samples were heated in a purified He atmosphere. The intensity of diffracted x-ray peaks was recorded over a 2-theta range of 15˚ using a fast linear diode array detector which was centered at either 2-theta = 31˚ or 51˚ for study of the 003/021 and 024/220 doublets, respectively. Heating and cooling rates were 1 K/s.

Peak positions of the 024/220 doublet were fit with a double Gaussian expression using the Multipeak Fitting package in Igor Pro 6.1. The relative area of the 024 peak with respect to the 220 peak was constrained to within ±10 %. The doublet was considered to have collapsed when the least squares fit failed to converge using the above constraint or when the chi squared values of the fits diverged. The resulting single peak was fit using a single Gaussian expression.

Samples of GeTe nanocrystals of similar sizes to those presented in Figure 3.2 were prepared by spin coating a dispersion of the nanocrystals in chloroform onto a silicon substrate. The resulting nanocrystal films were subsequently coated with ~10 nm of amorphous SiO_2 using RF sputtering.

Rietveld refinements were performed in the program X'Pert HighScore Plus by PANalytical Inc. A background determined by the method of Sonneveld and Visser using a granularity constant of 15 and a bending factor of zero was subtracted from the original data for presentation in Figure 3.6. Parameters refined to produce the Rietveld fits included a zero shift for 2-theta offset, a scale factor, the lattice constants and Ge atom Z position (sublattice displacement), and the Caglioti profile factor W (peak broadening). In addition, a polynomial background fit with three parameters was employed in the Rietveld refinements. A silicon standard was employed to account for instrumental broadening. The error values reported in Table 3.1 are those given by the fitting software.

Raman Spectroscopy:

Raman spectra were obtained using a home-built system with an argon ion laser operated at 514.5 nm with a laser power of 100 mW. A cylindrical lens with a spot length of several millimeters was used to minimize laser-induced heating. Spectra were collected using a SPEX triple spectrometer with a 2400 lines/mm diffraction grating and CCD. Low temperature (87-

280 K) measurements were done in a Janis VPF-100 liquid nitrogen cryostat with a silicon diode sensor. High-temperature (>280 K) measurements were taken in a home-built resistive heating cell under constant argon flow.

Batches of nanocrystals for Raman spectroscopy similar in size to those illustrated in Figure 3.2 were deposited on silicon substrates in an argon glovebox. Samples were coated with 50-100 nm of amorphous silica using an RF sputtering system to prevent loss of tellurium at high temperatures and minimize sintering.

Raman peaks were fit against a sloping background with PeakFit version 4 by Jandel Scientific using the Gauss*Lorentz fitting routine. For the 8, 17, and 100 nm particles, three peaks were used in the fitting procedure; for the 500 nm particles, two peaks were employed in the fit. For the spectra presented in Figure 3.8, a sloping background was subtracted in PeakFit using the NParm routine.

Modeling of the Crystal Structure:

To establish the directions of the polarization vectors shown in Figure 3.3, a model of the crystal structure was generated using the structural parameters provided in ref. 30 with the program ChemCraft, version 1.5. The polar distortion removes the equivalence of the different [110] zone axis orientations: For orientations with the polarization lying in the viewing plane, a staggering of the {111} planes can be observed, and for orientations with the polarization vector lying in a (110) plane perpendicular to the viewing plane, no such staggering is evident. However, a small displacement of the Ge sublattice along a [100]-type direction can be observed. The in-plane component of this displacement is parallel to the in-plane component of the polarization vector. To measure the sublattice displacement, line profiles for all rows were calculated in MacTempas X. The column positions were then extracted by fitting the peaks in these line profiles with Voigt functions in the program PeakFit version 4 by Jandel Scientific. Subsequent comparison with the aforementioned structural model enabled the assignment of the polarization vector directions shown in Figure 3.3.

The displacement of the Ge cation from the center of the unit cell can be determined in the left half of the particle from the staggering of {111} planes, which are perpendicular to the viewing plane. The Ge sublattice displacement is parallel to the trigonal axis (see Figure 3.1), which lies in the viewing plane, and is perpendicular to this set of {111} planes. The magnitude of the sublattice displacement is then one half of the difference between the spacings of adjacent pairs of {111} planes.

Simulations of the phase of the electron exit wave for Figure 3.4 were computed in MacTempas X. A model structure was generated using the structural parameters for the primitive unit cell in ref. 30 and custom MATLAB code. The simulated particle is a cube truncated along {111} planes, a shape consistent with [100], [110], and [111] projections, viewed

along the [1-10] direction. Multislice simulations were run using the same imaging parameters used for the acquisition of the experimental images (e. g. 80 kV accelerating voltage, C_s = -0.015 mm), 35 slices per unit cell (defined as the entire particle), and a G_{max} value of 2. Absorption was simulated using inelastic scattering factors, and Debye-Waller factors of 0.6 and 0.69 were used for Ge and Te, respectively, based on ref. 32.

3.3 Results and Discussion:

3.3.1. Nanocrystal Synthesis:

Spontaneous polar ordering was probed using several different populations of monodisperse colloidal GeTe nanocrystals synthesized as described in Chapter 1. Nanocrystals with average diameters of 8 and 17 nm were prepared by reaction of the divalent germanium precursor bis[bis(trimethylsilyl)amino]Ge(II) with trioctylphosphine-tellurium (TOP-Te). Nanocrystals with an average diameter of 100 nm were prepared by reaction of a precursor with slower nucleation kinetics, $GeCl_2$-1,4 dioxane complex, with the same tellurium source. In addition, particles of ~500 nm average size were prepared as a reference sample by reaction of $GeCl_2$-1,4 dioxane complex with TOP-Te at 300 °C in the presence of oleylamine and oleic acid surfactants. Typical TEM images of these nanocrystals are shown in Figure 3.2.

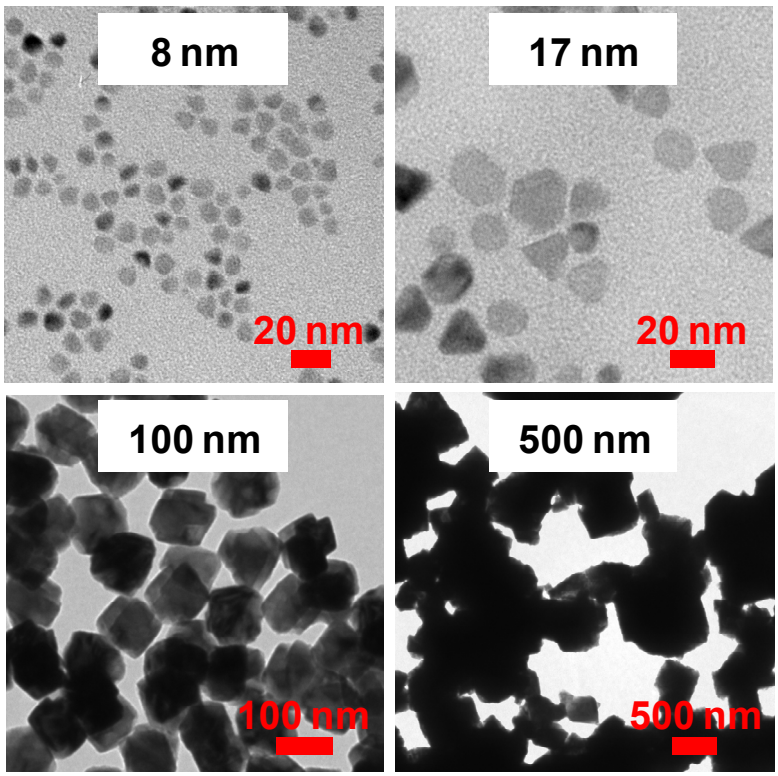

Figure 3.2. Transmission electron microscope images of the 8, 17, 100, and 500 nm GeTe nanocrystals studied in this chapter. The size distributions for all syntheses were between 10 and 20 percent.

3.3.2 Atomic-Resolution Transmission Electron Microscopy:

Atomically-resolved images of individual 4.5-8 nm GeTe nanocrystals provide direct evidence of the polar distortion in the smallest crystals synthesized. Exit wave reconstructions of high-resolution TEM (HRTEM) focal series obtained with the aberration-corrected TEAM 0.5 and TEAM 1 microscopes conclusively demonstrate the existence of both the spontaneous angular distortion and sublattice displacement in nanocrystals less than 5 nm in diameter at room temperature. Fast Fourier transform (FFT) analysis of the reconstructed phase image of a single ~4.5 nm particle viewed along the [100] zone axis (Figures 3.3A, 3.3B) illustrates an angular distortion of ~1.1°. Lattices fit to the FFTs of numerous particles using a least-squares procedure consistently indicated an angular distortion of 1-2° with an error of approximately 0.5° (Figure 3.5), consistent with synchrotron x-ray diffraction data described below. Analysis of reconstructed phase images also demonstrates the centrosymmetry-breaking sublattice

displacement: A phase image of a ~5 nm nanocrystal containing a (111) twin boundary (Figure 3.3C) shows two distinct sections in a [110] orientation with {111} planes perpendicular to the viewing plane. Separate germanium and tellurium columns can be distinguished in the image, and a sublattice displacement, manifested in a staggering of the {111} planes perpendicular to the polarization axis, measuring approximately 0.2 Å can be measured in the left section of the particle. This is reduced from the value of ~0.3 Å predicted theoretically[30]. No such staggering can be observed in the right section, consistent with a polarization vector that lies in a (110) plane perpendicular to the viewing plane. Additional reconstructed phase images of GeTe nanocrystals in a [110] orientation (Figure 3.4) indicate similar staggering of perpendicular {111} planes.

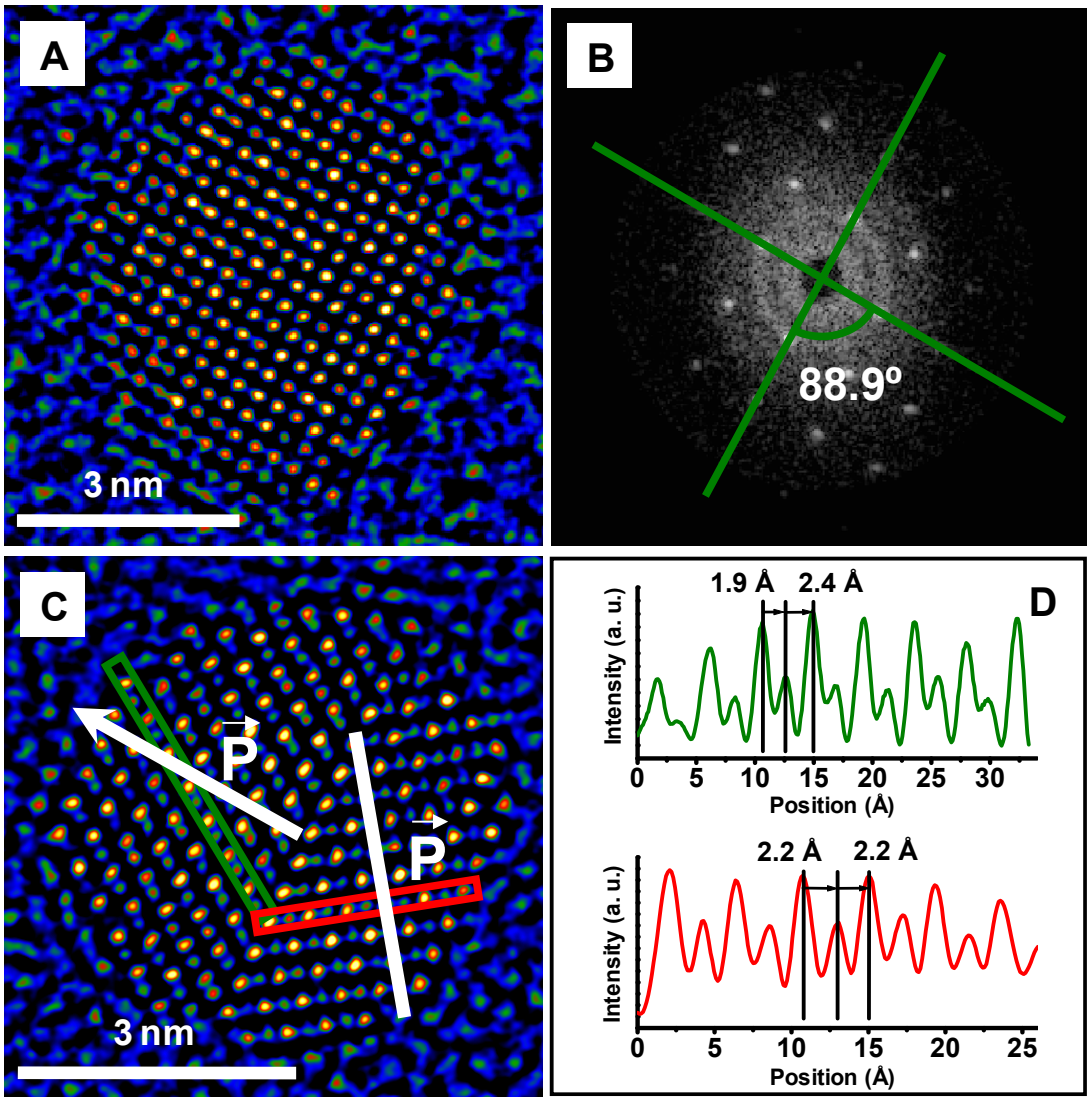

Figure 3.3. Atomically-resolved polar distortion in individual colloidal GeTe nanocrystals. (A) Phase of the reconstructed electron exit wave for a single ~4.5 nm GeTe nanocrystal in the [100] zone axis orientation; (B) corresponding fast Fourier transform demonstrating an angular distortion of ~1.1°; (C) phase of the reconstructed electron exit wave of a single ~5 nm GeTe nanocrystal with a (111) twin boundary; (D) corresponding line traces from the left (top) and right (bottom) sides. Separate Ge (smaller peaks) and Te (larger peaks) columns can be observed. The alternation of {111} plane spacings arising from the Ge sublattice displacement is clearly apparent in the left section of the particle. No such staggering can be observed on the right side of the particle, consistent with a polarization vector in a (110) plane perpendicular to the viewing plane.

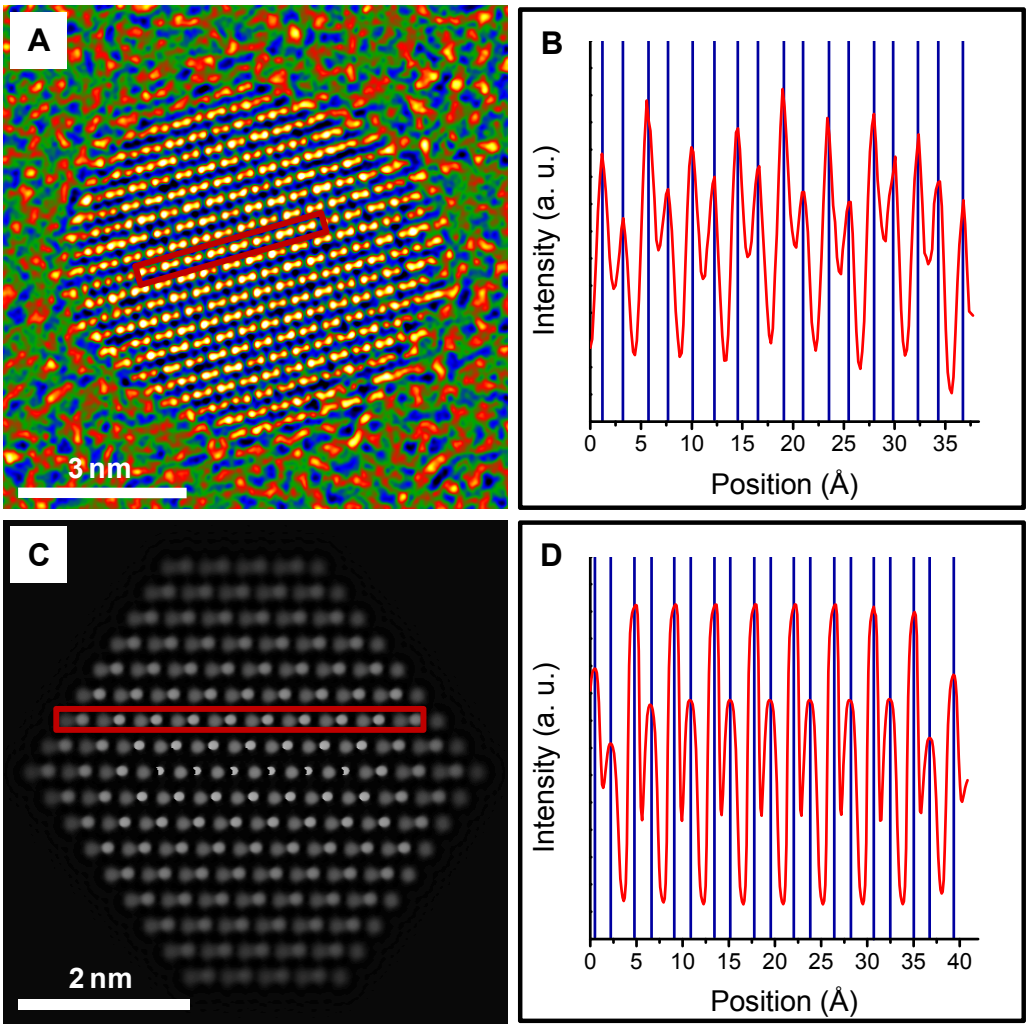

Figure 3.4. Sublattice displacement in experimental and simulated images of the phase of the electron exit wave. (A) Reconstructed phase image of a single GeTe nanocrystal in a [110] orientation. Coherent displacement of the {111} planes perpendicular to the image can be readily observed; (B) corresponding line trace illustrating the polar sublattice displacement; (C) simulated phase image for a GeTe nanocrystal with a coherent sublattice displacement; (D) corresponding line trace for the simulated image illustrating the polar sublattice displacement.

Moreover, these reconstructions are consistent with simulated phase images for a structure with a coherent sublattice displacement (Figure 3.4) generated using structural parameters from the literature[30]. Although the exact nature of spatial correlations is not entirely clear, these images suggest the persistence of a sizeable coherent, linear component of the polar

distortion, in contrast with literature reports indicating a transition to a toroidal state in both perovskite and GeTe nanodots[9,10].

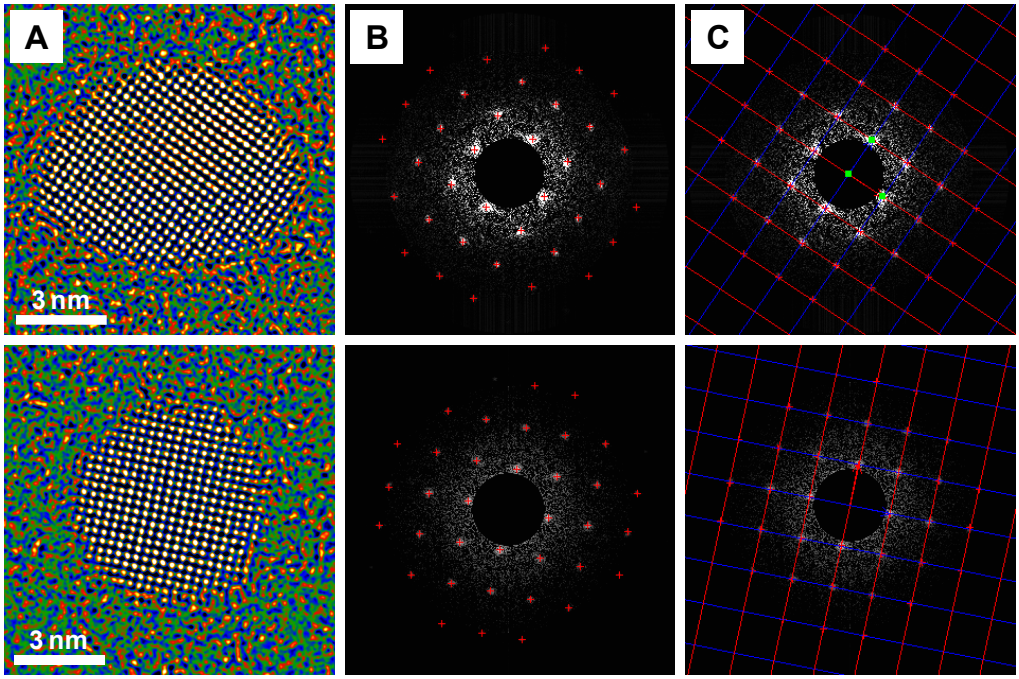

Figure 3.5. Rhombohedral angle measurements for individual GeTe nanocrystals in a [100] orientation. (A) Reconstructed phase images of GeTe nanocrystals in a [100] orientation; (B) corresponding fast Fourier transforms after background subtraction with fit positions of diffraction spots; (C) corresponding least-squares lattice fits to arrays of diffraction spots.

3.3.3. Synchrotron X-ray Diffraction Measurements of the Size-Scaling of the Polar Ordering and Phase Transition:

The existence of a polar phase transition in ensembles of nanocrystals was subsequently confirmed by temperature-resolved synchrotron x-ray diffraction (Figure 3.6). The cubic-to-rhombohedral phase transition in GeTe splits each of the 111 and 220 diffraction peaks (of the cubic system) into distinct 003/021 (parent 111) and 024/220 (parent 220) rhombohedral doublets. This splitting provides a clear signature of the structural phase transition. Ensembles of GeTe nanocrystals were analyzed using synchrotron powder x-ray diffraction. The resulting patterns indicate the presence of phase-pure germanium telluride in the rhombohedral phase

(Figure 3.6A). Analysis with Rietveld refinement (Table 3.1) indicates a monotonic increase in the rhombohedral angle (α) from 88.40 to 88.81 degrees with decreasing particle size, indicating >70 percent retention of the polar distortion down to dimensions of a few nanometers. In addition, the lattice constant (a) of the smallest (8 nm) nanocrystals (5.93 Å) is significantly reduced from the value of 6.023 Å found for the largest (500 nm) particles. The rhombohedral structural model consistently yielded a superior fit to the x-ray diffraction patterns for particles of all sizes, and the presence of an overall rhombohedral distortion in the smallest nanocrystals studied (8 nm) is further supported by our atomic-resolution TEM results indicating both an angular distortion of the cubic prototype lattice and a polar sublattice displacement.

Size (nm)	a (Å)	α (degrees)
8	5.93±0.03	88.81±0.02
17	5.96±0.01	88.72±0.01
100	6.017±0.005	88.599±0.004
500	6.023±0.005	88.395±0.005

Table 3.1. Structural parameters for GeTe nanocrystals obtained by Rietveld refinement of room-temperature synchrotron x-ray diffraction patterns. A substantial reduction in the lattice constant is evident for the smallest nanocrystals. In addition, a monotonic increase in the rhombohedral angle is observed.

Temperature ramps were then executed to follow the evolution of the 202 diffraction peak and of the 024/220 doublet. The 202 (rhombohedral) peak remains a singlet throughout the transition and may thus be used to monitor nanocrystallite size. During the temperature ramp, the width of this peak does not change significantly for the 100 nm and 500 nm nanocrystals. The peak does narrow, however, for the 17 nm and 8 nm diameter nanocrystals beginning around 495 K and 450 K, respectively, and this narrowing does not reverse upon cooling (Figure 3.7). This result is most consistent with sintering. For the 17 nm particles the width decreases by less than 10 %, reflecting only limited crystallite growth, while for the 8 nm particles the decrease is ~40 %. Analysis of the polar phase transition was thus restricted to the 17, 100, and 500 nm nanocrystals that exhibited little sintering during the measurement. For all particle sizes, the peak position moved smoothly to smaller diffraction angle over the entire temperature range (Figure 3.6C). In addition, no discontinuity is evident near the expected phase transition temperature (~625 K), consistent with previous reports[33,59] indicating a minimal volume change.

At room temperature, all nanocrystals exhibit splitting of the 024 and 220 diffraction peaks (Figures 3.6B, 3.6D) that decreases in magnitude for smaller particles, reflecting a reduced angular distortion. Upon heating the splitting decreases monotonically for all sizes as the nanocrystals approach the cubic phase. For the 100 and 500 nm particles, the splitting collapses gradually at lower temperatures, then more rapidly near the expected phase transition temperature (~625 K). At higher temperatures, the doublet peaks can no longer be resolved, reflecting the structural transformation to the cubic phase. For the 17 nm particles the doublet collapses more smoothly over the entire temperature ramp, with increasing rapidity starting as low as 425 K. Upon cooling, the doublets reappear, indicating recovery of the rhombohedral phase.

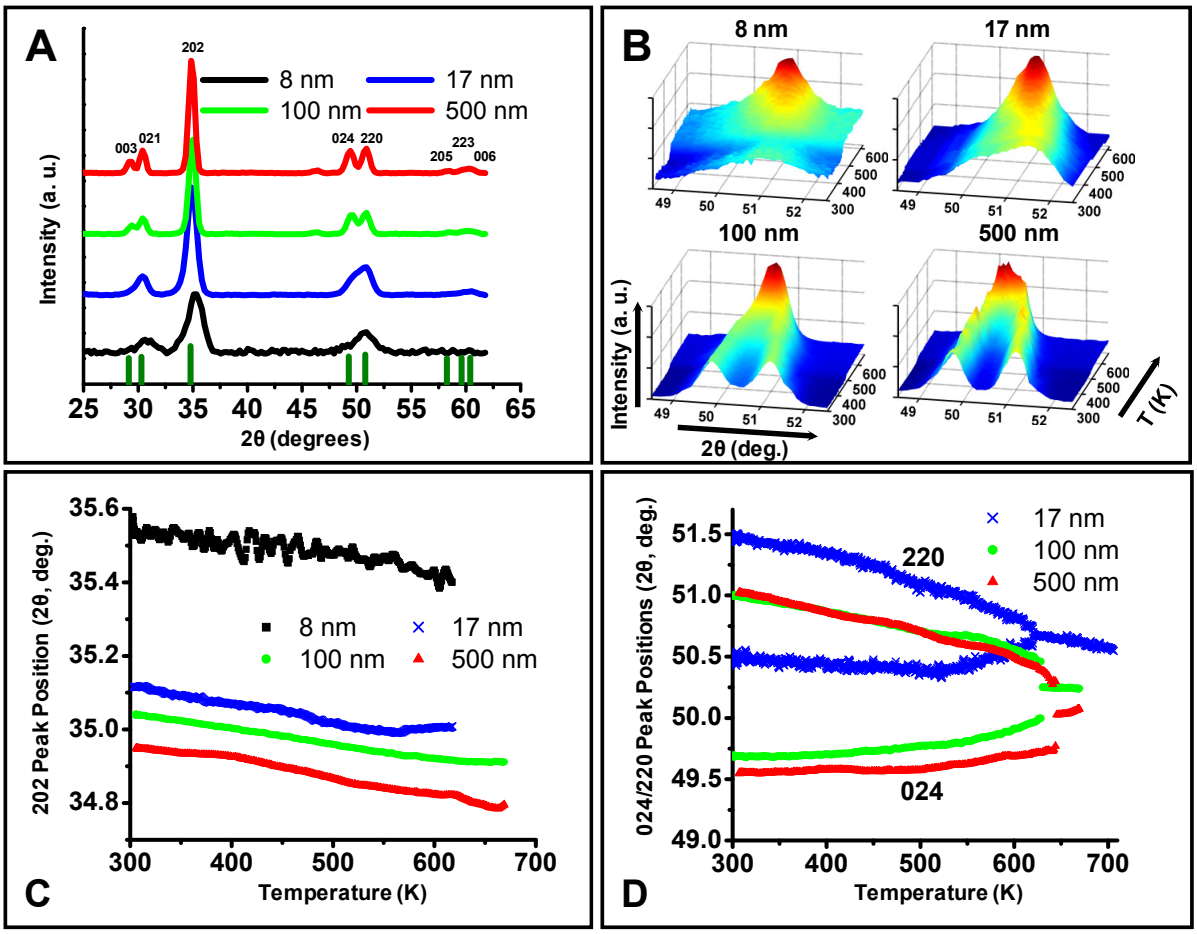

Figure 3.6. Temperature-dependent synchrotron x-ray diffraction studies of the polar phase transition in GeTe nanocrystals. (A) Room-temperature synchrotron powder x-ray diffraction patterns of GeTe nanocrystals; (B) plots of diffracted intensity versus 2-theta diffraction angle

and temperature for the 024/220 doublet. Convergence of the doublet peaks into a single peak of higher intensity characteristic of the cubic phase can be seen with increasing temperature; (C) position of the 202 (rhombohedral) diffraction peak as a function of temperature; (D) peak positions of the 024/220 (rhombohedral) doublet peaks as a function of temperature. The room-temperature peak splitting decreases for smaller particle sizes, and the doublet collapses as the rhombohedral to cubic phase transition is approached.

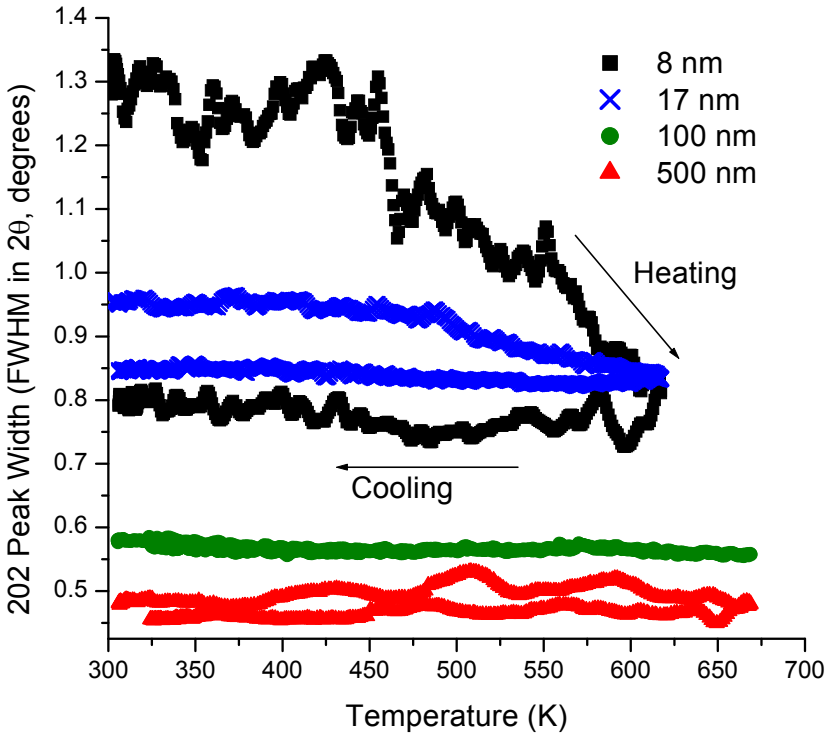

Figure 3.7. Sintering analysis of GeTe nanocrystals. The full width at half maximum of the 202 (rhombohedral) peak, which remains a singlet over the entire temperature range studied, is plotted as a function of temperature for both the heating and cooling stages of the experiment. Negligible changes in the width of the peak are evident for the 100 and 500 nm nanocrystals. A coarsening of the 17 nm nanocrystals of less than 10 percent and a coarsening of the 8 nm nanocrystals of approximately 40 percent can be observed.

3.3.4. Temperature-Dependent Raman Measurements:

Further evidence of the displacive character of the phase transition was obtained through temperature-resolved Raman studies. Many materials with a displacive polar phase transition possess a "soft" zone-center optical phonon that decreases rapidly in energy as the phase transition temperature is approached[60]. In GeTe, the polar distortion splits a single triply degenerate Raman-inactive F_{1u} symmetry optical mode in the cubic structure into an A_1 symmetry transverse optical mode (~125 cm^{-1} at 300 K) and a doubly degenerate E symmetry transverse optical/longitudinal optical mode (~90 cm^{-1} at 300 K), both of which are Raman-active[31]. The former (A_1) mode was determined to be the "soft" mode, and concurrent softening of the E symmetry mode was observed with increasing temperature. Since no Raman-active modes exist in the cubic-symmetry undistorted structure, the disappearance of these modes with increasing temperature and a pronounced decline in mode energies provide a spectroscopic signature of the phase transition.

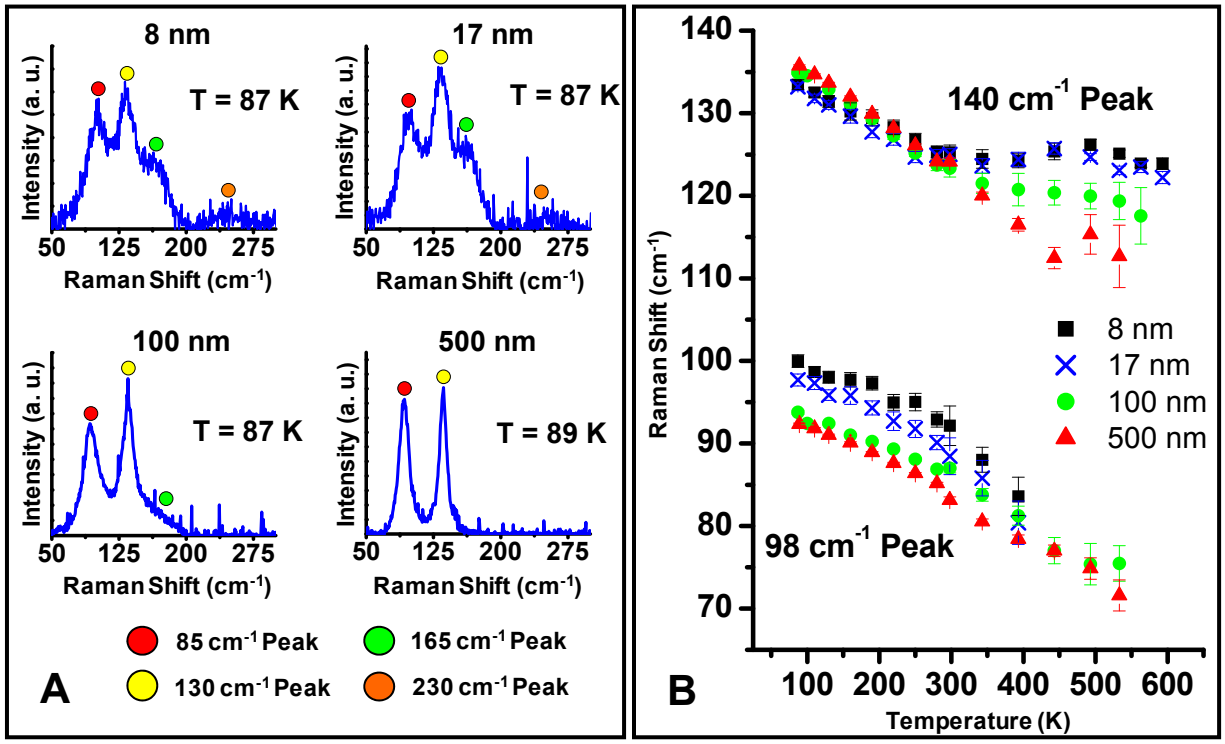

Figure 3.8. Temperature-dependent Raman scattering studies of GeTe nanocrystals. (A) Typical Raman spectra for films of 8 nm, 17 nm, 100 nm, and 500 nm GeTe nanocrystals at ~87 K. All spectra contain strong peaks that can be assigned primarily to the A_1 and E symmetry optical phonon modes of crystalline GeTe; (B) plot of the energies (in cm^{-1} units) of these two most prominent bands (primarily arising from the optical phonon modes of crystalline GeTe) as a function of temperature. Clear softening of both bands is observed for all particle sizes.

Raman analyses of nanocrystal films (Figure 3.8) demonstrate clear mode softening characteristic of a displacive phase transition. The two most prominent peaks near 85 and 130 cm^{-1} in the spectra are assigned primarily to the two optical phonon modes of crystalline GeTe. Additional peaks of lower intensity around 165 and 230 cm^{-1} were observed in the spectra of the 8, 17, and 100 nm nanocrystals. The additional modes can be assigned to a contribution from a low-coordination surface layer.

Raman characterization of a reference sample of amorphous GeTe nanoparticles (Figure 3.9) revealed four peaks around 85, 125, 165 and 230 cm^{-1}, similar to the peak positions observed in the spectra of the 8, 17, and 100 nm particles[39]. However, the band around 85 cm^{-1} is far more prominent for the crystalline samples, and the bands at 165 and 230 cm^{-1} become relatively weaker at progressively larger crystal sizes. The spectra of the nanocrystals can thus be understood as containing overlapping contributions from the crystalline interiors and low-

coordination surfaces. The temperature dependencies of the positions and intensities of the 85 and 130 cm^{-1} features support this interpretation. While these peaks shift only a few wavenumbers (cm^{-1}) between 82 K and 373 K for amorphous GeTe[29], in crystalline GeTe their rapidly vanishing intensities and redshifts of tens of wavenumbers provide further support for observation of the displacive phase transition[31]. For 100 nm and 500 nm nanocrystals, a rapid decline in the peak energies and the scattering intensities of the 85 and 130 cm^{-1} bands occurs with increasing temperature, indicative of the approaching phase transition. For the 8 and 17 nm nanocrystals, the 85 cm^{-1} band softens continuously from 87 K through 400 K; however, the position of the 130 cm^{-1} band is stable above ~350 K. This is ascribed to a rapid decline in scattering intensity of the crystalline A_1 phonon approaching the phase transition, so that the weakly temperature-dependent contribution from the surface dominates at higher temperatures. The smooth softening of the phonon mode energies mirrors the smooth changes in structural distortion determined by the diffraction measurements and indicates significant retention of the displacive character of the phase transition down to nanometer dimensions.

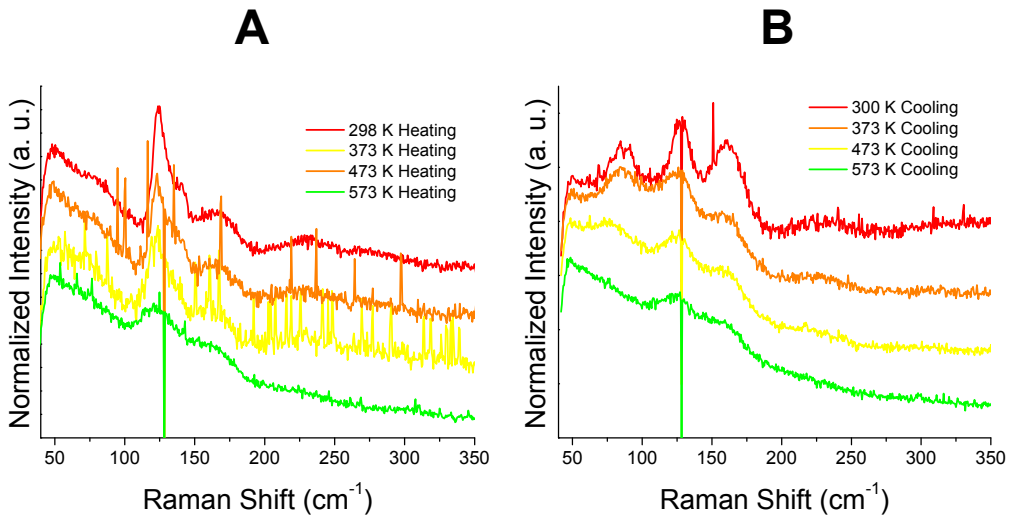

Figure 3.9. Raman spectra of a control sample of ~5 nm amorphous GeTe nanoparticles during a temperature ramp to 660 K. (A) Raman spectra taken during the heating stage of the temperature ramp; (B) Raman spectra taken during the cooling stage following the ramp to 660 K. The particles crystallized during the temperature ramp, leading to the appearance of the E symmetry crystalline phonon mode peak during the cooling stage of the experiment. Both the 165 and 230 cm^{-1} modes remain after the temperature ramp.

3.3.5. Discussion of Results:

The size effects observed throughout all experiments may be rationalized with a simple model based upon heightened surface-induced internal pressure. Several reports on nanosized perovskites implicate such internal strains in explaining reductions in the observed structural distortions and transition temperatures[16,54,61,62]. A spherical particle of radius *r* with surface energy γ experiences an internal stress given by $p = 2\gamma/r$ that may be on the order of 10^8-10^{10} Pa for common values of surface energy[16]. Internal strains arising from free surfaces have been found to induce a phase transition from a tetragonal phase to a disordered cubic phase in isolated $BaTiO_3$ nanoparticles[61] and to suppress ferroelectric ordering in $BaTiO_3$ wires[62]. Phenomenological modeling using Landau-Ginzburg-Devonshire theory by Morozovska, et al. further indicates sizeable shifts in bulk transition temperatures and suppression of ferroelectric ordering in spherical particles due to such surface stresses for positive values of the surface energy coefficient (i.e. compressive stress)[16]. This result is consistent with our diffraction results, which indicate both a lattice contraction for the smallest particles and a monotonic decrease in the angular distortion as a function of particle size. Literature reports describe similar trends in GeTe under hydrostatic pressures of between 0-10 GPa[59,63,64], and transition pressures as low as 3.5 GPa have been reported for GeTe compressed in a solid medium[63]. Using the bulk modulus of GeTe reported in the literature (K = 49.9 GPa) as a guideline, an estimated effective pressure of ~2.7 GPa can be calculated for the 8 nm particles[59]. These observations are also consistent with the Raman results, which indicate a ~25 % reduction in the energy splitting of the E and A_1 symmetry peaks at low temperatures. The convergence of these peaks towards the triply degenerate F_{1u} mode of the cubic phase provides further evidence of the partial suppression of the polar distortion in the smallest particles. The temperature-dependence of the structural parameters is also consistent with this interpretation. Due to the reduced room-temperature structural distortions, it is anticipated that the temperature required to transform nanocrystals to the cubic phase would be reduced relative to bulk material. These trends are clearly manifest in the temperature-dependence of the 024/220 doublet peak positions. While the gradual nature of the change in angular distortion and the broadened peaks prevent an unambiguous identification of the size-scaling law governing the transition temperature, the collapse of the doublet at lower temperatures for smaller particles supports this interpretation.

The pronounced stability of the polar state may arise from screening of the polarization due to the high bulk conductivity of GeTe. Bulk GeTe contains Ge vacancies that lead to a high (10^{20} cm^{-3}) concentration of free holes[23]. At this carrier concentration, several free carriers are expected to be present in each nanocrystal, even for particles with an average diameter of 5 nm. These free carriers may screen induced surface charges and thereby minimize the depolarizing field. The stability of the polar state may also be attributable to effective compensation of polarization-induced surface charges by organic capping ligands[65]. These mechanisms are not reflected in theoretical calculations demonstrating vortex polarization states in GeTe[10], which may explain the discrepancy with our experiments.

This chapter provides atomic-scale evidence of the room-temperature stability of the polar phase in colloidal nanocrystals down to at least 5 nm in size and suggests the persistence of linear order at nanometer length scales. Synchrotron x-ray diffraction and Raman spectroscopy studies demonstrate a reversible polar-nonpolar phase transition leading to a size-dependent polar distortion that is displacive in nature, which has been directly confirmed with aberration-corrected transmission electron microscopy. This work reveals the surprising stability of polar distortions in freestanding nanometer-sized crystals and provides a platform for developing future fundamental studies of the nature of polar ordering at atomic length scales.

Chapter 4: Characterization of Ferroelectric Ordering in Individual Colloidal Nanocrystals

Reproduced in part with permission from: Mark J. Polking, Myung-Geun Han, Amin Yourdkhani, Valeri Petkov, Christian F. Kisielowski, Steve Volkov, Yimei Zhu, Gabriel Caruntu, A. Paul Alivisatos, and Ramamoorthy Ramesh, "Coherent Ferroelectric Ordering in Individual Nanoscale Single Crystals" [in preparation] **2011**.

4.1 Introduction:

New synthetic strategies for nanostructures of functional materials and new nanoscale characterization tools have rapidly expanded knowledge of fundamental physical properties at finite dimensions. While much progress has been made in the understanding of nanoscale photophysical[66,67], magnetic[18,68], and many other functional properties, understanding of the basic physics of ferroelectric nanomaterials remains far less advanced. Conclusive answers to the questions of the fundamental nature of the polar state at finite dimensions and the mechanisms for ferroelectric size effects have been hindered in part by reliance on ensemble-averaged measurement techniques, which obscure the local behavior of individual crystals.

The work described in this chapter aims to remedy these shortcomings through analysis of ferroelectric ordering at a local, unit-cell scale. In this chapter, detailed imaging of local structure is achieved using atomic-resolution aberration-corrected transmission electron microscopy and nanometer-resolution mapping of ferroelectric polarization with off-axis electron holography. Ferroelectric ordering arises from a spontaneous distortion of the crystal lattice, leading to relative displacements of the ionic sublattices in the unit cell[1]. Direct, atomic-resolution imaging of these displacements, generally on the order of 0.1 Å, provides a powerful means of analyzing local polarization patterns[69,70]. Coordinating this analysis with direct imaging of the corresponding electrostatic potential gradients through holographic imaging of the resulting phase shifts[71] enables both the structural and electrostatic manifestations of the polar state to be uncovered in individual nanoscale crystals at a local scale, recovering crucial details obscured by ensemble-averaged measurement techniques. Combining this local-scale imaging of ferroelectric ordering with direct electrical measurements of individual nanocrystals then enables the defining characteristic of a ferroelectric, namely the reorientation of the spontaneous polarization under an applied electric field, to be directly examined and provides a complete, nanoscale picture of the ferroelectric behavior of nanometer-scale single crystals.

In this chapter, the ferroelectric properties of individual nanocrystals of semiconducting GeTe and the archetypal oxide ferroelectric $BaTiO_3$ prepared using colloidal chemistry methods are probed. Aberration-corrected transmission electron microscopy (TEM) is employed to map

local ferroelectric cation displacements at the unit-cell scale in both materials with picometer-level precision. These detailed TEM studies are complimented with off-axis electron holography studies of individual $BaTiO_3$ nanocubes, which enable the direct imaging of the ferroelectric polarization. These experiments indicate that a monodomain ferroelectric state with an overall, linear polarization is readily stabilized in these nanocrystals, albeit with evidence of polarization rotation. In addition, piezoresponse force microscope (PFM) measurements of individual $BaTiO_3$ nanocrystals demonstrate polarization switching of sub-10 nm nanocubes and reveal superparaelectric behavior at room temperature below a critical size of 5-10 nm, indicating the ultimate limit for the size-scaling of the polar phase.

As described in Chapter 3, germanium telluride is the simplest material to undergo a ferroelectric phase transition, with one anion and one cation per primitive unit cell[31,72]. This polar distortion in GeTe, manifested by a relative displacement of the Ge and Te sublattices along a [111] direction (Figure 4.1A, top)[32,33], can be readily imaged in a [110]-type projection (Figure 4.1A, bottom). GeTe exists naturally in a nonstoichiometric phase with a high density of Ge vacancies, leading to a density of free holes exceeding 10^{20} per cubic centimeter[23,73]. Although this high carrier density has inhibited practical ferroelectric switching, GeTe presents an interesting test case of a ferroelectric metal with strong internal polarization screening. The classic perovskite ferroelectric $BaTiO_3$, in contrast, is an insulating oxide with a Curie temperature of around 400 K[74]. Below this temperature, the cubic prototype phase undergoes a tetragonal distortion along a [001]-type axis with a corresponding displacement of the central Ti cation along the same direction (Figure 4.1B, top), producing a spontaneous polarization[74]. This distortion can be observed in [100]-type projections (Figure 4.1B, bottom).

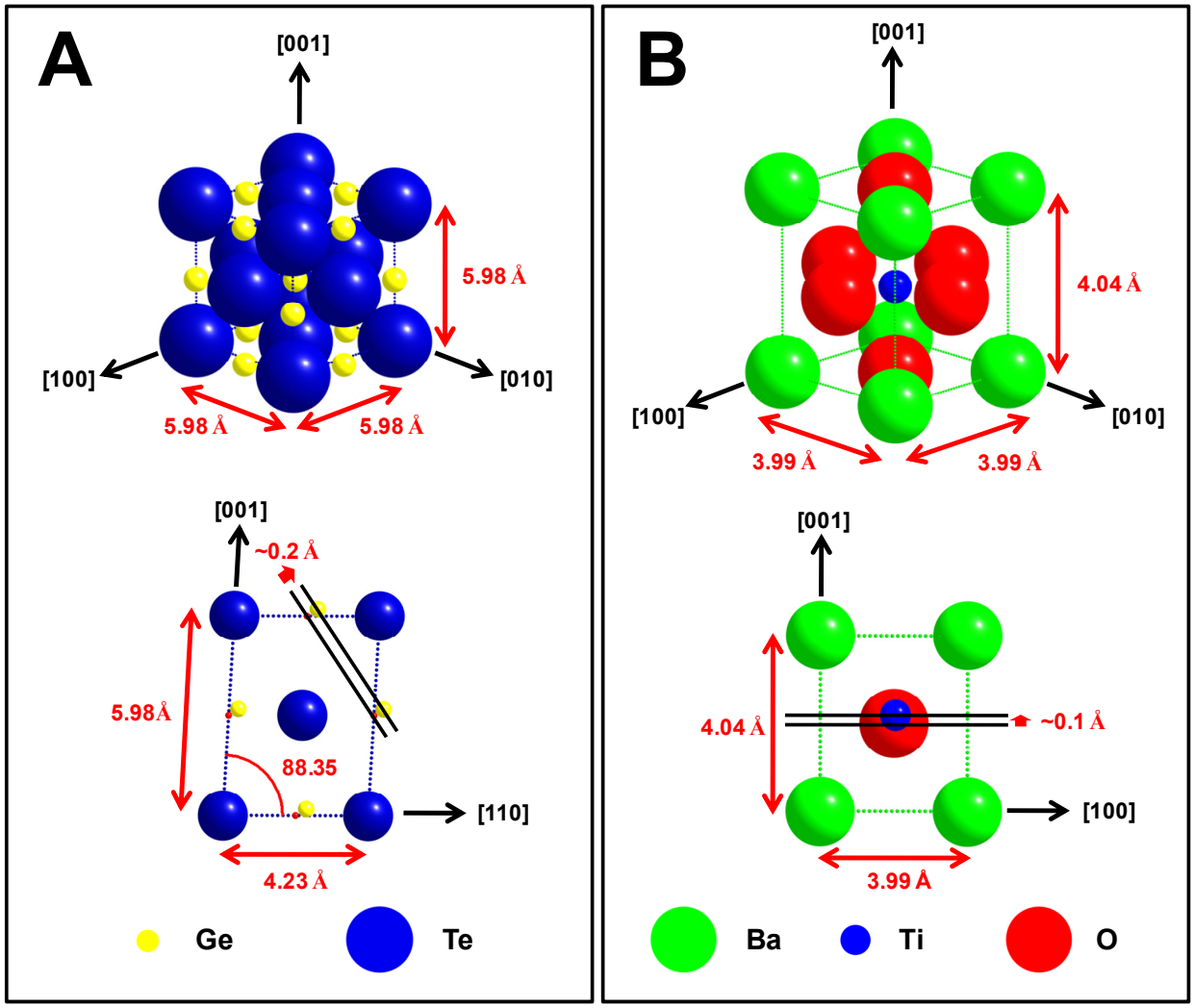

Figure 4.1. Ferroelectric distortions of the GeTe and $BaTiO_3$ conventional unit cells. (A) Conventional unit cell of GeTe in the rhombohedral phase; a [110]-type projection used for atomic-resolution transmission electron microscopy (TEM) is shown. The rhombohedral distortion of the unit cell results in an angular distortion of the principal axes accompanied by a relative displacement of the Ge sublattice with respect to the Te sublattice (small red arrows); (B) conventional unit cell of tetragonal $BaTiO_3$; a [100]-type projection used for atomic-resolution TEM imaging is shown. The ferroelectric phase transition results in a tetragonal distortion of the unit cell along a [001]-type axis and a displacement of the titanium cation from the center of the unit cell, removing the inversion symmetry. Structural data are taken from references 30 and 74.

4.2 Materials and Methods:

Nanocrystal Synthesis:

Monocrystalline nanoparticles of both materials were prepared using colloidal synthetic techniques. GeTe nanocrystals with an average diameter of 8 nm were prepared through reaction of Ge(II) bis-bis(trimethylsilyl)amide and trioctylphosphine-tellurium in the presence of a 1-dodecanethiol surfactant as described in Section 1.2 (Figure 4.2A). Nanocrystals of $BaTiO_3$ were prepared using a two-phase aqueous/organic synthesis procedure in a pressure vessel following a previous literature report (Figure 4.2B)[12]. Nanocubes with average side lengths of 8, 10, and 15 nm were prepared using this procedure, and quasi-spherical particles with an average diameter of 10 nm were prepared by decreasing the polarity of the reaction medium through addition of a supplementary volume of decanol in the mixture formed by water, ethanol and decanol, respectively[75].

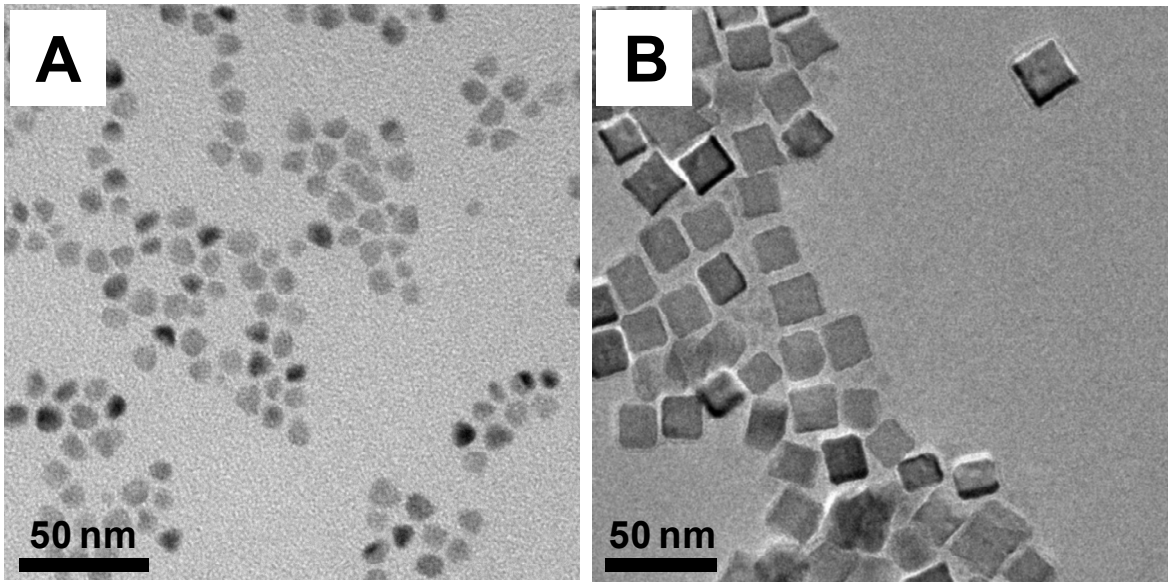

Figure 4.2. Transmission electron microscope (TEM) images of GeTe and $BaTiO_3$ nanocrystals. (A) TEM image of 8 nm average diameter GeTe nanocrystals; (B) TEM image of 15 nm average size $BaTiO_3$ nanocubes.

Atomic-Resolution Transmission Electron Microscopy:

Nanocrystals of GeTe with an average diameter of 8 nm and nanocubes of $BaTiO_3$ with an average size of 10 nm were imaged under negative phase contrast conditions using the aberration-corrected TEAM 1 microscope at the National Center for Electron Microscopy, a modified FEI Titan 80-300 equipped with a combined spherical and chromatic aberration corrector, a special high-brightness field emission gun, and a Gatan Image Filter (GIF). Through-focus series consisting of 30 high-resolution TEM (HRTEM) images of GeTe nanocrystals in [110]-type orientations and $BaTiO_3$ nanocrystals in [100]-type orientations were taken at defocus values ranging from 300 Å to -300 Å with a negative coefficient of spherical aberration of approximately -15 μm. These focal series were reconstructed using the Gerchberg-Saxton algorithm implemented in MacTempas X by Total Resolution, Inc. to recover the phase of the electron wave function at the exit plane of the specimen, which contains directly interpretable information about the atomic structure down to the information limit of the microscope[76,77]. The resulting phase images were Fourier filtered using the background subtraction filter in MacTempas X; this filtering did not alter the observed polarization patterns. Unit cell-scale maps of the local ferroelectric polarization were extracted from the reconstructed phase images using Gaussian fitting of atomic column positions followed by calculation of the relative displacements of these columns for each unit cell (Figure 4.3). To avoid potential artifacts due to crystal tilt, only complex exit waves exhibiting highly symmetric Fourier transforms were employed in the analysis. $BaTiO_3$ images were acquired at an accelerating voltage of 300 kV, and GeTe images were acquired at 80 kV. All samples were imaged on ultrathin carbon grids from Ted Pella. Simulated phase images for GeTe and $BaTiO_3$ nanocrystals were calculated as described in Section 3.2.

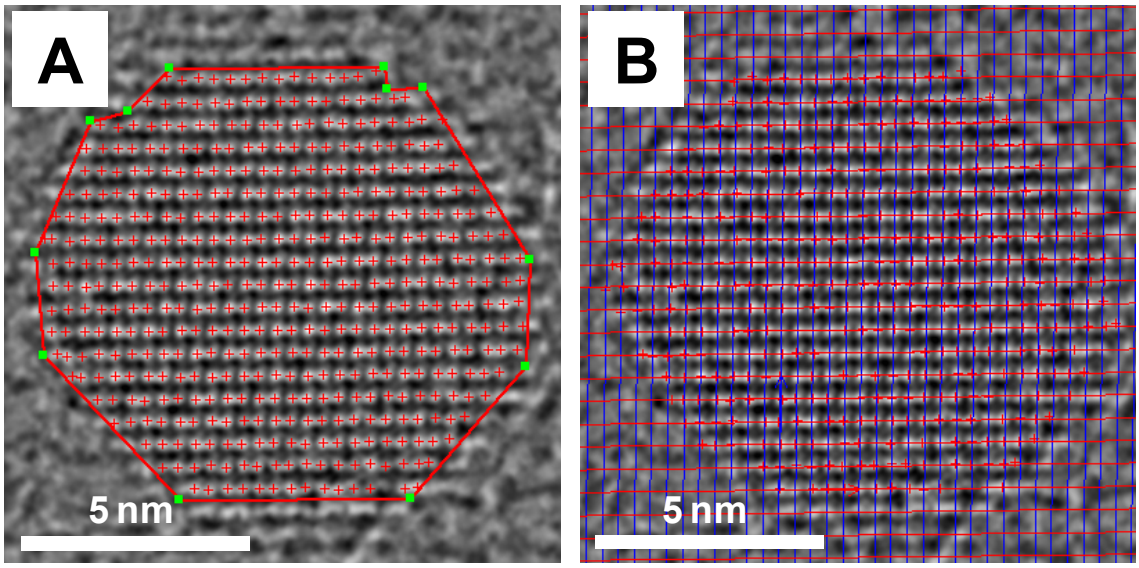

Figure 4.3. Quantitative analysis of atomic-resolution reconstructed phase images. (A) Reconstructed phase image of a GeTe nanocrystal displaying peak positions determined by the Gaussian peak fitting function in MacTempas X (Total Resolution, Inc.); (B) reconstructed phase image with the best-fit lattice calculated using a least-squares routine.

Off-Axis Electron Holographic Imaging of $BaTiO_3$ Nanocubes:

Holographic images of individual $BaTiO_3$ nanocubes were acquired using a JEOL 3000F transmission electron microscope operated at 300 kV equipped with a field emission gun, GIF, Lorentz lens, and biprism. Holograms were acquired with a biprism voltage of 50 V, and reference images were taken over vacuum. Holograms were taken of particles suspended over vacuum on the edge of a lacey carbon grid. Phase images were reconstructed using custom Gatan Digital Micrograph scripts. Nanocubes were heated above the Curie point using a Gatan heating holder, and individual nanocubes were poled using a Nanofactory probe holder with an integrated tungsten STM tip. To enable access to particles on the carbon grid for the poling experiments, the copper/carbon grid was cut in half, leaving several copper grid squares exposed. The phase profiles presented in Figure 4.8 were calculated in Gatan Digital Micrograph using the line profile tool.

Simulated phase images for $BaTiO_3$ nanocubes were numerically calculated based on electrostatics. The spontaneous polarization charge (P_S) on one side of a $BaTiO_3$ nanocube was treated as a square sheet charge with uniform charge density P_S. For a square with a side length

of 2a with a uniform surface charge P_S, the center of which is the origin, the potential can be obtained by summing the contributions of elementary charges $P_S$dx′dz′:

$$V(x,y,z) = \frac{P_S}{4\pi\varepsilon_o}\int_{-a}^{a}\int_{-a}^{a}\frac{dx'dz'}{\sqrt{(x-x')^2+y^2+(z-z')^2}}$$
$$= \frac{P_S}{4\pi\varepsilon_o}\int_{-a}^{a}\ln\left[\frac{a+x+\sqrt{(x+a)+y^2+(z-z')^2}}{-a+x+\sqrt{(x-a)^2+y^2+(z-z')^2}}\right]dz'$$

The electron wave near the nanocube will be perturbed by the above potential field along the beam path (z-axis) and give rise to a phase image ($\Delta\varphi(x,y)$) according to the equation:

$$\Delta\varphi(x,y) = C_E\int_{-\infty}^{\infty}V(x,y,z)dz$$
$$= \frac{C_E P_S}{4\pi\varepsilon_o}\int_{-\infty}^{\infty}\int_{-a}^{a}\ln\left[\frac{a+x+\sqrt{(x+a)+y^2+(z-z')^2}}{-a+x+\sqrt{(x-a)^2+y^2+(z-z')^2}}\right]dz'dz$$

Here, C_E is an energy-related constant with a value of 6.526 mrad/V·nm for 300 keV electrons. The above double- integration problem was solved numerically using a Gatan Digital Micrograph script to generate the simulated phase images. In addition, to address the contact of the $BaTiO_3$ nanocube with the conducting carbon grid, a mirror square charge was set up to ensure zero potential on the carbon surface. This manipulation is equivalent to complete compensation of the spontaneous polarization charge on the side of the $BaTiO_3$ nanocube in contact with the carbon grid. Inside the $BaTiO_3$ nanocube, the mean-inner-potential experienced by incident electrons yields a constant phase shift.

Piezoresponse Force Measurements of Individual $BaTiO_3$ Nanocubes:

The polarization switching and local piezoelectric response of $BaTiO_3$ nanocrystals were studied at room temperature with an Asylum Research MFP-3D atomic force microscope working in contact mode. An AC240TM cantilever made of a tetrahedral silicon tip coated with platinum/titanium was used to apply a small AC voltage with an amplitude of 40 mV. Measurements were performed by applying two oscillating voltages with frequencies below and

above resonance (270 kHz), operating the cantilever in the dual AC resonance tracking (DART) mode[78]. The piezoresponse of the nanocubes was detected as the first-harmonic component of the deflection of the tip, $d=d_0+A\cos(\omega t+\varphi)$, where φ is the phase of the piezoelectric signal. The photodetector signal amplitude was demodulated with a lock-in amplifier and the values of the piezoelectric coefficient were obtained after calibrating the photodetector signal.

4.3 Results and Discussion:

4.3.1 Atomic-Resolution TEM Imaging of Individual GeTe Nanocrystals:

Atomic-resolution phase images of GeTe nanocrystals (Figure 4.4) provide information transfer beyond 0.7 Å and allow facile discrimination between Ge and Te atomic columns. The high atomic masses of the constituent elements enable the positions of these columns to be determined with an accuracy of a few picometers. Maps of local polar displacements obtained from these reconstructions (Figures 4.4B, 4.4D) indicate a primarily linear polarization state, albeit with evidence of complex rotational patterns in some particles. The polar displacement map illustrated in Figure 4.4B, similar to those extracted from the majority of reconstructions, illustrates local dipoles aligned in parallel along a [111]-type direction, consistent with a linear, monodomain polarization state, in agreement with the results of Chapters 2 and 3.

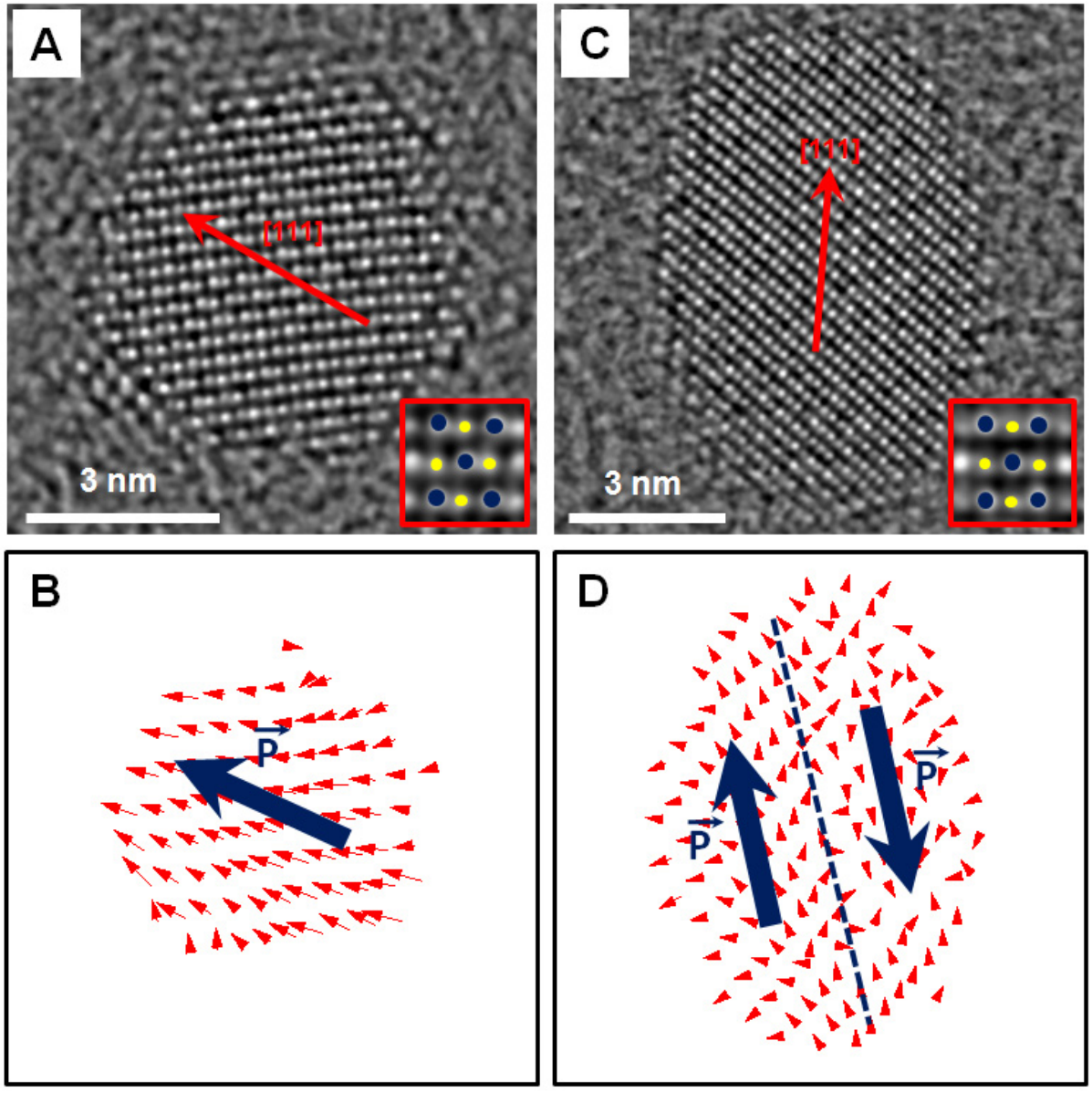

Figure 4.4. Atomic-resolution reconstructed phase images and polar displacement maps of individual GeTe monocrystalline nanoparticles. (A, B) Reconstructed phase image of a GeTe nanocrystal (A) and corresponding polar displacement map (B) illustrating a nearly linear, coherent polarization pattern along a [111] axis. Inset: magnified view of a GeTe unit cell from the particle demonstrating resolution of Ge and Te columns; (C, D) reconstructed phase image of a GeTe nanocrystal (C) and corresponding polar displacement map (D) illustrating an inversion domain boundary with flux closure in the center. Inset: magnified view of a GeTe unit cell from the particle demonstrating resolution of Ge and Te columns.

The displacements have an average value of approximately ~0.2 Å, consistent with but smaller than displacements reported for bulk material[30,32]. A portion of the polar displacement maps exhibit evidence of more complex, non-linear patterns. The polar displacement map of Figure 4.4D reveals a displacement pattern consistent with two antiparallel polarization domains separated by a (111) plane. The polarization points along opposite <111> directions on each side of the interface, consistent with an inversion domain boundary with rotational twinning[34]. In the central region of the particle, the displacements appear to rotate about the core, suggestive of toroidal polarization patterns predicted theoretically[9,10]. Multislice image simulations and subsequent phase reconstructions for GeTe particles with the same truncated cubic shape (Figure 4.5) indicate that crystal tilt is unlikely to be responsible for these patterns.

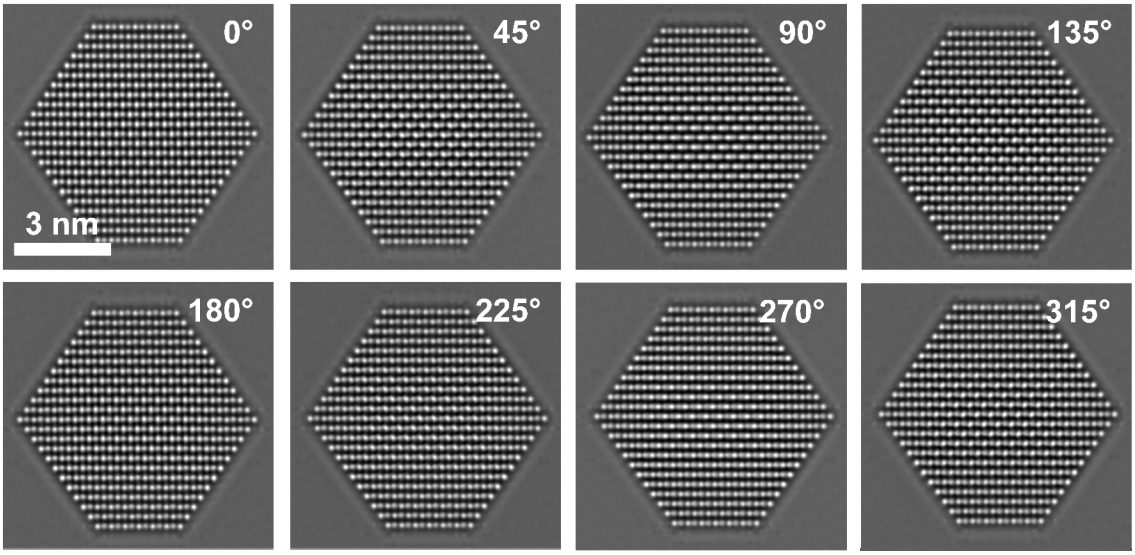

Figure 4.5. Simulated phase images for 8 nm GeTe nanocrystals. Simulations were performed for GeTe nanocrystals with a homogeneous linear polarization and a tilt angle of 10 mrad with respect to the beam direction at angles of 0-315° with respect to the vertical direction of the image plane.

4.3.2 Atomic-Resolution TEM Imaging of Individual $BaTiO_3$ Nanocubes:

Phase reconstructions for individual $BaTiO_3$ nanocubes (Figures 4.6A, 4.6C) provide an atomic-resolution picture of the local structure down to an information limit of around 0.7 Å, as for GeTe. All atomic columns, including low-contrast oxygen columns, can be readily distinguished in the images, allowing for precise extraction of the small local titanium

displacements that produce the spontaneous polarization. The corresponding polar displacement maps indicate a primarily linear, monodomain polarization state, as for GeTe, in contrast with theoretical expectations of a toroidal state[10]. The polar displacement map of Figure 4.6B illustrates clear alignment of the displacements for each unit cell along a [001]-type direction, consistent with a ferroelectric tetragonal structure with a coherent polarization. The average magnitude of the local Ti displacements (~0.1 Å) is near the bulk value (~0.09 Å)[74] and in agreement with previous reports indicating an enhancement of local Ti displacements in nanosized $BaTiO_3$[7,8].

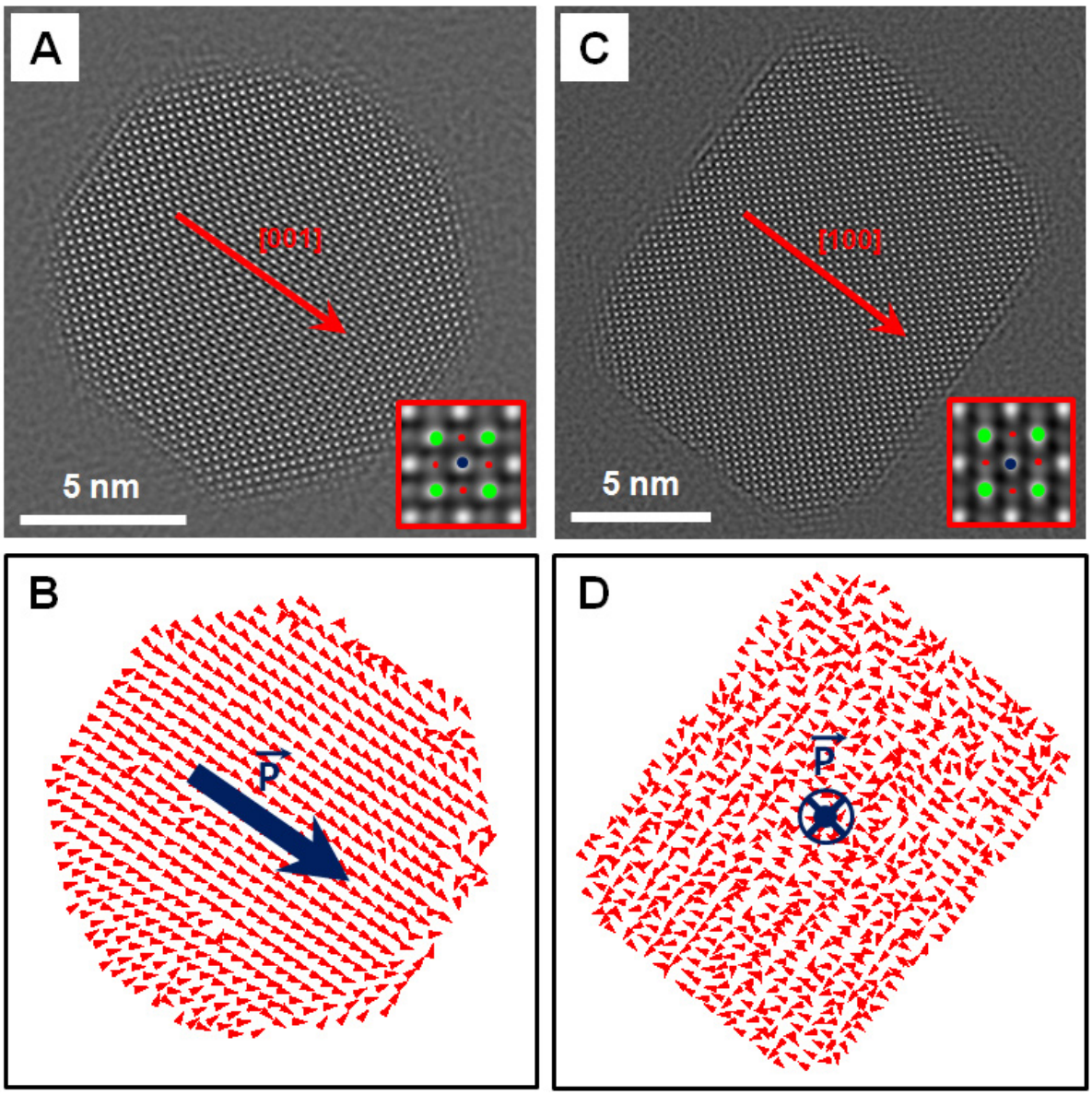

Figure 4.6. Atomic-resolution reconstructed phase images and polar displacement maps of individual $BaTiO_3$ monocrystalline nanocubes. (A, B) Reconstructed phase image of a $BaTiO_3$ nanocube (A) and corresponding polar displacement map (B) illustrating a nearly linear, coherent polarization pattern along the [001] axis. Inset: magnified view of a $BaTiO_3$ unit cell from the particle demonstrating resolution of Ba, Ti/O, and O columns; (C, D) reconstructed phase image of a $BaTiO_3$ nanocube (C) and corresponding polar displacement map (D) illustrating no clear polarization pattern with weak dipoles, suggesting an out-of-plane polarization orientation. Inset: magnified view of a $BaTiO_3$ unit cell from the particle demonstrating resolution of Ba, Ti/O, and O columns.

No clear pattern is observed in the displacements presented in Figure 4.6D, suggesting a polarization perpendicular to the image plane. The average magnitude of the displacements is greatly reduced from that of Figure 4.6B, further supporting this interpretation. Multislice image simulations for $BaTiO_3$ nanocubes with similar truncated cubic shapes (Figure 4.7) indicate a pronounced apparent displacement of the oxygen columns with respect to the Ti and Ba/O columns, even for small tilts (<10 mrad), providing a highly sensitive probe of crystal tilt, and a minimal relative shift of the Ti columns. The precise centering of the oxygen columns at the midpoints between the Ba/O columns in the experimental images demonstrates a minimal tilt of these crystals, suggesting that crystal tilt cannot be responsible for the observed polarization patterns.

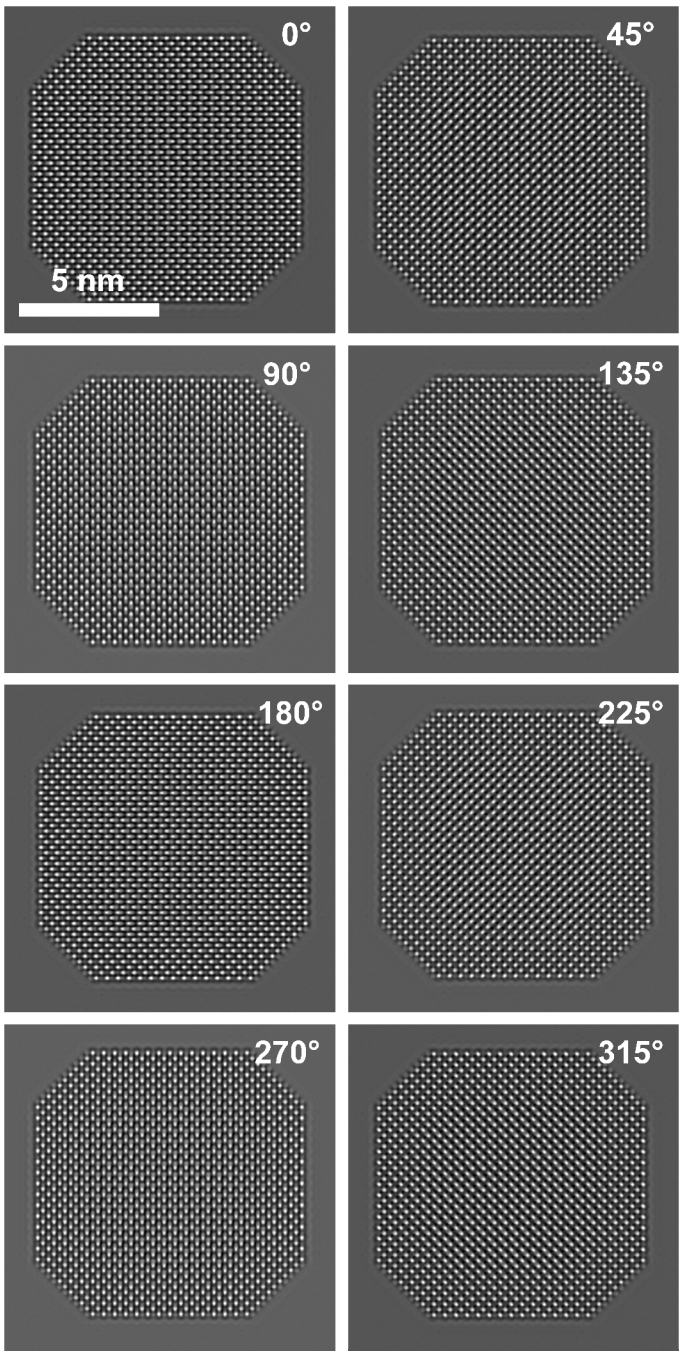

Figure 4.7. Simulated phase images for 10 nm $BaTiO_3$ nanocubes. Simulations were performed for $BaTiO_3$ nanocrystals with a homogeneous linear polarization and a tilt angle of 10 mrad with respect to the beam direction at angles of 0-315° with respect to the vertical direction of the

image plane. A shift of the oxygen columns with respect to the Ba/O and Ti columns can be observed, providing a sensitive indicator of crystal tilt.

4.3.3 Off-Axis Electron Holographic Imaging of Ferroelectric Polarization in $BaTiO_3$ Nanocubes:

Detailed *in-situ* studies of individual $BaTiO_3$ nanocubes with nanometer-resolution off-axis electron holography provide further evidence of the linear, monodomain polarization state and enable direct imaging of the spontaneous polarization. In off-axis holography, the electron beam from a field emission source is separated into two beams, one passing through the sample and the second passing through vacuum[79]. The overlap of these beams beneath the sample then produces an interference pattern from which the relative phase shift of the sample electron wave function can be reconstructed. Electric fields and ferroelectric polarization induce phase shifts of the sample beam with respect to the reference beam from which maps of the local electrostatic potential can be extracted[71].

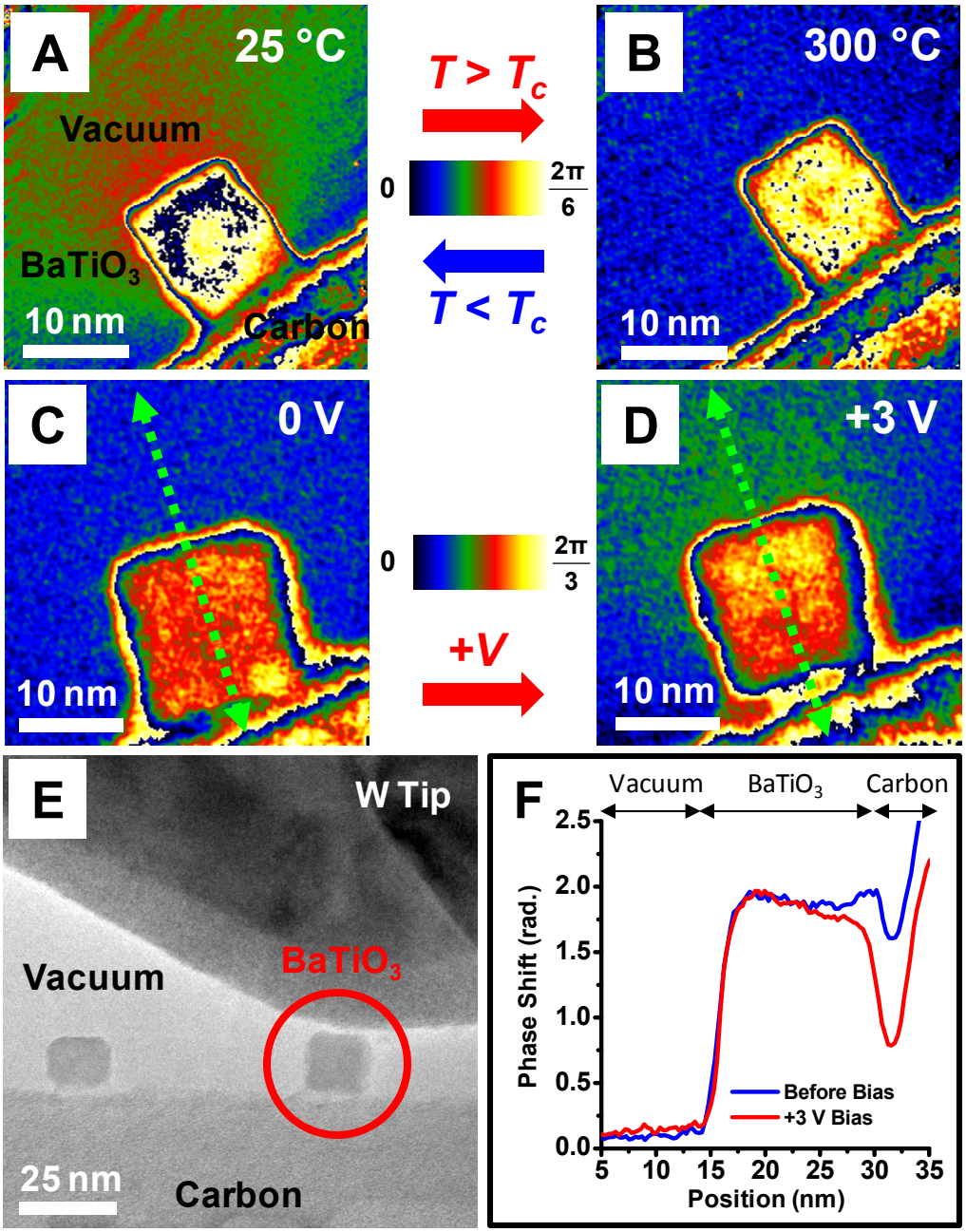

Figure 4.8. Direct polarization imaging of individual $BaTiO_3$ nanocubes with off-axis electron holography. (A, B) Phase images of an individual $BaTiO_3$ nanocube above (B) and below (A) the ferroelectric Curie temperature (130 °C) illustrating a fringing field emanating from the [001] face that disappears above T_c; (C, D) reconstructed phase images of an individual $BaTiO_3$ nanocube before application of an electrical bias (C) and after application of a +3 V bias (D). No fringing field can be observed before application of a bias; clear fringing fields emanating from

the [001] face can be observed after electrical poling; (E) TEM image of the integrated STM tip nearing contact with the individual $BaTiO_3$ cube imaged in panels C and D; (F) Corresponding line profiles for panels C and D demonstrating the appearance of a strong linear phase gradient upon electrical poling. All phase images have been amplified for clarity (6 times for A and B, 3 times for C and D).

Phase images of $BaTiO_3$ nanocubes suspended over vacuum exhibit a clear electrostatic fringing field emanating from a [001]-type face at room temperature (Figure 4.8A) characteristic of a linear polarization along this axis. Upon heating of the sample above the ferroelectric Curie temperature (130 °C), this field disappears (Figure 4.8B), reflecting the non-polar state. *In-situ* poling of individual particles with a scanning tunneling microscope (STM) tip (Figures 4.8C, 4.8D) results in the appearance of a strong, linear polarization along the [001]-type axis perpendicular to the carbon support. Prior to the application of a bias, the particle exhibits no clear electrostatic fringing field and a flat potential profile in the interior (Figure 4.8F), suggesting a polarization oriented perpendicular to the image plane. Upon application of a +3 V bias, a strong fringing field appears parallel to the axis of the STM tip, and a strong linear potential gradient can be observed in the particle interior, indicating a linear ferroelectric polarization along this axis. The observed phase images are in strong agreement with theoretical images (Figure 4.9) constructed using electrostatic calculations for a particle with a linear, monodomain ferroelectric polarization. The absence of a fringing field for the particle in Figure 4.8C prior to the application of bias discounts charging due to the electron beam as a source for the observed fringing field, and additional evidence is provided by the disappearance of the fringing field above the Curie temperature.

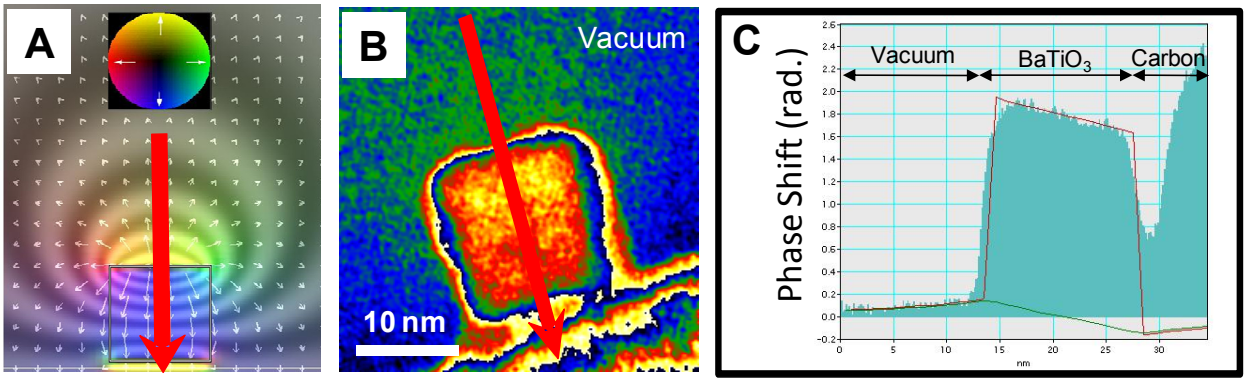

Figure 4.9. Comparison of experimental and simulated holographic phase images. (A) Theoretical phase image for a $BaTiO_3$ nanocrystal with a linear, monodomain polarization state (P_s = 25 μC/cm^2); (B) experimental phase image (3 times amplified) for a $BaTiO_3$ nanocrystal

poled at +3 V; (C) line profiles obtained for the regions indicated with arrows in A and B. The solid green line represents the calculated phase shift in the electron wave due only to the surface charge (P_s). The solid red line represents the calculated total phase shift due to the surface charge and the mean-inner-potential (17.9 eV) of the $BaTiO_3$ nanocube. Strong agreement between the experimental and theoretical images can be observed.

4.3.4 Piezoresponse Force Measurements of Individual $BaTiO_3$ Nanocubes:

Piezoresponse force microscopy studies provide further evidence for the persistence of a coherent ferroelectric polarization in these particles at room temperature and capture the ultimate stability limit of the ferroelectric state (Figures 4.10, 4.11). PFM, a scanned-probe technique that detects local piezoelectric deformations in response to an oscillating electric field[80], has been widely used for nanoscale mapping of ferroelectric domains[81] and local polarization switching[82]. Differences in polarization orientation can be discerned through differences in the phase of the material piezoresponse, with a 180° phase shift indicating two antiparallel polarization states[80]. Polarization switching experiments on individual 10 nm $BaTiO_3$ nanocubes (Figure 4.10A) illustrate the presence of a clear hysteresis and 180° phase switching at room temperature, indicating polarization switching between two antiparallel polarization states. While the value of the piezoelectric coefficient (d_{33} = 1.55 pm/V) is significantly reduced from the bulk value (d_{33} = 75 pm/V)[83], these results are comparable to those obtained for $BaTiO_3$ dots formed through ion milling with an edge length of 220 nm and a height of 40 nm (d_{33} = 2 pm/V)[84]. These measurements indicate that a stable ferroelectric state is clearly maintained at room temperature down to dimensions of 10 nm, in line with experimental work suggesting a preservation of the local dipole distortions in nanosized $BaTiO_3$[6,8].

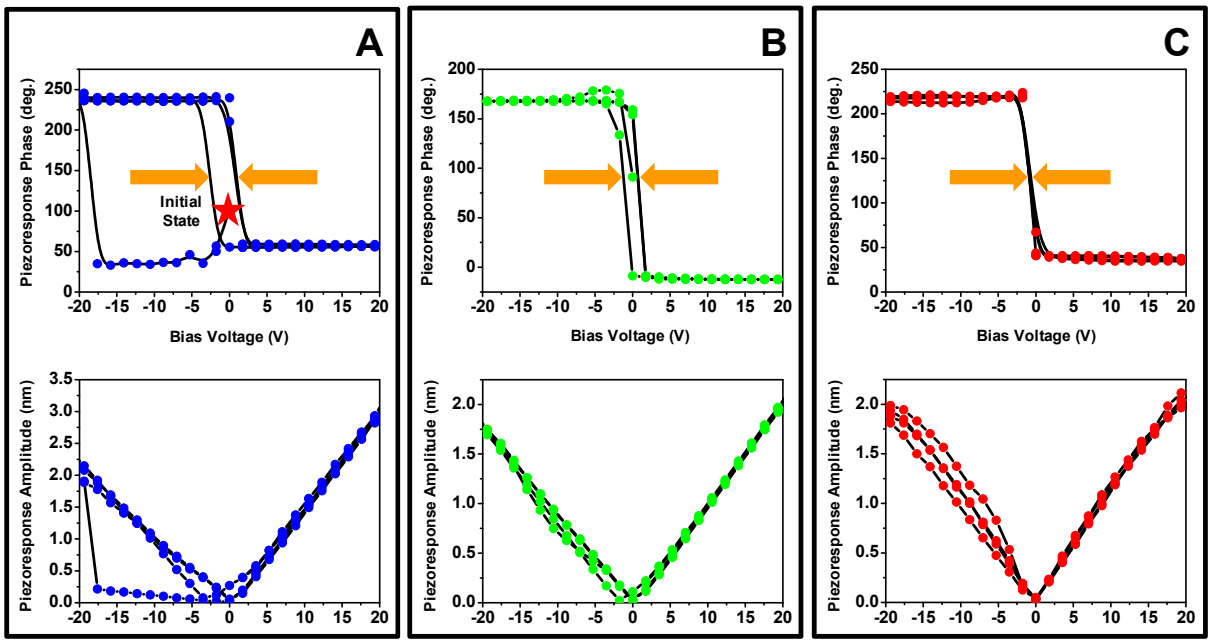

Figure 4.10. Temperature-dependent piezoresponse force microscope (PFM) measurements of individual 10 nm $BaTiO_3$ nanocubes. (A) Piezoresponse phase (top) and amplitude (bottom) for a single 10 nm $BaTiO_3$ nanocube at room temperature. A clear hysteresis and 180° phase switching can be observed; (B) piezoresponse phase (top) and amplitude (bottom) for the same 10 nm $BaTiO_3$ nanocube at 60 °C. A markedly decreased hysteresis is observed; (C) piezoresponse phase (top) and amplitude (bottom) for the same 10 nm $BaTiO_3$ nanocube at 80 °C. Although sharp 180° phase switching is maintained, the hysteresis collapses, indicating a transition to a superparaelectric state.

Temperature-dependent and size-dependent PFM measurements reveal the ultimate stability limit of the ferroelectric state. The hysteresis loop for 10 nm nanocubes shrinks at 60 °C (Figure 4.10B) and closes at approximately 80 °C (Figure 4.10C), but a highly non-linear curve with a 180° phase shift is maintained. PFM measurements of 5 nm nanocubes (Figure 4.11) demonstrate similar behavior down to room temperature, with no detectable hysteresis. The sharp transition between polarization states without hysteresis closely resembles the superparamagnetic state of small magnetic nanoparticles[85], in which aligned local spins undergo collective reorientation under ambient thermal energy, rather than the paraelectric state of $BaTiO_3$ above the Curie temperature, characterized by a gradual change in polarization with applied field[86]. Previous work[6-8] has suggested a transition to a paraelectric state, characterized by uncorrelated local dipoles, with decreasing particle size, leading to the disappearance of ferroelectric order. These results suggest, in contrast, that the polarization decays not due to the complete decoherence of local dipoles, but rather due to a transition to an analogous

superparaelectric state in which local dipoles maintain transient spatial coherence but rapidly undergo collective reorientation under ambient thermal excitation.

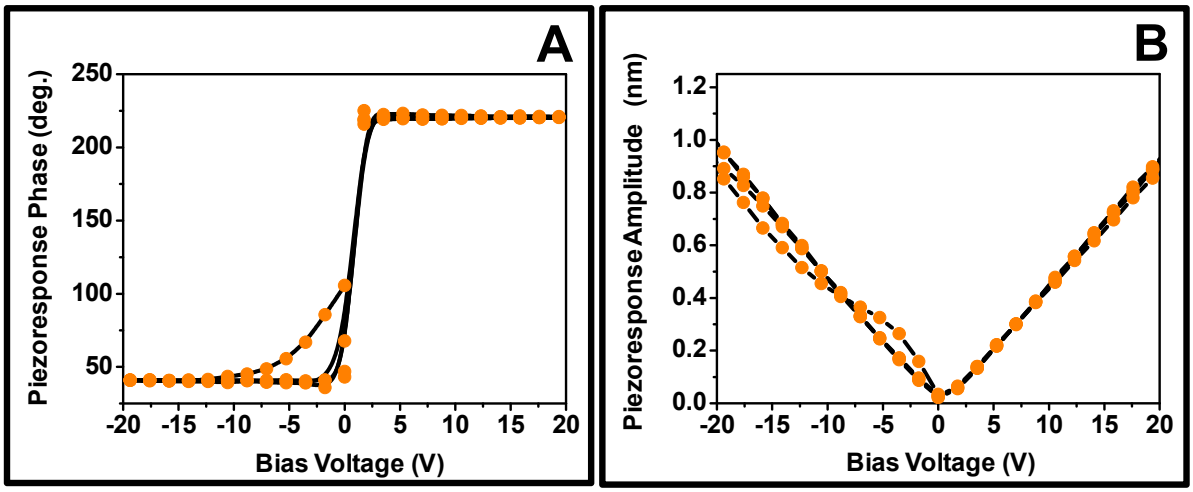

Figure 4.11. Temperature-dependent piezoresponse force microscope (PFM) measurements of individual 5 nm $BaTiO_3$ nanocubes. (A) Plot of piezoresponse phase vs. applied bias for an individual 5 nm $BaTiO_3$ nanocube at 25 °C; (B) corresponding plot of piezoresponse amplitude vs. applied bias for an individual 5 nm $BaTiO_3$ nanocube. No hysteresis is evident at room temperature, indicating the disappearance of a stable ferroelectric polarization.

4.3.5 Discussion of Results:

This work provides atomic-scale insight into the fundamental nature and stability of ferroelectric ordering down to its ultimate size limit. Atomic-resolution mapping of local ferroelectric distortions indicates a coherent, linear, and monodomain state accompanied by local structural distortions and some evidence of local polarization rotation. The persistence of ferroelectric coherence in $BaTiO_3$ is further supported by single-particle studies with off-axis electron holography and PFM measurements of individual nanocubes demonstrating ferroelectric switching behavior at room temperature. These PFM studies further demonstrate the ultimate stability limit of ferroelectric ordering, at which a transition to a superparaelectric state is observed. These experiments provide a glimpse of ferroelectric ordering down to its ultimate limits, revealing the nature of the polar state in individual particles down to atomic length scales.

Chapter 5: Comparing GeTe and $BaTiO_3$: Understanding the Mechanisms for Ferroelectric Size Effects

Reproduced in part with permission from: Mark J. Polking, Myung-Geun Han, Amin Yourdkhani, Valeri Petkov, Christian F. Kisielowski, Steve Volkov, Yimei Zhu, Gabriel Caruntu, A. Paul Alivisatos, and Ramamoorthy Ramesh, "Coherent Ferroelectric Ordering in Individual Nanoscale Single Crystals" [in preparation] **2011**. Figure 5.4 reproduced with permission from Prashant K. Jain.

5.1 Introduction:

The decay of ferroelectric ordering with decreasing crystal size is a phenomenon that has been known for decades, although only recently have its origins begun to be uncovered. Early ensemble studies of ferroelectric ceramics, primarily with x-ray scattering techniques, suggested a complete collapse of the ferroelectric state below a critical length scale of around 100 nm, temporarily dimming the prospects for nonvolatile memory devices and other applications demanding miniaturization of ferroelectric bits[4,5,54]. Debate raged, however, over whether the observed size effects were truly an intrinsic quality of a nanoscale ferroelectric or merely the consequence of extrinsic "dead layers" arising from surface damage due to poor processing conditions[40].

The advent of molecular beam epitaxy for the growth of ferroelectric thin films and the development of solution-phase routes to the preparation of high-quality freestanding single crystals[12-14] have enabled the study of nearly pristine nanoscale ferroelectrics, free from the mysterious "dead layers" that had previously plagued the field. Work on ferroelectric thin films with thicknesses of only a few atomic layers[87,88] demonstrated the persistence of ferroelectric ordering in two-dimensional systems far beyond the critical length scales reported in previous work. Work by Spanier and Urban on individual $BaTiO_3$ nanowires then extended this result to a one-dimensional system, further reviving hope for applications of nanoscale ferroelectrics[65].

These results fueled further debate about the fundamental origins of size effects in ferroelectric materials. Earlier work had suggested two fundamental mechanisms that lead to a reduction in ferroelectric polarization at finite dimensions, one involving the free surface and the second involving fundamental electrostatics. Seminal work by Kretschmer and Binder[15] developed the concept of an extrapolation length near the free surface, within which the polarization undergoes a linear decay as the surface is approached from within. The concept of a depolarizing field was then outlined in the work of Batra, Silverman, and Wurfel, which examined the effects of incomplete screening of polarization-induced surface charges. Incomplete electrical compensation at the surface, as found in this work, leads to an electric field

opposing the spontaneous polarization, known as the depolarizing field, which increasingly quenches the spontaneous polarization as film thickness is reduced[17]. Experimental confirmation of the former mechanism was provided by atomic-resolution TEM work by Jia, et al.[69], which clearly illustrated a linear decline in ferroelectric distortion near the surface of a lead zirconate-titanate thin film, and depolarization effects have been implicated as the cause of vortex polarization states predicted by theoretical calculations[9,24]. In previous studies, however, the two mechanisms have been examined separately, and the relative contributions of each mechanism to the changes in polar order at finite dimensions are not entirely clear.

Deconvolution of the effects of these two mechanisms requires systematic study of nanosized ferroelectrics with varying sizes, shapes, and electrostatic boundary conditions. Careful comparison of particles with similar compositions and sizes but variable morphologies enables elucidation of the influence of surface structure on ferroelectric order, and comparison of ferroelectric order between materials with different degrees of polarization screening helps to separate the influences of depolarization and surface effects. In the work described in this chapter, the former comparison is achieved using monocrystalline $BaTiO_3$ particles with both spherical and cubic morphologies and similar average sizes. The question of the relative influences of depolarization and surface effects is addressed using 8 nm particles of the highly conductive ferroelectric GeTe and 8 nm cubes of insulating $BaTiO_3$. These comparisons demonstrate the vital role of particle morphology on ferroelectric order and the dual influences of surface and depolarization effects on the coherence of the ferroelectric state.

The validity of the second comparison, however, depends on the highly conductive nature of GeTe at finite dimensions. GeTe, with an intrinsic bulk carrier density of 10^{20} cm^{-3}, is unlikely to be useful as a practical ferroelectric, but it may nonetheless prove useful as a test case of a ferroelectric metal with strong polarization screening. Evidence for the high density of free carriers in the nanocrystalline samples may be obtained from infrared absorbance measurements. Recent work on highly Cu-deficient Cu_2S samples has revealed strong, sharp localized surface plasmon resonance (LSPR) modes arising from the high density of free holes in this material, which exceeds 10^{20} per cubic centimeter[89]. The resonant wavelength of such a LSPR mode may be calculated using the following equation:

$$\omega_{sp} = \frac{1}{2\pi\sqrt{\frac{Ne^2}{\varepsilon_0 m_e(\varepsilon_\infty + 2\varepsilon_m)}}}$$

Here, N represents the carrier density, ε_0 the dielectric constant of the material, ε_m the dielectric constant of the surrounding medium, and m_e the effective mass of the carriers. Using literature values for the dielectric functions and effective mass[23,90], one can obtain an estimate of the carrier density of the semiconductor material. Analysis of GeTe nanocrystals with FTIR

absorption measurements and discrete dipole approximation (DDA) simulations demonstrates a well-defined localized surface plasmon resonance mode and a free carrier density exceeding 10^{20} cm^{-3}, comparable to bulk material.

5.2 Materials and Methods:

Synthesis of Amorphous and Crystalline GeTe Nanoparticles:

Crystalline GeTe nanoparticles with an average diameter of approximately 8 nm were prepared using the procedure presented in Section 1.2. Amorphous nanoparticles with the same average diameter were prepared using a modified version of this procedure in which a portion of the 1.5 mL of TOP-Te used in the crystalline synthesis was replaced with an equal volume of pure TOP. All other reaction parameters were the same as those for the synthesis of crystalline particles. Nanoparticle samples for subsequent experiments were cleaned using the procedure outlined in Section 1.2.

Fourier Transform Infrared Spectroscopy of GeTe Nanoparticles:

Absorbance measurements of GeTe nanoparticle films in both amorphous and crystalline forms were acquired using a Thermo Nicolet Nexus 870 Fourier transform infrared (FTIR) spectrometer. Data were acquired over a wavenumber range of ~500 cm^{-1} to 7500 cm^{-1} using a KBr beamsplitter and IR source. The absorbance of GeTe films dried from chloroform was analyzed in attenuated total reflectance (ATR) mode with averaging over 256 scans. Amorphous GeTe particles were crystallized by heating a film of nanoparticles on a silicon substrate under an argon atmosphere at 250 °C for 30-60 seconds.

Atomic Pair Distribution Function Analysis of $BaTiO_3$ and GeTe Nanocrystals:

Atomic pair distribution function measurements were carried out at beamline 11-ID-C at the Advanced Photon Source at Argonne National Laboratory using x-rays with an energy of 115.232 keV (λ = 0.1076 Å) and a large area detector. Samples were prepared by evaporation of a concentrated solution of nanocrystals into 1.5 mm quartz capillaries. Capillaries containing air-sensitive GeTe were sealed under argon using epoxy to prevent sample oxidation.

Commercial GeTe from Alfa Aesar was used as a standard for comparison with the nanocrystalline powders. Several scans were taken and averaged to improve the x-ray diffraction (XRD) data statistics. The XRD data were reduced to atomic pair distribution functions (PDF, G(r)) using the program RAD[91]. The atomic PDFs were fit with structure models featuring long-range ordered dipoles and no dipoles. The fits were completed with the help of the program PDFgui[92].

5.3 Results and Discussion:

5.3.1 Amorphous and Crystalline GeTe Nanoparticles:

Samples of both amorphous and crystalline GeTe nanoparticles with an average size of around 8 nm were synthesized by varying the ratio between trioctylphosphine-Te (TOP-Te) and the germanium(II) amide precursor with a constant concentration of TOP in the reaction flask. A large excess of TOP-Te yielded crystalline particles, as determined by powder x-ray diffraction, TEM, and electron diffraction measurements, whereas more stoichiometric mixtures of the precursors yielded amorphous particles, as determined by the same series of measurements. Further reduction in the concentration of TOP-Te yielded highly Ge-rich amorphous particles, as confirmed by energy dispersive x-ray analysis (EDAX). A typical TEM image and electron diffraction pattern for the amorphous particles are shown in Figure 5.1.

While the cause of the transition between amorphous and crystalline states is not entirely clear, a systematic increase in crystallization temperature of the amorphous particles was observed with decreasing Te content. Samples prepared with a nearly stoichiometric mixture of Ge and Te precursors crystallized readily under the heat treatment described in Section 5.2 (250 °C for 30-60 seconds). The Ge-rich samples, in contrast, remained amorphous following the same heat treatment. It is thus possible that crystallization of samples with lower Te content is inhibited at the injection temperature (230 °C), and certainly at the growth temperature (220 °C), leading to crystalline particles at higher Te levels. This result is consistent with thin film measurements by Raoux, et al.[93].

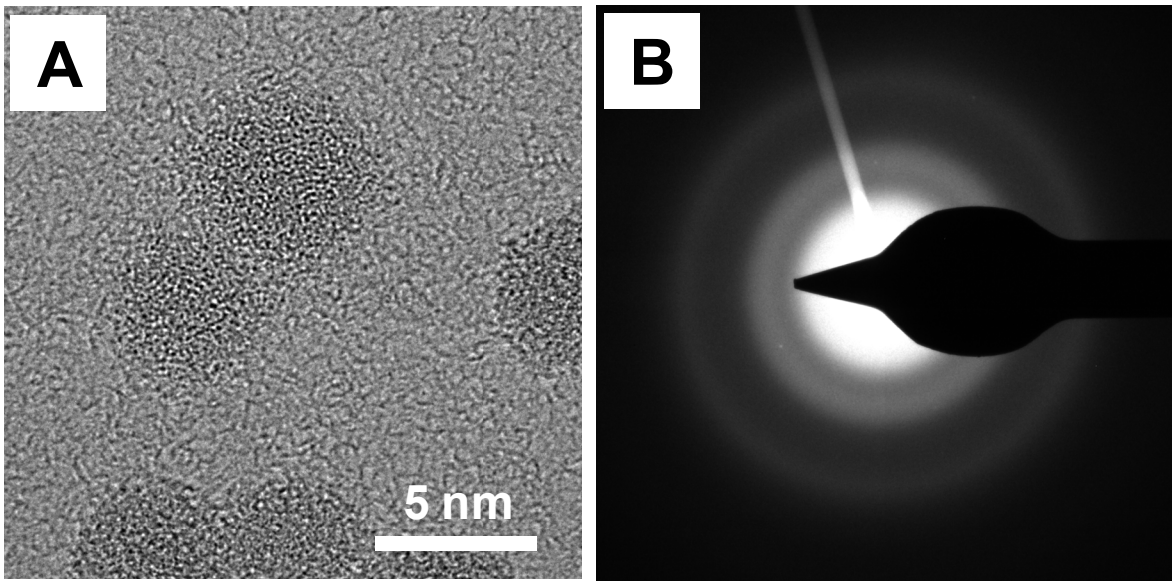

Figure 5.1. Amorphous GeTe nanoparticles. (A) TEM image of 8 nm amorphous GeTe nanoparticles. No lattice fringes are evident; (B) electron diffraction pattern of 8 nm amorphous GeTe nanoparticles. Only broad features can be observed, consistent with an amorphous phase.

5.3.2 Fourier Transform Infrared Spectroscopy of GeTe Nanoparticles:

Fourier transform infrared spectroscopy (FTIR) measurements of both amorphous and crystalline GeTe nanoparticles demonstrate a clear localized surface plasmon resonance in the crystalline phase that is absent in the amorphous phase. FTIR measurements of amorphous particles (Figure 5.2A) show a gradual increase in absorbance with increasing energy with sharp absorption lines assigned to 1-dodecanethiol surfactant molecules[94] near 3300 cm^{-1} (0.37 eV). The absorption spectrum of the crystalline particles (Figure 5.2B), in contrast, exhibits the same spectral features due to 1-dodecanethiol ligands and a band gap absorption onset at higher energies seen in the amorphous samples, but includes an additional broad, approximately Gaussian absorption feature centered around ~0.5 eV with a line width of ~0.3 eV. This absorption feature closely resembles the plasmon mode observed previously in highly doped (> 10^{21} cm^{-3}) Cu_2S samples and is in strong agreement with the position of the free carrier absorption onset observed in thin film samples[57,95].

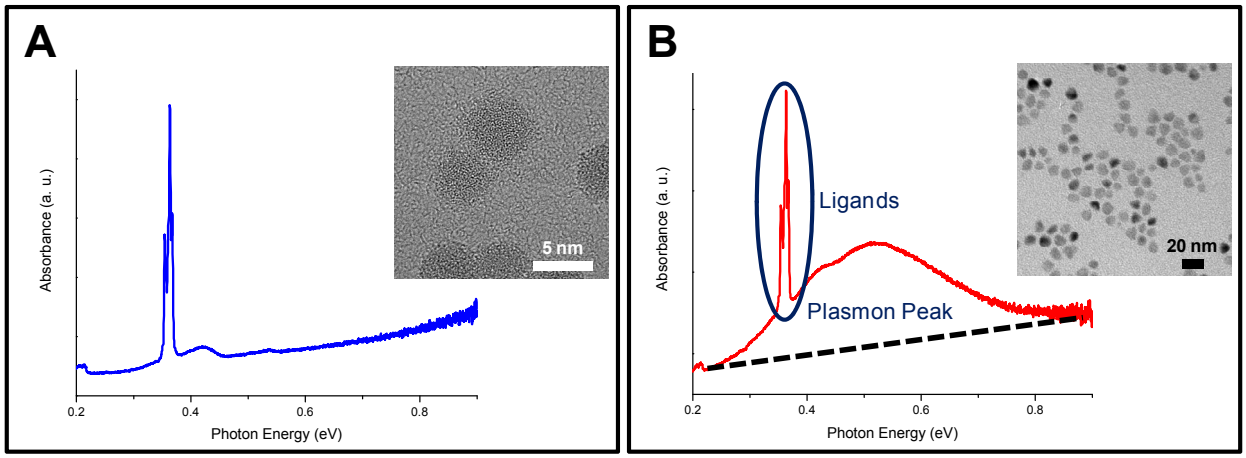

Figure 5.2. Fourier transform infrared spectroscopy (FTIR) absorption measurements of amorphous and crystalline GeTe nanoparticles. (A) FTIR absorption spectrum of 8 nm amorphous GeTe nanoparticles. A gradual increase in absorption due to excitation across the band gap can be observed along with sharp features attributed to 1-dodecanethiol ligands; (B) FTIR absorption spectrum of 8 nm crystalline GeTe nanoparticles. An additional broad, nearly Gaussian feature centered around 0.5 eV can be observed; this feature is assigned to a localized surface plasmon resonance mode.

FTIR measurements on the same sample of GeTe particles taken before and after crystallization (Figure 5.3) demonstrate the appearance of this broad mode after crystallization, excluding differences in surface coverage as a source of this feature. In addition, low-temperature absorption spectra reveal no significant shifts or variations in the intensity of this peak, indicating that excitonic absorption is unlikely to be responsible for this feature. Further support for this argument can be obtained from discrete dipole approximation (DDA) simulations of the absorption spectra for both material phases (Figure 5.4). The simulated absorption spectrum of the crystalline material including the Drude contribution due to free carriers shows a clear absorption peak around 0.3 eV with a line width similar to that for the plasmon feature observed in experiments. This feature disappears when the Drude contribution to the dielectric function is ignored, indicating that this feature is indeed plasmonic in nature. The discrepancy in peak position may be attributable to a difference in free carrier density between the simulations (5×10^{20} cm^{-3}) and the actual particles. Comparison between simulation and experiment thus suggests a carrier density on the order of $10^{20} - 10^{21}$ cm^{-3}, well within the regime of metallic behavior.

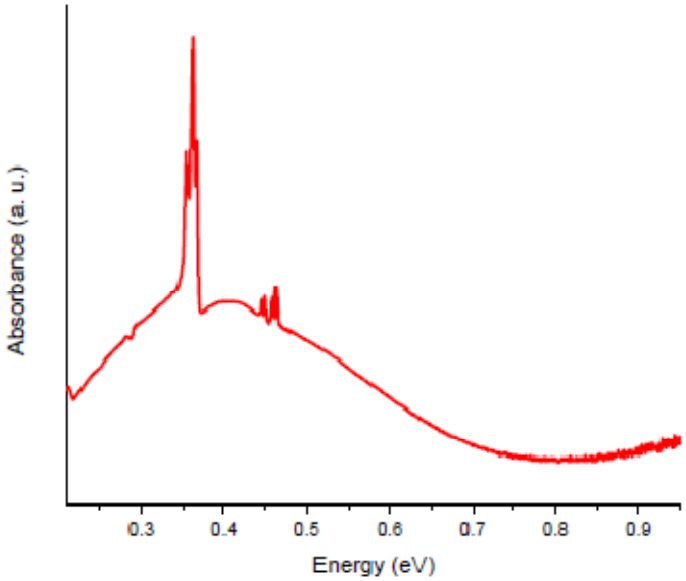

Figure 5.3. FTIR absorption spectrum of crystallized amorphous GeTe nanoparticles. The plasmonic absorption feature centered around ~0.5 eV reappears upon crystallization, indicating that differences in surface coverage or organic contamination are not responsible for this peak.

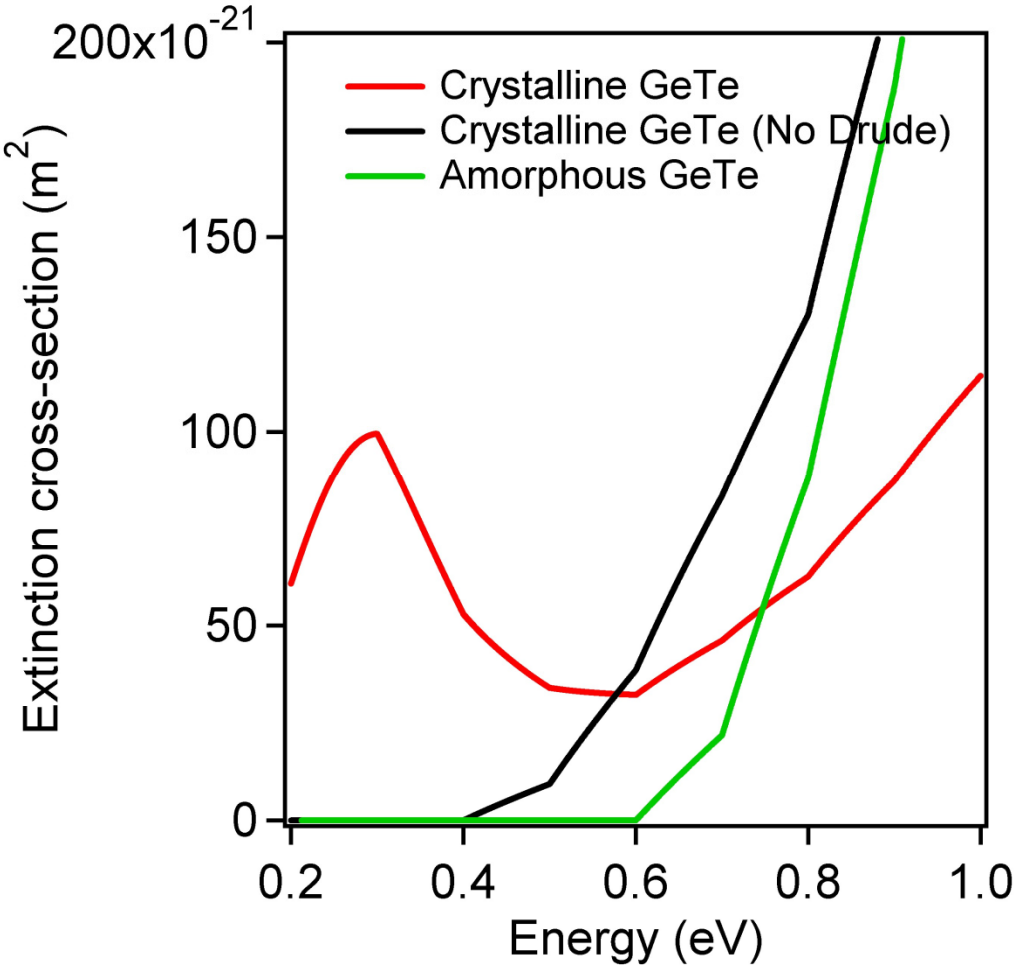

Figure 5.4. Simulated absorption spectra for amorphous GeTe nanoparticles and for GeTe nanocrystals with and without the Drude contribution to the dielectric functions. The simulated spectra, obtained from discrete dipole approximation methods, demonstrate the appearance of a well-defined absorption band similar to the plasmon feature observed in experiments in the crystalline material when the Drude (free carrier) contribution is considered. This feature disappears when the Drude contribution is ignored, indicating that this feature arises from free carrier (i.e. plasmonic) absorption.

5.3.3 Atomic Pair Distribution Function Measurements of GeTe Nanocrystals:

Atomic PDFs were calculated from synchrotron diffraction patterns for 8 nm GeTe nanocrystals. Comparison between atomic PDFs of GeTe (Figure 5.5) with both cubic and rhombohedral structural models yields a superior fit to the rhombohedral model, indicating the presence of local rhombohedral distortions. The best fit is obtained for a lattice constant of 5.891 Å and a rhombohedral angle of 88.25°, in good agreement with the Rietveld results for 8 nm GeTe nanocrystals presented in Chapter 3. In addition, the PDF analysis allows the magnitude of the polar sublattice displacement to be extracted, yielding a value of x = 0.240 (compared with 0.250 for the undistorted structure) for the position of the Ge cation. This corresponds to a sublattice displacement of approximately ~0.1 Å, considerably reduced from the magnitudes of the displacements observed in atomic-resolution TEM studies, approximately 0.2 Å. This suggests a partial disordering of the ferroelectric distortions across the particles.

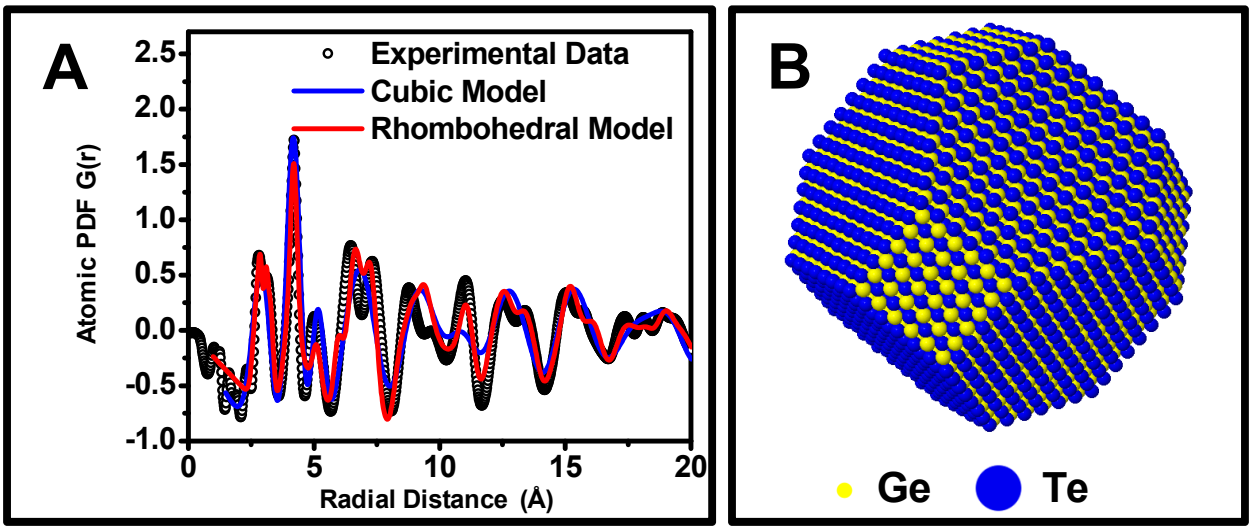

Figure 5.5. Atomic pair distribution function analysis of GeTe nanocrystal ensembles. (A) Atomic pair distribution function (PDF) for 8 nm GeTe nanocrystals compared with cubic and rhombohedral structural models; (B) model structure for 8 nm GeTe nanocrystals.

Insight into the length scale over which these rhombohedral distortions remain spatially correlated can be obtained by comparing the quality of fit for both the undistorted cubic model and the ferroelectric rhombohedral model over different length scales. Calculations of atomic PDFs for 20, 35, and 50 Å length scales (Figure 5.6) indicate the persistence of spatial

correlation among these local dipoles to distance scales of ~5 nm, close to the average particle diameter. Although spatial correlations are weakened in the nanocrystalline samples, some degree of linear coherence is maintained. These results are in agreement with the TEM measurements indicating a coherent, monodomain polarization state in most GeTe particles that is accompanied by local distortions and polarization rotation.

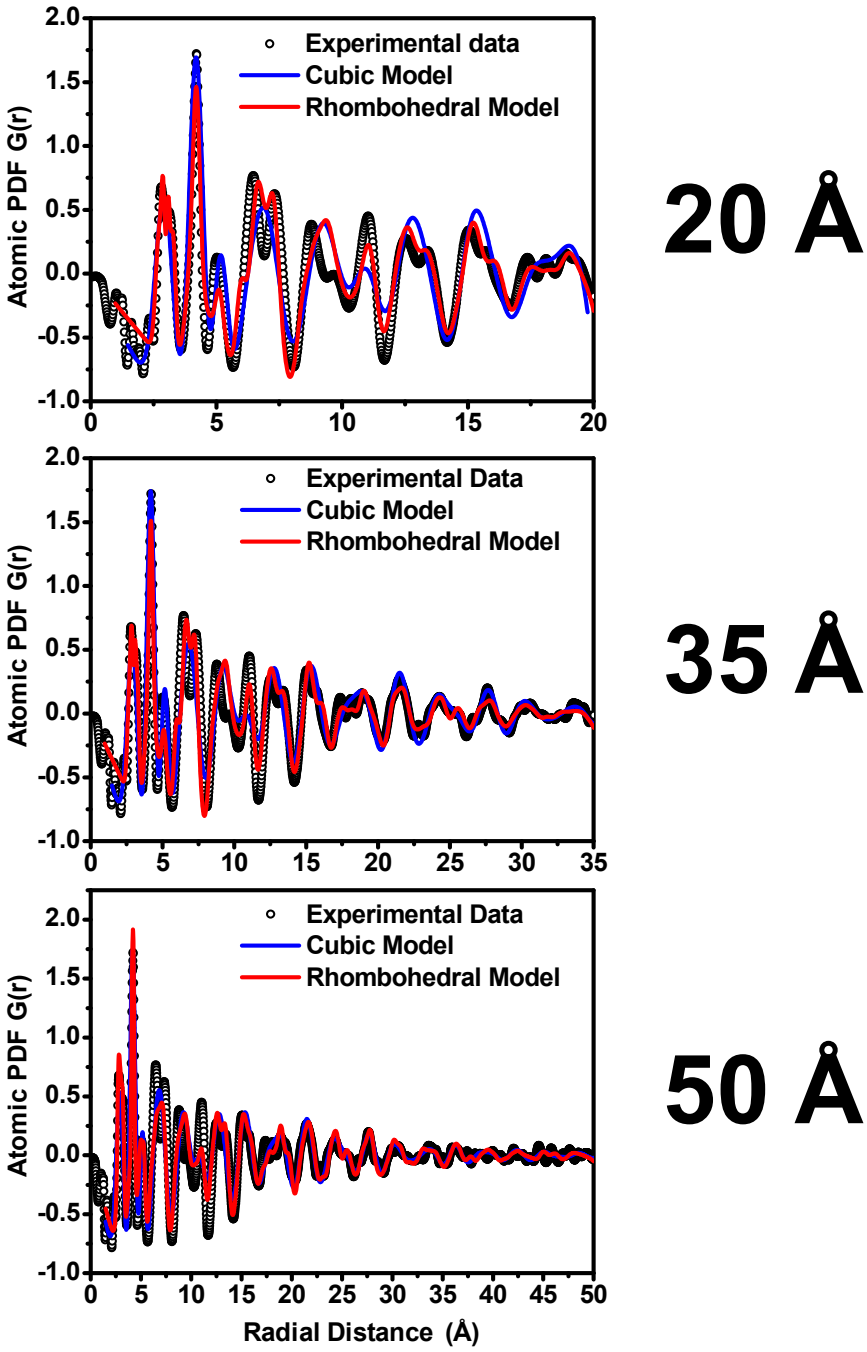

Figure 5.6. Comparison of atomic pair distribution functions for 8 nm GeTe nanocrystals at different length scales. Atomic PDFs for GeTe are compared with both cubic and rhombohedral models for length scales of 20, 35, and 50 Å. The rhombohedral model yields a superior fit at the shorter length scales, but the quality of fit becomes comparable for both models at longer length scales.

5.3.4 Atomic Pair Distribution Function Measurements of $BaTiO_3$ Nanocrystals:

Atomic PDFs were calculated from synchrotron diffraction patterns for 8 nm and 15 nm $BaTiO_3$ nanocubes and 10 nm $BaTiO_3$ nanospheres. Comparison of $BaTiO_3$ particles with similar sizes and different shapes was conducted in order to elucidate the impact of particle surface structure on the nature of the polarization state. Comparisons of the atomic PDFs for $BaTiO_3$ nanocrystals of all types (Figure 5.7) with a tetragonal structural model confirm the presence of local tetragonal distortions at room temperature. The tetragonal distortions maintain local coherence over a length scale of approximately 10 Å for the $BaTiO_3$ nanospheres, with an irregular surface structure, but persist up to approximately 20 Å for the 8 nm nanocubes and beyond 40 Å for the 15 nm nanocubes.

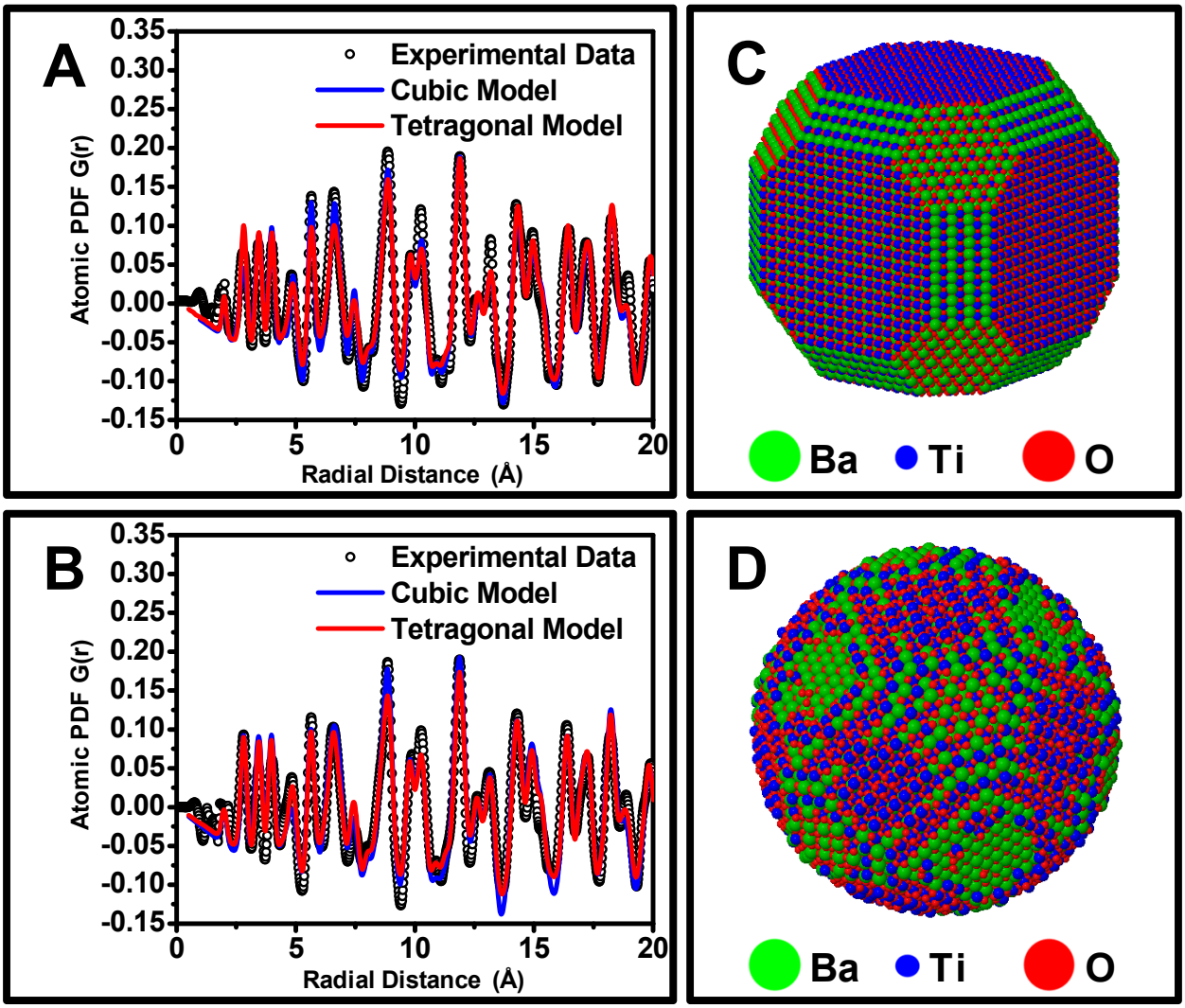

Figure 5.7. Atomic pair distribution function analysis of $BaTiO_3$ nanocubes and nanospheres. (A) Atomic pair distribution function (PDF) for 8 nm $BaTiO_3$ nanocubes compared with cubic and tetragonal structural models; (B) atomic PDF for 10 nm $BaTiO_3$ nanospheres compared with cubic and tetragonal structural models; (C, D) model structures for 8 nm $BaTiO_3$ nanocubes (C) and 10 nm $BaTiO_3$ nanospheres (D).

The atomic PDF measurements indicate correlation among local ferroelectric dipoles consistent with some degree of ferroelectric order, but indicate the presence of strong structural distortions, particularly for the spherical particles. This high degree of structural disorder is likely responsible for the observed reduction in piezoresponse for individual nanocubes

described in the previous chapter. Further comparison between $BaTiO_3$ nanocubes of two different sizes, 8 and 15 nm, indicates a marked enhancement in the spatial correlation among dipoles in the 15 nm sample, evidenced by a higher quality of fit to the tetragonal structural model. The PFM measurements presented in the previous chapter reveal a marked decline in piezoresponse from 10 nm to 5 nm cubes. It is clear that there exists a strong relationship between the structural disorder discerned from PDF analysis and the magnitude of the material piezoresponse determined from PFM, but the origins of this structural disorder require further elucidation.

5.3.5 Discussion of Results:

Experimental evidence on individual nanocrystals points to the preservation of a coherent, linear ferroelectric state at nanometer dimensions, albeit with significant local structural deviations and a decline in overall polarization. These trends can be attributed to a combination of surface-induced phenomena and depolarization effects. The role of the former is highlighted by the comparison of spherical and cubic $BaTiO_3$ nanocrystals of similar size. A marked decline in the spatial coherence of ferroelectric dipoles can be observed for the spherical sample in the atomic PDF studies, even when compared with cubic particles smaller in size. The cubic particles exhibit nearly atomically flat low-index surfaces, while the spherical particles possess an irregular surface structure with many high-index segments. As discussed in Chapter 3, internal stresses imposed by free surfaces proportional to $2\gamma/r$—in which γ is the surface energy and r is the particle radius—may approach values of several GPa in sub-10 nm particles[16] and have been found to reduce the magnitude of the polar distortion in nanosized perovskites[61,62]. The preponderance of high-energy surface facets and the irregular surface structure of the spherical particles likely enhance both the overall internal stresses and the inhomogeneity of the strain field, resulting in a reduction of the overall polar distortion and an enhancement of structural disorder, leading to the observed reduction in spatial coherence. It is notable that cubic particles smaller in size (but with greater surface area) retain stronger spatial dipole correlations. The influence of the surface here is thus not simply dependent on surface area or strictly a consequence of the well-known reduction in polarization near a ferroelectric surface described by Kretschmer and Binder[15]. The comparisons between cubes of different sizes and particles with different surface structures thus points to a more complex, specific surface effect governed not only by the surface area, consistent with the classical picture of Kretschmer and Binder, but also by the specific energies and arrangements of surface facets. These results suggest that careful control over surface terminations and particle shape control, a key advantage of colloidal synthetic procedures, may provide a pathway to the stabilization of ferroelectric ordering in nanoscale crystals.

Insight into the influence of depolarization effects may be obtained from the comparison of highly conducting GeTe with strongly insulating $BaTiO_3$ nanocrystals of comparable size. The large intrinsic free carrier density ($>10^{20}$ cm^{-3}) of GeTe is expected to provide metallic

conduction and strong internal screening of the polarization, minimizing depolarization effects, and sidesteps the notoriously difficult problem of electrical doping of colloidal nanomaterials. PDF analysis indicates markedly enhanced spatial correlations in GeTe (correlation length of 5 nm for 8 nm particles) relative to $BaTiO_3$ (correlation length of 2 nm for 8 nm nanocubes), although the correlation range does not span the entire diameter of the particles. These observations suggest a strong stabilization of the coherent polar state in GeTe by internal carriers. Both the PDF analysis and TEM studies, however, indicate considerable structural disorder and inhomogeneity in the polarization patterns of GeTe nanomaterials, suggesting a strong surface contribution. The results of Chapter 3 indicate a decline in the overall distortion magnitude with decreasing particle size, further supporting this interpretation. It is clear from these experiments that both surface structure and depolarization effects exercise a profound influence on the stability and nature of the polar state in low-dimensional nanosystems.

The marked decline in dipole correlations in $BaTiO_3$ nanocrystals of all types relative to GeTe suggests incomplete screening of polarization-induced surface charges, further confirmed by the observation of electrostatic fringing fields in the holograms arising from polarization-induced surface charges presented in the previous chapter. The stability of a linear polarization state under incomplete screening conditions contrasts with theoretical reports predicting a toroidal state for all screening conditions with the exception of nearly perfect short-circuit boundary conditions[96]. Despite imperfect screening conditions, the classical linear polarization state remains surprisingly stable, persisting at room temperature down to particle sizes of less than 10 nm. It is also notable that the polarization generally exists in a monodomain state. Several recent works on ion-milled single crystals of $BaTiO_3$ have revealed scaling laws describing the decrease in domain periodicity with decreasing side length down to dimensions of around 100 nm[45-47]. These scaling laws thus break down at the length scales observed in our experiments.

Given that neither perfect charge screening nor polarization domain formation occur to compensate the polarization, the persistence of the linear, monodomain state at nanometer dimensions lends itself to two rationalizations. The first arises from incoherent structural disorder leading to the frustration of local ferroelectric dipoles and a reduction of the overall polarization, as suggested in previous work[6,8]. The second involves local coherent polarization rotations that similarly weaken the overall linear polarization. Our polarization maps suggest polarization rotation, and in some cases flux closure, in some fraction of the observed particles. Such rotational tendencies further reduce the apparent spatial correlations of local dipoles and overall polarization. Both mechanisms likely contribute to the decline of ferroelectric order at finite dimensions, although the factors governing the dominant mechanism remain unclear and are the subject of ongoing investigation.

The work described in this chapter provides atomic-scale insight into the fundamental nature and stability of ferroelectric ordering down to its ultimate size limit. Careful atomic PDF studies point to the parallel roles played by surface-induced relaxation and depolarization effects in the dissolution of ferroelectric ordering at finite dimensions and indicate considerable structural disorder and dipole decoherence, even in conductive GeTe with strong polarization

screening. Strong polarization screening is provided by the high density of free carriers in GeTe, as evidenced by the observation of a well-defined localized surface plasmon resonance mode. These studies additionally demonstrate the utility of colloidal morphology control as a means of stabilizing the polar state at nanoscale dimensions. The experiments described in this chapter indicate a complex driving force for ferroelectric size effects involving significant contributions from both free surfaces and depolarization fields and provide a pathway to unraveling the fundamental physics of nanoscale ferroelectricity at the smallest possible size scales.

References

1. Lines, M. E.; Glass, A. M. *Principles and Applications of Ferroelectrics and Related Materials*; Clarendon Press: Oxford, 1977.

2. Scott, J. F.; Paz de Araujo, C. A. *Science* **1989**, *246*, 1400.

3. Scott, J. F. *Science* **2007**, *315*, 954.

4. Zhong, W. L.; Wang, Y. G.; Zhang, P. L.; Qu, B. D. *Phys. Rev. B* **1994**, *50*, 698.

5. Chattopadhyay, S.; Ayyub, P.; Palkar, V. R.; Multani, M. *Phys. Rev. B* **1995**, *52*, 13177.

6. Page, K.; Proffen, T.; Niederberger, M.; Seshadri, R. *Chem. Mater.* **2010**, *22*, 4386.

7. Smith, M. B.; Page, K.; Siegrist, T.; Redmond, P. L.; Walter, E. C.; Seshadri, R.; Brus, L. E.; Steigerwald, M. L. *J. Am. Chem. Soc.* **2008**, *130*, 6955.

8. Petkov, V.; Gateshki, M.; Niederberger, M.; Ren, Y. *Chem. Mater.* **2006**, *18*, 814.

9. Naumov, I. I.; Bellaiche, L.; Fu, H. *Nature* **2004**, *432*, 737.

10. Durgun, E.; Ghosez, P.; Shaltaf, R.; Gonze, X.; Raty, J.-Y. *Phys. Rev. Lett.* **2009**, *103*, 247601.

11. Polking, M. J.; Zheng, H.; Ramesh, R.; Alivisatos, A. P. *J. Am. Chem. Soc.* **2011**, *133*, 2044.

12. Adireddy, S.; Lin, C.; Cao, B.; Zhou, W.; Caruntu, G. *Chem. Mater.* **2010**, *22*, 1946.

13. Urban, J. J.; Yun, W. S.; Gu, Q.; Park, H. *J. Am. Chem. Soc.* **2002**, *124*, 1186.

14. O'Brien, S.; Brus, L.; Murray, C. B. *J. Am. Chem. Soc.* **2001**, *123*, 12085.

15. Kretschmer, R.; Binder, K. *Phys. Rev. B* **1979**, *20*, 1065.

16. Morozovska, A. N.; Glinchuk, M. D.; Eliseev, E. A. *Phys. Rev. B* **2007**, *76*, 014102.

17. Batra, I. P.; Wurfel, P.; Silverman, B. D. *Phys. Rev. Lett.* **1973**, *30*, 384.

18. Murray, C. B.; Kagan, C. R.; Bawendi, M. G. *Annu. Rev. Mater. Sci.* **2000**, *30*, 545.

19. Park, J.; Joo, J.; Kwon, S. G.; Jang, Y.; Hyeon, T. *Angew. Chem. Int. Ed.* **2007**, *46*, 4630.

20. Murray, C. B.; Sun, S.; Gaschler, W.; Doyle, H.; Betley, T. A.; Kagan, C. R. *IBM J. Res. Dev.* **2001**, *45*, 47.

21. Kovalenko, M. V.; Heiss, W.; Shevchenko, E. V.; Lee, J.-S.; Schwinghammer, H.; Alivisatos, A. P.; Talapin, D. V. *J. Am. Chem. Soc.* **2007**, *129*, 11354.

22. Murphy, J. E.; Beard, M. C.; Norman, A. G.; Ahrenkiel, S. P.; Johnson, J. C.; Yu, P.; Micic, O. I.; Ellingson, R. J.; Nozik, A. J. *J. Am. Chem. Soc.* **2006**, *128*, 3241.

23. Bahl, S. K.; Chopra, K. L. *J. Appl. Phys.* **1970**, *41*, 2196.

24. Fu, H.; Bellaiche, L. *Phys. Rev. Lett.* **2003**, *91*, 257601.

25. Baumgardner, W. J.; Choi, J. J.; Lim, Y.-F.; Hanrath, T. *J. Am. Chem. Soc.* **2010**, *132*, 9519.

26. Hickey, S. G.; Waurisch, C.; Rellinghaus, B.; Eychmueller, A. *J. Am. Chem. Soc.* **2008**, *130*, 14978.

27. Littlewood, P. B. *J. Phys. C: Solid State Phys.* **1980**, *13*, 4855.

28. Waghmare, U. V.; Spaldin, N. A.; Kandpal, H. C.; Seshadri, R. *Phys. Rev. B* **2003**, *67*, 125111.

29. Andrikopoulos, K. S.; Yannopoulos, S. N.; Voyiatzis, G. A.; Kolobov, A. V.; Ribes, M.; Tominaga, J. *J. Phys. Condens. Matter* **2006**, *18*, 965.

30. Lencer, D.; Salinga, M.; Grabowski, B.; Hickel, T.; Neugebauer, J.; Wuttig, M. *Nature Mater.* **2008**, *7*, 972.

31. Steigmeier, E. F.; Harbeke, G. *Solid State Commun.* **1970**, *8*, 1275.

32. Goldak, J.; Barrett, C. S.; Innes, D.; Youdelis, W. *J. Chem. Phys.* **1966**, *44*, 3323.

33. Chattopadhyay, T.; Boucherle, J. X.; Von Schnering, H. G. *J. Phys. C: Solid State Phys.* **1987**, *20*, 1431.

34. Snykers, M.; Delavignette, P.; Amelinckx, S. *Mater. Res. Bull.* **1972**, *7*, 831.

35. Tuan, H.-Y.; Korgel, B. A. *Cryst. Growth Des.* **2008**, *8*, 2555.

36. Meister, S.; Peng, H.; Mcllwrath, K.; Jarausch, K.; Zhang, X. F.; Cui, Y. *Nano Lett.* **2006**, *6*, 1514.

37. Yu, D.; Wu, J.; Gu, Q.; Park, H. *J. Am. Chem. Soc.* **2006**, *128*, 8148.

38. Buck, M. R.; Sines, I. T.; Schaak, R. E. *Chem. Mater.* **2010**, *22*, 3236.

39. Caldwell, M. A.; Raoux, S.; Wang, R. Y.; Philip Wong, H.-S.; Milliron, D. J. *J. Mater. Chem.* **2010**, *20*, 1285.

40. Rabe, K. M.; Ahn, C. H.; Triscone, J.-M. *Physics of Ferroelectrics: A Modern Perspective*; Springer Verlag: Berlin, 2007.

41. Seidel, J., et al. *Nature Mater.* **2009**, *8*, 229.

42. Chu, Y.-H.; He, Q.; Yang, C.-H.; Yu, P.; Martin, L. W.; Shafer, P.; Ramesh, R. *Nano Lett.* **2009**, *9*, 1726.

43. Kittel, C. *Introduction to Solid State Physics*; John Wiley and Sons: Hoboken, NJ, 2005.

44. O'Handley, R. C. *Modern Magnetic Materials: Principles and Applications*; John Wiley and Sons: New York, 2000.

45. Schilling, A.; Byrne, D.; Catalan, G.; Webber, K. G.; Genenko, Y. A.; Wu, G. S.; Scott, J. F.; Gregg, J. M. *Nano Lett.* **2009**, *9*, 3359.

46. Schilling, A.; Adams, T. B.; Bowman, R. M.; Gregg, J. M.; Catalan, G.; Scott, J. F. *Phys. Rev. B* **2006**, *74*, 024115.

47. Catalan, G.; Schilling, A.; Scott, J. F.; Gregg, J. M. *J. Phys. Condens. Matter* **2007**, *19*, 132201.

48. Enders, P. *Phys. Stat. Sol. B* **1983**, *120*, 735.

49. Snykers, M.; Serneels, R.; Delavignette, P.; Gevers, R.; Van Landuyt, J.; Amelinckx, S. *Phys. Stat. Sol. A* **1977**, *41*, 51.

50. Yashina, L. V.; Puettner, R.; Neudachina, V. S.; Zyubina, T. S.; Shtanov, V. I.; Poygin, M. V. *J. Appl. Phys.* **2008**, *103*, 094909.

51. Roitburd, A. L. *Phys. Stat. Sol. A* **1976**, *37*, 329.

52. Arlt, G. *J. Mater. Sci.* **1990**, *25*, 2655.

53. Luk'yanchuk, I. A.; Schilling, A.; Gregg, J. M.; Catalan, G.; Scott, J. F. *Phys. Rev. B* **2009**, *79*, 144111.

54. Uchino, K.; Sadanaga, E.; Hirose, T. *J. Am. Ceram. Soc.* **1989**, *72*, 1555.

55. Wuttig, M.; Yamada, N. *Nature Mater.* **2007**, *6*, 824.

56. Snyder, J.; Toberer, E. S. *Nature Mater.* **2008**, *7*, 105.

57. Bahl, S. K.; Chopra, K. L. *J. Appl. Phys.* **1969**, *40*, 4940.

58. Rabe, K. M.; Joannopoulos, J. D. *Phys. Rev. B* **1987**, *36*, 6631.

59. Onodera, A.; Sakamoto, I.; Fujii, Y.; Mori, N.; Sugai, S. *Phys. Rev. B* **1997**, *56*, 7935.

60. Scott, J. F. *Rev. Mod. Phys.* **1974**, *46*, 83.

61. Shiratori, Y.; Pithan, C.; Dornseiffer, J.; Waser, R. *J. Raman Spectrosc.* **2007**, *38*, 1288.

62. Geneste, G.; Bousquet, E.; Junquera, J.; Ghosez, P. *Appl. Phys. Lett.* **2006**, *88*, 112906.

63. Kabalkina, S. S.; Vereshchagin, L. F.; Serebryanaya, N. R. *Sov. Phys. JETP* **1967**, *24*, 917.

64. Ciucivara, A.; Sahu, B. R.; Kleinman, L. *Phys. Rev. B* **2006**, *73*, 214105.

65. Spanier, J. E.; Kolpak, A. M.; Urban, J. J.; Grinberg, I.; Ouyang, L.; Yun, W. S.; Rappe, A. M.; Park, H. *Nano Lett.* **2006**, *6*, 735.

66. Bawendi, M. G.; Steigerwald, M. L.; Brus, L. E. *Annu. Rev. Phys. Chem.* **1990**, *41*, 477.

67. Law, M.; Goldberger, J.; Yang, P. *Annu. Rev. Mater. Sci.* **2004**, *34*, 83.

68. Sun, S.; Murray, C. B. *J. Appl. Phys.* **1999**, *85*, 4325.

69. Jia, C.-L.; Nagarajan, V.; He, J.-Q.; Houben, L.; Zhao, T.; Ramesh, R.; Urban, K.; Waser, R. *Nature Mater.* **2007**, *6*, 64.

70. Jia, C.-L.; Urban, K. W.; Alexe, M.; Hesse, D.; Vrejoiu, I. *Science* **2011**, *331*, 1420.

71. Lichte, H.; Reibold, M.; Brand, K.; Lehmann, M. *Ultramicroscopy* **2002**, *93*, 199.

72. Chopra, K. L.; Bahl, S. K. *J. Appl. Phys.* **1969**, *40*, 4171.

73. Edwards, A. H.; Pineda, A. C.; Schultz, P. A.; Martin, M. G.; Thompson, A. P.; Hjalmarson, H. P.; Umrigar, C. J. *Phys. Rev. B* **2006**, *73*, 045210.

74. Kwei, G. H.; Lawson, A. C.; Billinge, S. J. L.; Cheong, S.-W. *J. Phys. Chem.* **1993**, *97*, 2368.

75. Adireddy, S. A.; Yourdkhani, A.; Caruntu, G. [in preparation] **2011**.

76. Gerchberg, R. W.; Saxton, W. O. *Optik* **1972**, *35*, 237.

77. Coene, W.; Janssen, G.; Op de Beeck, M.; Van Dyck, D. *Phys. Rev. Lett.* **1992**, *69*, 3743.

78. Rodriguez, B. J.; Callahan, C.; Kalinin, S. V.; Proksch, R. *Nanotechnology* **2007**, *18*, 475504.

79. McCartney, M. R.; Smith, D. J. *Annu. Rev. Mater. Sci.* **2007**, *37*, 729.

80. Kalinin, S. V.; Bonnell, D. A. *Phys. Rev. B* **2002**, *65*, 125408.

81. Nagarajan, V.; Roytburd, A.; Stanishevsky, A.; Prasertchoung, S.; Zhao, T.; Chen, L.; Melngailis, J.; Auciello, O.; Ramesh, R. *Nature Mater.* **2003**, *2*, 43.

82. Maksymovych, P.; Jesse, S.; Yu, P.; Ramesh, R.; Baddorf, A. P.; Kalinin, S. V. *Science* **2009**, *324*, 1421.

83. Jona, F.; Shirane, G. *Ferroelectric Crystals*; Dover Publications: New York, 1993.

84. Ma, W.; Hesse, D. *Appl. Phys. Lett.* **2004**, *85*, 3214.

85. Sun, S.; Zeng, H.; Robinson, D. B.; Raoux, S.; Rice, P. M.; Wang, S. X.; Li, G. *J. Am. Chem. Soc.* **2004**, *126*, 273.

86. Merz, W. J. *Phys. Rev.* **1953**, *91*, 513.

87. Streiffer, S. K.; Eastman, J. A.; Fong, D. D.; Thompson, C.; Munkholm, A.; Ramana Murty, M. V.; Auciello, O.; Bai, G. R.; Stephenson, G. B. *Phys. Rev. Lett.* **2002**, *89*, 067601.

88. Junquera, J.; Ghosez, P. *Nature* **2003**, *422*, 506.

89. Luther, J. M.; Jain, P. K.; Ewers, T.; Alivisatos, A. P. *Nature Mater.* **2011**, *10*, 361.

90. Huang, B.; Robertson, J. *Phys. Rev. B* **2010**, *81*, 081204.

91. Petkov, V. *J. Appl. Cryst.* **1989**, *22*, 387.

92. Farrow, C. L.; Juhas, P.; Liu, J. W.; Bryndin, D.; Bozin, E. S.; Bloch, J.; Proffen, T.; Billinge, S. J. L. *J. Phys. Condens. Matter* **2007**, *19*, 335219.

93. Raoux, S.; Cheng, H. Y.; Caldwell, M. A.; Philip Wong, H.-S. *Appl. Phys. Lett.* **2009**, *95*, 071910.

94. Spectral Database for Organic Compounds SDBS No. 10643. http://riodb01.ibase.aist.go.jp/sdbs/cgi-bin/direct_frame_top.cgi (accessed Aug 17, 2011).

95. Lewis, J. E. *Phys. Stat. Sol. B* **2006**, *59*, 367.

96. Ponomareva, I.; Naumov, I. I.; Bellaiche, L. *Phys. Rev. B* **2005**, *72*, 214118.